Mean and Eddy Induced Transport in the Ocean Region Adjacent to the Greenland-Scotland Ridge

by

© *Sarah Lundrigan*

A thesis submitted to the

School of Graduate Studies

in partial fulfilment of the

requirements for the degree of

Doctor of Philosophy

Department of *Physics and Physical Oceanography*

Memorial University of Newfoundland

October 2019

St. John's Newfoundland

Abstract

The circulation and transport in the ocean region adjacent to the Greenland-Scotland Ridge (GSR) are crucial for maintaining heat, freshwater, and sea-ice exchange between the Nordic Seas and Subpolar North Atlantic Ocean. The Nordic Seas receive low-density Atlantic Water and transform it into dense water. The dense water overflow contributes to the North Atlantic Deep Water mass formation, which feeds the lower limb of the Atlantic Meridional Overturning Circulation. The thesis presents results from a study of the temperature and salinity transport in the ocean region adjacent to the GSR consisting of three sub-projects.

The first sub-project is focused on model simulations of interannual to decadal variability of the exchange through the GSR and its impact on the variability of the temperature and salinity in the Nordic Seas. The model results demonstrate that the increase in the transport of fresh and cold waters through Fram Strait in the 1960s was concurrent with a reduction in the exchange over the GSR. The resulting imbalance in salinity and heat fluxes through the strait and over the ridge contributed to the freshening of the water masses of the Nordic Seas and intensified the Great Salinity Anomaly in the 1960s. In the late 1980s the AW transport over the GSR was stronger than normal while the exchange through Fram Strait was close to normal. The related imbalance in the lateral heat fluxes through the strait and over the ridge warmed the Nordic Seas and caused an increase in the temperature of the AW inflow to the Arctic Ocean in the late 1980s (i.e., about a decade earlier than the warming of the subpolar North Atlantic Ocean in the mid-1990s).

The second sub-project is focused on observational estimates of the heat flux

convergence of the ocean region adjacent to the GSR. Along-track altimeter and sea surface temperature satellite observations and ARGO in-situ measurements of temperature and salinity are used to investigate the heat transport by mean currents and eddies in the ocean region adjacent to the GSR from 2003 to 2008. The results from the analysis show that the heat advection by the mean flow in the surface layer is zonally asymmetric with a higher magnitude in the western part of the region. This asymmetry is associated with an excessive mean heat advection in an area adjacent to the Denmark Strait. The advection of heat is high and positive south of the strait and low and negative north of it. We suggest that this heat advection impacts the local budgets of heat and potential energy of the mean flow in the surface layer.

The third sub-project studies the vertical structure of the convergence of advective fluxes of heat (HFC) and salt (SFC) in the ocean region adjacent to the GSR. The study is based on SODA (Simple Ocean Data Assimilation) ocean reanalysis for the period between 1965 and 2010. The SODA based estimates show that the high values found in satellite based estimates of HFC over the Denmark Strait are part of a pattern of high HFC and SFC in the whole water column. In this region, the HFC has a maximum at the surface. The highest values of SFC there are found in the subsurface layer at depths between 500 and 1500 m. A similar structure of high positive SFC and HFC are observed at intermediate depths over the Iceland-Faroe Ridge. The EOF analysis of the HFC and SFC shows that the variability of the HFC and SFC in these two regions are dominated by modes of coherent variations in the SFC and HFC. During warming period in the late 1980s these modes drove strong variations of the HFC and SFC over Denmark Strait and Iceland-Faroe Ridge which correlated well with the variations in the surface wind stress curl.

Acknowledgments

This research was supported by the National Sciences and Engineering Research Council of Canada (NSERC), the Ocean Frontier Institute (OFI) and by Canadian Foundation for Climate and Atmospheric Science through the GOAPP and GR-631.

The projects presented in this thesis were supported and tirelessly assisted by my supervisor Entcho Demirov. This thesis would not be possible without his support and guidance.

Contents

List of Tables

List of Figures

Chapter 1

Introduction

The subarctic ocean is a crucial element of the global climate system. It connects the cool, fresh Arctic and the warm, salty Atlantic Ocean. The ocean transport through the subarctic is essential for maintaining the present day exchange of heat and freshwater between the Arctic Mediterranean and the Atlantic Ocean.

The Arctic Mediterranean comprises the Arctic and Nordic Seas, see Figure 1.1. It receives warm and salty Atlantic waters and transforms them into cold dense intermediate and deep water masses (Meincke, Rudels & HJ Friedrich, 1997). The overflow of dense waters from the Arctic Mediterranean through the Greenland Scotland Ridge (GSR) contributes to the North Atlantic Deep Water which feeds the lower limb of the Atlantic Meridional Overturning Circulation -AMOC (R.R. Dickson & Brown, 1994).

The warm and salty Atlantic waters enter the ocean region adjacent to the GSR through multiple branches of the North Atlantic Current (Figure 1.2). The air-sea exchange and mixing in the subpolar gyre modify these waters. As they propagate in the subarctic they gradually become colder and denser and a part of them enters

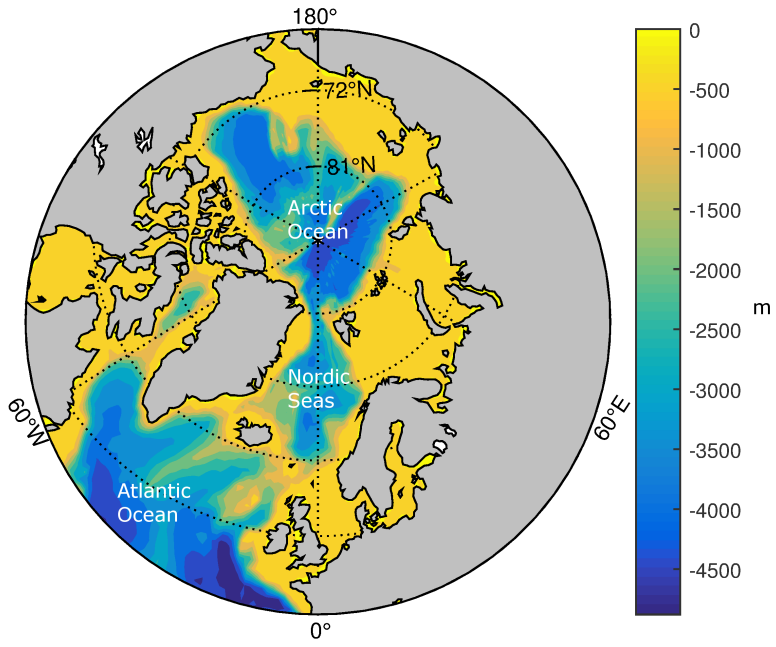

Figure 1.1: Bathymetry of the Arctic Ocean, Nordic Seas and Subpolar ocean.

the Arctic Mediterranean through the GSR. The rest of the modified Atlantic waters propagate in the Irminger and Labrador Seas.

The waters of the Arctic Ocean enter the subpolar North Atlantic through three main conduits: the Canadian Arctic Archipelago, Baffin Bay and Fram Strait. The latter is the deepest connection between Arctic and subarctic and is of key significance for heat, freshwater and sea-ice exchange between these two ocean regions. The inflow from the Fram Strait spreads in the Nordic Seas along the east coast of Greenland. It is gradually modified by the processes of air-sea exchange and mixing. Part of these waters enter the North Atlantic through the GSR. The rest of them propagates through the Nordic Seas.

Being relatively shallow the GSR, which separates the North Atlantic from the Arctic Mediterranean, restricts the exchange of deep and intermediate waters between these two basins. The transport through the GSR includes inflow of surface modified Atlantic water into the Nordic Seas over the Iceland-Faroe Ridge and through the Faroe-Shetland Channel, and a return flow of polar waters of Arctic origin and dense-water overflow into the Atlantic Ocean (Hansen & Østerhus, 2000). The difference in the characteristics of the inflow and outflow through the GSR implies a net heat and salt flux into the Arctic Mediterranean. The long-term variations in heat and salt transport through the GSR have significant implications for the variability of the Arctic Mediterranean (Yashayaev & Seidov, 2015).

The focus of this thesis is on the ocean dynamics in the region adjacent to the GSR and its impact on the transport of heat and freshwater. This chapter gives an overview of the region in the context of the study outlining the main oceanographic characteristics of the region, such as general topography, water masses and circulation

and the data and methods of the study.

1.1 The Ocean Region Adjacent to the Greenland Scotland Ridge

1.1.1 Bathymetry and Configuration

The ocean region of this study extends from 59^{o}N to 80$^o N$ in the meridional direction. Zonally, it is limited by the coasts of Norway and Greenland (Figure 1.2). The GSR which separates the North Atlantic from the Arctic Mediterranean spans a relatively shallow sub-area in this region. The maximum depth in the Iceland-Faroe Ridge is 450 m. The Faroe Bank Channel and the Denmark Strait provide a deeper connection with sill depths of 840 and 630 m respectively.

The part of the Eastern North Atlantic in the studied region south of the GSR is subdivided into two basins, the Irminger Sea and the Iceland Basin separated from each other by the Reykjanes Ridge. The maximum depth in these two ocean basins are about 3000 m. In the south-west the Irminger Sea is connected to the Labrador Sea.

To the north of the GSR is the Nordic Seas which refer collectively to the Norwegian, Greenland and Iceland Seas (Figure 1.2). The Norwegian Sea includes the Lofoten (maximum depth of 3200 m) and the Norwegian (maximum depth of 3600 m deep) basin. The Iceland Sea (maximum depth of 1800 m) is bounded by Greenland-Scotland Ridge to the south and the Jan Mayen Fracture zone to the north. The Greenland Sea is separated from Iceland Sea and the Norwegian Sea by the Jan

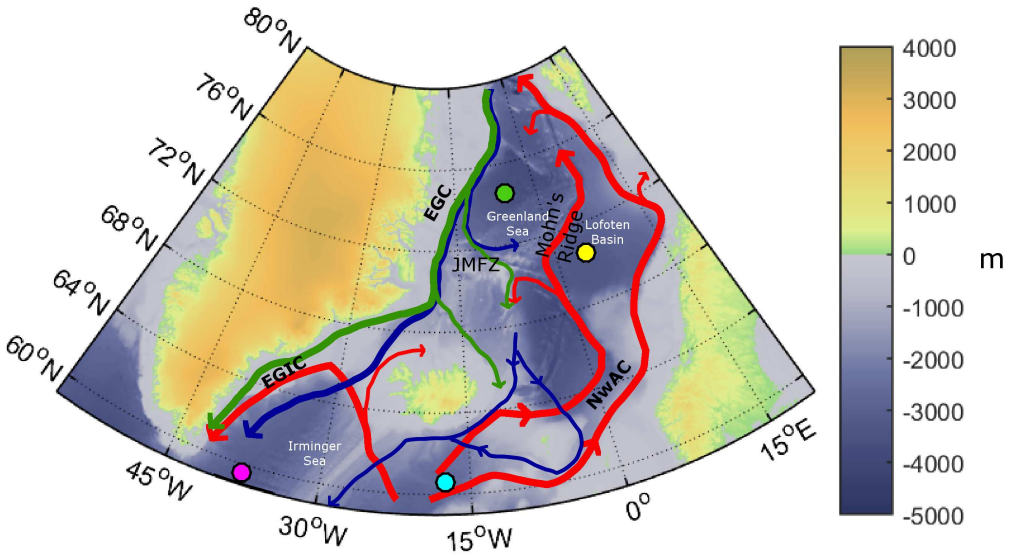

Figure 1.2: Bathymetry and main currents in the ocean region adjacent to the GSR. The red arrows show currents transporting the warm waters of the Atlantic Ocean. The green arrows show near surface currents and blue arrows show the currents at the intermediate and deep layers. The dots indicate the positions of the TS diagrams shown in Figure 1.3. The Mohn's Ridge and Jan Mayen Fracture Zone (JMFZ) are labeled.

Mayen Fracture zone and the Mohns Ridge. The northern border of the Nordic Seas is the Fram Strait. The Fram Strait, which is located between Greenland and Svalbard, provides the deepest connection (sill depth of 2600 m) between the Arctic Ocean and the Nordic Seas. The other connections between the global ocean and the Arctic have significantly smaller depth; about 250 m in the Barents Sea; about 200 m in the Canadian Arctic Archipelago and 50 m in the Bering Sea.

1.1.2 Water Masses

In the ocean region south of the GSR, the warm and salty Atlantic waters are cooled and modified as they spread through the subpolar gyre. These modified Atlantic Waters form the Subpolar Mode Water (SPMW) which is nearly uniform vertically in temperature, salinity and density. The SPMW extends over a large horizontal area in the subpolar gyre. In the Irminger Sea the SPMW (Figure 1.3) has a density of about 27.5 kg/m^3 and occupies the surface 700 m layer (Våge et al., 2011). A remnant of the SPMW, called the Irminger Water (IW) (see Myers, Kulan & Ribergaard (2007)), spreads at intermediate depths in the Irminger and Labrador seas. The IW has a density less than 27.70 kg/m^3. It is relatively warm and salty (see Figure 1.3) and plays an essential significant role in the heat budget of the Irminger and Labrador Seas (Straneo, 2006; Zhu & Demirov, 2011). In the Irminger Sea, there is a sharp horizontal frontal area separating the SPMW from the cold and fresh water of Arctic origin that is transported by East Greenland Current southward along the east coast of Greenland.

There are no major bathymetric restrictions for the propagation of deep and inter-

mediate water masses between the Irminger Sea and the Labrador Sea. The Labrador Sea Water (LSW) spreads easily in the Irminger Sea. The LSW is mostly formed by deep convection in the Labrador Sea and propagates at intermediate depths along the western boundary current, towards the Irminger Sea, and into the central Atlantic. The depth of the LSW is between 500 and 1500 m. During cold winter periods, the part of the LSW entering the Irminger Sea can be renewed by deep convection (Pickart, Torres & Fratantoni, 2005). The LSW is a weakly stratified water mass. It has density between 27.70 kg/m^3 and 27.80 kg/m^3 (Våge et al., 2011).

The North Atlantic Deep Water in the Irminger Sea is comprised of two water masses, the Denmark Strait Overflow water (DSOW) and the Iceland-Scotland Overflow (ISOW). Both of these water masses have a density greater than 27.80 kg/m^3. They originate in the Nordic Seas and are carried into the Irminger Sea by the near-bottom dense overflow through the Denmark Strait and over the Iceland-Faroe Ridge. The DSOW is the slightly denser of the two. The ISOW is relatively salty and warm and spreads above the DSOW in the North Atlantic. The greater salinity of the ISOW is a result of entrainment of the SPMW over the Iceland-Scotland Ridge.

There are four main water masses in the Nordic Seas, the Atlantic Water (AW), the Polar Water (PW), the intermediate Atlantic Water (IAW) and the deep water. The PW is located from the surface to 150 m mostly in the western half of the Nordic Seas. These are Arctic waters which enter through the Fram Strait. The temperature of the PW is below 0^oC near Greenland in both the summer and the winter (see Figure 1.3). The PW is separated vertically from the underlying IAW by a sharp halocline. The surface salinity of the PW is less than 30 PSU and increases with depth to about 34 PSU or higher near the halocline (Coachman & Aagaard, 1974).

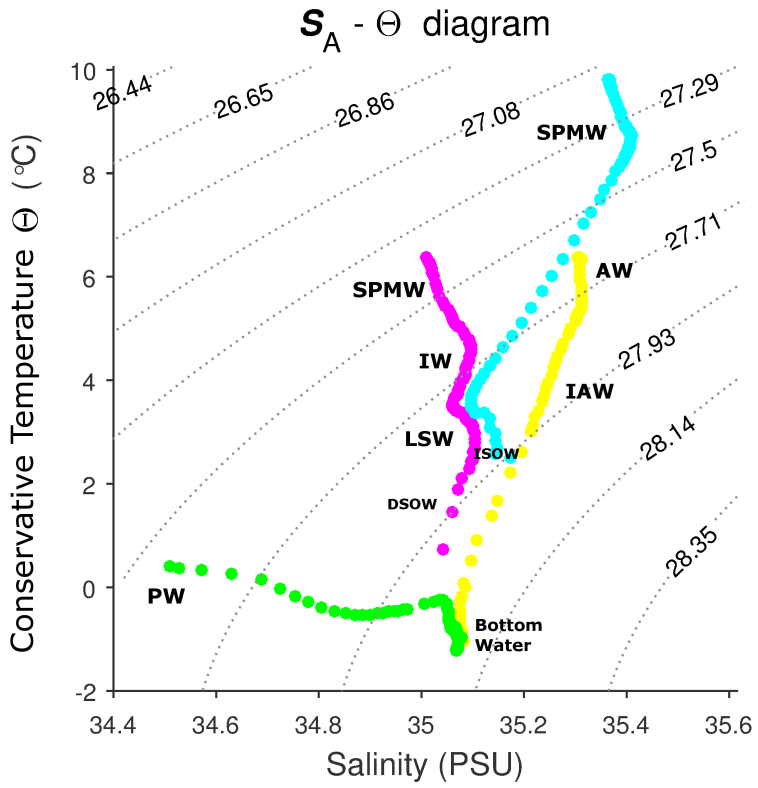

Figure 1.3: Temperature-Salinity diagram of water masses in the Nordic Seas. Location of the T-S curves are shown in Figure 1.2. Lines of constant σ_θ are shown with dotted lines.

The upper ocean layer in the eastern Nordic Seas is occupied by the warm and salty AW. As it travels northward the temperature of the AW decrease from 8^oC to 3^oC in the winter and from 10^oC to 6^oC in the summer. The salinity of the AW varies and increases from the polar water values downward until the salinity reaches 34.88 to 35.00 PSU. Below the AW is the IAW which forms from the vertical mixing between warm AW and colder waters at intermediate depths. The IAW extends between the bottom of the AW and down to depths of about 800 m. The temperature of the IAW is positive and has a maximum at between 200 and 400 m depth.

The layer under 800 m in the Nordic Seas is occupied by the deep water. It has quasi-uniform temperature and salinity in the vertical (Coachman & Aagaard, 1974). The temperatures of the deep water is below 0^oC and its salinity is between 34.87 and 34.95 PSU. The deep water forms, normally, from deep convection events in the winter and predominantly in the Greenland and Norwegian Seas (Coachman & Aagaard, 1974) (see Figure 1.3).

1.1.3 Ocean Currents

The main ocean currents of the region adjacent to the GSR are shown in Figure 1.2. The red arrows indicate warm currents and the blue/green arrows show ocean currents transporting relatively cold waters.

The North Atlantic Current (NAC) originates from the Gulf Stream. It transports warm and salty water northwards in the upper layers mostly in the eastern part of the region. In the subpolar North Atlantic the NAC splits in several branches. One of them passes over the GSR and becomes the Norwegian Atlantic Current (NwAC). A

second branch recirculates in the subpolar gyre and feeds the Irminger Current (IC). The IC transports warm salty water over the Reykjanes Ridge into the Irminger and Labrador Seas (Bersch, 1995). At the northernmost part of the IC, near Iceland, a small portion of the current branches off and continues northward and becomes the North Icelandic Irminger Current (NIIC) while the rest of the IC returns south. The NIIC continues northward and eastward along the coast of Iceland, which brings salty and warm surface SPMW along the Iceland coast.

The NwAC carries the AW northward over the GSR into the Nordic Seas. Then it propagates along the coast of Norway. The NwAC has two main branches which are relatively narrow and persistent currents. The inner branch follows closely the continental slope off the coast of Norway. The outer branch is a baroclinic, topographically steered jet. In the northern part the waters transported by NwAC exit the Nordic Seas into the Arctic Ocean through the Barents Sea and the Fram Strait. In this region, the NwAC partly recirculates in the Greenland Sea.

In the western part of the studied region, the East Greenland Current (EGC) transports cold and fresh waters (see Figure 1.2) and sea ice of Arctic origin along the east coast of Greenland (B. Rudels, H. Friedrich & Quadfasel, 1999; B. Rudels, Fahrbach, et al., 2002). The waters transported by the EGC includes PW, recirculated IAW and deep water.

At the Jan Mayen Fracture Zone, the part of the EGC that is deeper than 1800 m is diverted eastward. In the upper later, the EGC branches, with the main branch flowing along the coast of Greenland. The deflected part of the EGC flows eastward and becomes the Jan Mayen Current. This current extends along the southern part of the Greenland Sea gyre.

Further south, another branch separates from the EGC (see Figure 1.2) and forms the East Icelandic Current (EIC) (Blindheim & Osterhus, 2005). This current brings cold and fresh waters from the EGC along the northern and eastern coasts of Iceland. The main branch of the EGC extends southward and passes through the Denmark Strait.

South of the Denmark Strait, the EGC flows over the shelf along the coast of Greenland parallel to the IC. The IC and the EGC that flows southward in this region along the East Greenland/Irminger hydrographic front are collectively referred to as the East Greenland Irminger Current (EGIC) (Pickart, Torres & Fratantoni, 2005).

1.1.4 Mesoscale Dynamics

The warm salty Atlantic Water transported by the NwAC north of the GSR undergoes intense transformation in the Nordic Seas. The air-sea exchange through the ocean surface drives vertical mixing and deepening of the surface mixed layer. The Intermediate Atlantic Water (IAW) forms as a result of the vertical mixing of AW with the dense intermediate waters.

Deep convection in the Nordic Sea occurs mostly in the Greenland and Iceland Seas. The weak stratification (Johannessen, Lygre & Eldevik, 2005), doming of the isopyncals (Rhein, 1996), and winter sea ice formation (Pawlowicz et al., 1995) contribute to the intensification of winter convection in the central part of these two ocean basins. The deep convection in the centers of the Greenland and Iceland gyres reach depths of about 1000 m (B. Rudels, Quadfasel, et al., 1989). The relatively warm and saline AW and IAW and cold PW are entrained into the two gyres and

play an essential role in their overall heat budget. The heat gain due to the inflow of the AW and IAW is balanced by air-sea exchange and transport of cold waters and sea-ice by nearby PW. The eddy-induced transport plays a dominant role in the lateral exchange of heat and salt in the Greenland and Iceland Seas. (Latarius & Quadfasel, 2010; Mauritzen, 1996a; Mauritzen, 1996b; Eldevik et al., 2009).

The assessment of the heat and salt eddy-induced transport using high-latitude observations is difficult because of the small scale of the mesoscale eddies. The typical scale of mesoscale eddies can be determined by the first Rossby Baroclinic Radius of Deformation (Rd_1). This is the length scale at which the effects of rotation become as important as buoyancy effects in the geostrophic balance. The values of Rd_1 in the ocean depend on the buoyancy frequency N:

$$N^2 = -\frac{g}{\rho_o}\frac{\partial \rho(z)}{\partial z}$$

where g is gravity, $\rho(z)$ is the potential density, ρ_o is the averaged ocean density. For a constant N

$$Rd_1 = \frac{NH}{\pi f}$$

where H is the ocean depth and f is the Coriolis parameter (Gill, 1982). The first Rossby Baroclinic Radius of deformation is much smaller at higher latitudes, where the values of N are relatively small. In more realistic ocean applications where N is not a constant but depends on the depth, the exact value of Rd_1 can be obtained by solving the Sturm-Liouville eigenvalue problem for the vertical structure of vertical velocity.

$$N^{-2}(z)\frac{d^2\phi}{dx^2} + c^2\phi = 0$$

with boundary conditions:

$$\phi = 0; z = 0; z = -H$$

The solutions of the eigenvalue value problem

$$c_i = fRd_i$$

determine the phase speed for the i-th baroclinic Rossby mode. The average estimate of Rd_1 for the Norwegian Sea is about 7 km (Nurser & Bacon, 2014) and can be as low as 1.4 km in the Greenland Sea. For comparison the values of Rd_1 in the Subtropical North Atlantic vary between 20 and 60 km (Chelton, DeSzoeke, et al., 1998).

The small Rossby radius at high latitudes imposes restrictions on the quality and resolution of the observational data sets used in studies of mesoscale dynamics. The spatial resolution of gridded satellite and in-situ data is not sufficient for studies of mesoscale eddies and their impact on the transport of salt and heat. Karimova (2017) have shown that gridded altimeter products are suitable for studies of eddies with diameter is larger than 70 km. In this study, eddy-induced heat and salt transports are assessed with along-track satellite altimetry observations which resolve the mesoscale at high latitudes.

1.2 Ocean Observations

The subarctic has been studied since the late 19th century (Mohn, 1887). For a long time, however, observational data remained rather limited in terms of spatial

coverage and frequency. Severe weather and presence of sea-ice at the ocean surface made large scale observational surveys rather difficult. The following developments over the past two-three decades made such studies possible. In the late 19th century and through most of the 20th century the observations were largely ship based. These observational studies were the first to identify the Arctic and Atlantic water masses and the characteristics of their variability, the major bathymetric features and they main currents. At the same time these observations were shipped based and therefore limited in their spatial and temporal coverage and due to their equipment at the time limited in their accuracy.

Over the past few decades there was a dramatic development in the technology for ocean observations in the subarctic. A major development in the observing system was the addition of regular mooring station observations which started in the Norwegian Sea in the late 1990s and early 2000s. Some of these stations were positioned at key points along the GSR to study the inflow of AW into the Norwegian Sea. These mooring observations include ADCP and standard CTD sections (B. Dickson, J. Meincke & P. Rhines, 2008). Repeated hydrographic sections were conducted along the coast of Norway to monitor the flow of the AW in the Norwegian Sea, the Barents Sea Opening, Svinoy and the Sorkapp sections. In the Barents Sea Opening there are repeated hydrographic (CTD) sampling since the 1960s and current measurements since 1997. The Svinoy section has been studied since the mid 1950s and the Sorkapp section since the late 1970s. These moorings give detailed information about the variations of the water mass characteristics at these sections. However, some moorings only existed for a short period of time and, due to the fact that moorings are stationary, they only take measurements at specific locations and usually only for certain

periods of time. Over the last two to three decades, the technology of ocean observation dramatically improved. The new methods of ocean observations implemented over the past two decades include new sensors, mobile autonomous platforms, and fast communication tools.

The development in the satellite altimetry technology was a major breakthrough in ocean observing methods which started in the 1980s and 1990s. The first satellite mission of GEOSAT in 1978 demonstrated the strong potential of the sea-surface height observations in ocean studies. Many different satellite missions (for example Geosat, ERS-1, Topex/Poseidon, GFO, ERS-2, Envisat, Jason-1) were launched over the past couple of decades. Presently, several satellites (Jason-2, Cryosat-2, HY-2A, SARAL, Sentinel-3, Jason-3) are operational and they produce high quality near-real time sea-surface height data. The high-accuracy observations of sea-level from the space were a basis for essential advancement of the understanding of ocean dynamics over the past two decades.

Satellite altimetry measures the time taken by a radar pulse to travel from the satellite antenna to the surface and back to the satellite receiver. Using this precise time measurement combined with exact location of the satellite, the sea-surface height (SSH) can be calculated. The SSH is a sum of three components – the geiod, the absolute dynamic dynamic topography, and the sea-level anomaly. The geoid is the equipotential surface of the Earth, which is everywhere perpendicular to the local direction of gravity plus centrifugal force due to the planetary rotation. It would be the equilibrium surface for the motionless ocean, i.e. where no waves and currents exist. The absolute dynamic topography is the best fit, in a least-squares sense, of global mean sea level above the geoid. It depends on the ocean temperature,

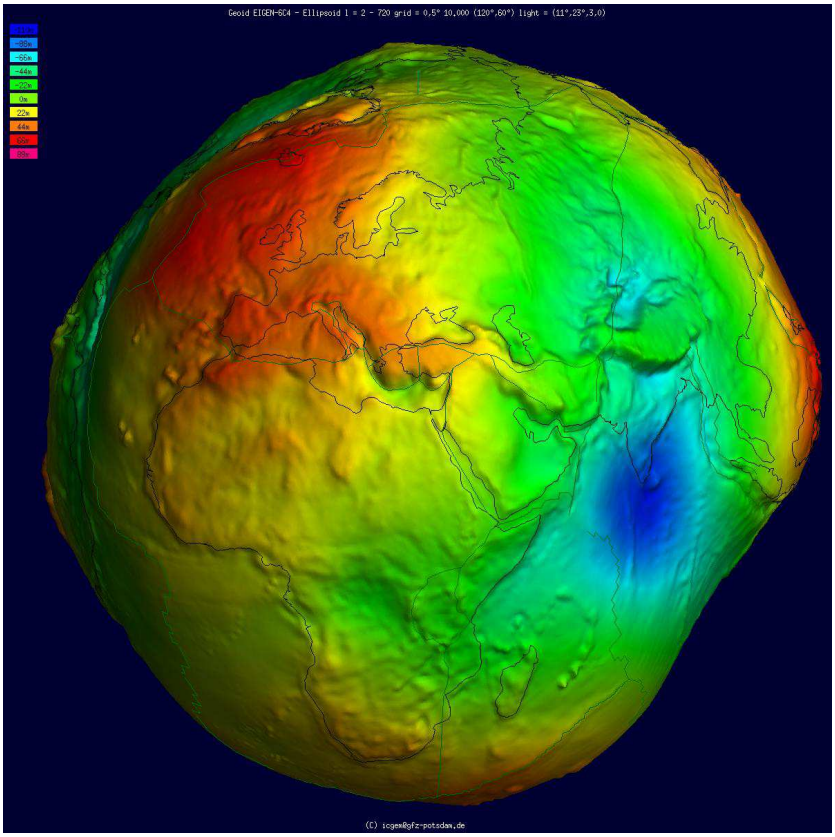

Figure 1.4: The surface of Earth Geoid. (reproduced from Ince et al. (2019) with permission.

salinity and mean circulation and is usually assumed to be constant in time. The absolute dynamic topography, however, can vary due to climate change and long term interdecadal and centennial changes in the bottom topography, temperature, salinity, and ocean currents.

The reference ellipsoid is much smoother than the real Earth surface. The GOCE satellite mission determined the exact height of the earth's surface based on precise gravity observations (see Figure 1.4). The spatial irregularities of the geoid height are produced by the distribution of the Earth's density.

As a satellite passes over the surface of the oceans it measures the instantaneous sea surface height. The along-track sea level is then calculated as the difference between the height measured by the satellite SSH and the mean sea surface height. It is also corrected for any atmospheric interference, such as cloud cover.

Satellite observations of the global ocean are available operationally in near-real time beginning in the early 1990s. However, not all ocean observing satellites follow tracks that allow for high latitude observations. For example Jason-3 only observes up to 60^oN. For our study, Geodetic and Oceanographic SATellite Follow-On (GFO) and Envisat (EN) were chosen because they had good coverage of our study area. The data from the satellite sea level observations is available both as gridded products and as along track data which determine the sea surface height at points along the path of the satellite's orbit. The gridded products are averaged over space and time to create evenly gridded sea level data, from which other physical characteristics, such as velocity, can be calculated. This gridding often leads to smoothing of data and loss of spatial and temporal resolution. This issue is significant in the areas of small Rossby radius of deformation. A major part of the mesoscale processes in the subarctic are unresolved by gridded altimeter data. In this study we use the along-track data for analysis of eddy-induced fluxes determined by Equations 1.6 and 1.7.

Another important component of the global ocean observing system in the subarctic is the Global Drifter Program (GDP), which also known as the Surface Velocity Program (SVP). Together with the satellite observations, these programs provide a comprehensive data set for the study of surface ocean dynamics. This includes surface characteristics such as current velocities, sea surface temperature, sea surface salinity and atmospheric characteristics at sea level. The project started in 1979 but a sig-

nificant amount of drifters were deployed only since 1992. However, the observations from ocean drifters as repeat measurements at the same location and time of year are not likely. Another limitation of drifter observations in the ocean region adjacent the GSR is that the drifter deployments are still sparse.

1.3 Ocean Heat and Salt Transport

Mean currents and turbulence in the ocean region adjacent to the GSR play an essential role in the meridional heat and freshwater transports. The waters in the ocean region adjacent to the GSR, are intensively transformed through surface air-sea exchange, advection, and mixing. This transformation modifies the seawater characteristics like the heat and salt content.

The main boundary currents in the studied region like the Irminger Current, East Greenland Currents and Norwegian Atlantic Current are persistent flows with quasi-permanent paths. They are baroclincally unstable and generate mesoscale eddies which have an impact on the horizontal heat and the freshwater transport across the ocean region adjacent to the GSR. When the eddies move (Dong et al., 2014) towards the central part of the region they bring waters with characteristics typical of the area of their formation in the boundary currents. Some eddies have a lifetime of up to several months. During this time they cover distances of hundreds of kilometres (Isachsen, Koszalka & JH LaCasce, 2012).

Variability in ocean temperature (T) and salinity (S) is determined by the advection-diffusion equations:

$$\frac{\partial T}{\partial t} + \mathbf{u} \cdot \nabla T + w\frac{\partial T}{\partial z} = \nabla \cdot \nu \nabla T + \frac{\partial}{\partial z}\nu\frac{\partial T}{\partial z} \tag{1.1}$$

$$\frac{\partial S}{\partial t} + \mathbf{u} \cdot \nabla S + w\frac{\partial S}{\partial z} = \nabla \cdot \nu \nabla S + \frac{\partial}{\partial z}\nu\frac{\partial S}{\partial z} \tag{1.2}$$

where $\mathbf{u} = (u, v)$ is the horizontal current velocity, w is the vertical component, ν is the molecular diffusivity and ∇ is the horizontal gradient operator. Equations 1.1 and 1.2 determine the change in T and S due to dynamical processes in the ocean which span motions and scales from small and fast to large and slow.

Present day models and observations in general agree about the mean large-scale circulation of the global ocean. Mesoscale and sub-mesoscale processes are less understood. These processes have relatively small scales and are not entirely resolved by ocean models and observations. Understanding of their dynamics is important for understanding meridional heat and freshwater exchange since they can influence ocean transport due to nonlinear dynamics.

Model data and observations are used in this study to assess the horizontal transport heat and salt. This transport is separated into mean and eddy components. The mean advection due the large-scale ocean general circulation assumes quasi-steady characteristics ($(\overline{u})$, $(\overline{v})$, $(\overline{w})$, $(\overline{T})$, $(\overline{S})$) which in this study are estimated as the mean over a specific time period. The latter is normally determined based on the time scale of the studied processes and the length of the data.

Following the definition of Wunsch (1999), the eddy components of velocity, temperature and salinity here are defined as the variability with respect to the record mean, regardless of its dynamical cause. Therefore, the "eddy" components

(u', v', w', T', S') of u, v, w, T, and S involve physical processes in a rather broad temporal interval including intraseasonal, seasonal, interannual and decadal time scales.

There are also limitations in resolving the fine-scale components of the "eddy"-induced flow and transport. It is considered later in this study that eddy-driven advection consists of a part which is resolved by the data and a second part which is subscale and unresolved in the data. With these definitions, the budget of mean temperature and salinity is given by the averaged advection-diffusion Equations 1.1 and 1.2:

$$\frac{\partial \overline{T}}{\partial t} = -\left(\overline{\mathbf{u} \cdot \nabla T} - \nabla \cdot k \nabla \overline{T}\right) - \left(\overline{w \frac{\partial T}{\partial z}} - \frac{\partial}{\partial z} k \frac{\partial \overline{T}}{\partial z}\right) \tag{1.3}$$

$$\frac{\partial \overline{S}}{\partial t} = -\left(\overline{\mathbf{u} \cdot \nabla S} - \nabla \cdot k \nabla \overline{S}\right) - \left(\overline{w \frac{\partial S}{\partial z}} - \frac{\partial}{\partial z} k \frac{\partial \overline{S}}{\partial z}\right) \tag{1.4}$$

The transport terms in the right-hand sides of 1.3 and 1.4 represent the horizontal advection and diffusion (the first two terms) and vertical advection and diffusion (the third and fourth terms). By using the Reynolds averaging (Vallis & Lam, 1996), the horizontal transport of heat is written as:

$$\overline{\mathbf{u} \cdot \nabla T} - \nabla \cdot k \nabla \overline{T} = \overline{\mathbf{u}} \nabla \overline{T} + \overline{\mathbf{u}' \cdot \nabla T'} - \nabla k_{hT} \nabla \overline{T} \tag{1.5}$$

The first term on the right-hand side of 1.5 is the advection by the mean flow, the second is the eddy-induced transport due to mesoscale eddies resolved in the data, the third one represents the smaller scale turbulence unresolved in the data. The eddy-induced advection term $\overline{\mathbf{u}' \cdot \nabla T'}$ is a sum of two components - divergent and rotational (J. Marshall & Shutts, 1981). The divergent component of $\overline{\mathbf{u}' \cdot \nabla T'}$ is due

to the ageostrophic component of the flow. It represents the local contribution of eddy advection to the heat budget.

The mesoscale and sub-mesoscale eddies are in quasigeostrophic balance. A part of the eddy velocity vector (u') is approximately parallel to the ispoycnals (isolines of ρ' and respectively to isotherms for T' and isohalines for S'). The rotational component of the heat advection is due to this part of the flow vanishes in 1.5. It is associated with the formation and propagation of mesoscale eddies through the region. The rotational component of eddy-induced heat advection resolved in the data still contributes to the temperature change through the heat released in the area of eddy decay through the enhancement of irreversible mixing created by eddy stirring and fine-scale patterns. This heat is normally parameterized as $\nabla k_{OC} \nabla \overline{T}$ where k_{OC} is the so-called Osborn-Cox diffusivity (T. Osborn & Cox, 1972). The sub-scale rotational (non-divergent) eddy-driven advection unresolved by the data is normally determined as $\nabla k_K \nabla \overline{T}$. The diffusion coefficient k_K can be locally positive or negative but it vanishes in the equation of globally integrated heat budget. Therefore, the turbulent heat diffusion coefficient k_{hT} in Equation 1.5 is defined (see Abernathey & Marshall, 2013) as the sum of the following components.

$$k_{hT} = k + k_K + k_{OC}$$

The vertical heat transport in Equation 1.3 is

$$\overline{w \frac{\partial T}{\partial z}} - \frac{\partial}{\partial z} k \frac{\partial \overline{T}}{\partial z} = \overline{w} \frac{\partial \overline{T}}{\partial z} + \overline{w' \frac{\partial T'}{\partial z}} - \frac{\partial}{\partial z} k \frac{\partial \overline{T}}{\partial z}$$

The vertical subscale heat transport is normally determined by using models of turbulence (see Burchard & Beckers, 2004)

$$\frac{\partial}{\partial z} k \frac{\partial \overline{T}}{\partial z} - \overline{w' \frac{\partial T'}{\partial z}} = \frac{\partial}{\partial z} k_{vT} \frac{\partial \overline{T}}{\partial z}$$

where k_{vT}, the vertical turbulent heat diffusion coefficient is a function of vertical velocity shear and buoyancy. The same concept of separation of the advective terms into mean and eddy-components apply for the salinity equation. The final form of the equations for salinity and temperature used in this study are

$$\frac{\partial \overline{T}}{\partial t} = -\overline{\mathbf{u}} \cdot \nabla \overline{T} - \overline{w}\frac{\partial \overline{T}}{\partial z} - \overline{\mathbf{u}' \cdot \nabla T'} + \nabla \cdot k_{hT} \nabla \overline{T} + \frac{\partial}{\partial z} k_{vT} \frac{\partial \overline{T}}{\partial z} \tag{1.6}$$

$$\frac{\partial \overline{S}}{\partial t} = -\overline{\mathbf{u}} \cdot \nabla \overline{S} - \overline{w}\frac{\partial \overline{S}}{\partial z} - \overline{\mathbf{u}' \cdot \nabla S'} + \nabla \cdot k_{hS} \nabla \overline{S} + \frac{\partial}{\partial z} k_{vS} \frac{\partial \overline{S}}{\partial z} \tag{1.7}$$

where k_{hS}, k_{vS} are the horizontal and vertical coefficient of salinity turbulent diffusion respectively.

1.4 Heat Budget of the Nordic Seas

The GSR is positioned along the southern boundary of the Nordic Seas with the Atlantic Ocean. The Fram Strait separates Arctic from the Nordic Seas. The waters of the Arctic and Atlantic origin which flow through these straits are transformed by air-sea interaction and mixing in the Nordic Seas. The net effect of the transport through the straits and air-sea fluxes on the heat budget of this ocean basin is given by the integrated equation of temperature (Equation 1.3):

$$\frac{\partial}{\partial t}\int \overline{T} dV = -\int \left(\overline{\mathbf{u}} \cdot \nabla \overline{T} + \overline{w}\frac{\partial \overline{T}}{\partial z}\right) dV - \int \left(\overline{u' \cdot \nabla T'}\right) dV + \int \left(\nabla \cdot k_{hT} \nabla \overline{T}\right) dV + \int \left(\frac{\partial}{\partial z} k_{vT} \frac{\partial \overline{T}}{\partial z}\right) dV$$

The left-hand side represents the rate of change of the basin's heat content H_T where $H_T = \rho c_p \int \overline{T} dV$, ρ is the seawater density, and c_p is the heat capacity. The first integral on the right-hand side can be expanded by using integration by parts in conjunction with the continuity equation:

$$\nabla \cdot u + \frac{\partial w}{\partial z} = 0$$

$$-\int \left(\overline{\mathbf{u}} \nabla \overline{T} + \overline{w} \frac{\partial \overline{T}}{\partial z} \right) dV = -\oint \overline{\mathbf{u}} \cdot \mathbf{n} \overline{T} dA_L$$

Here A_L is the area of the lateral boundary surrounding the region and $\mathbf{n}$ is a unit outward vector normal to the boundary. The condition $\int \overline{w} dA_S = 0$ was assumed, where A_S is the area of the ocean surface. By using the same approach we can express the other volume integrals in the integrated temperature equations:

$$-\int \left(\nabla \cdot \overline{\mathbf{u}' T'} \right) dV = -\oint \overline{\mathbf{u}' T'} \cdot \mathbf{n} dA_L$$

$$\int \left(\nabla \cdot k_{hT} \nabla \overline{T} \right) dV = \oint k_{hT} \mathbf{n} \cdot \nabla \overline{T} dA_L$$

and

$$\int \left(\frac{\partial}{\partial z} k_{vT} \frac{\partial \overline{T}}{\partial z} \right) dV = \int k_{vT} \frac{\partial \overline{T}}{\partial z} dA_S - \int k_{vT} \frac{\partial \overline{T}}{\partial z} dA_B$$

Here A_B is the area of the bottom surface. The final form of the equation of the net heat content of the Nordic Seas is:

$$\frac{1}{\rho c_p}\frac{\partial H_T}{\partial t} = -\oint \overline{\mathbf{u}}\cdot\mathbf{n}\overline{T}dA_L - \oint \overline{\mathbf{u}'T'}\cdot\mathbf{n}dA_L + \oint k_{hT}\mathbf{n}\cdot\nabla\overline{T}dA_L + \int k_{vT}\frac{\partial\overline{T}}{\partial z}dA_S - \int k_{vT}\frac{\partial\overline{T}}{\partial z}dA_B \quad (1.8)$$

The heat content of the basin is a sum of the mean (first term on the right) and eddy-induced (second and third terms on the right) lateral heat transport through the boundaries, the surface net heat flux (the fourth term on the right) and geothermal heat (the last term).

Similarly the equation of salinity content $H_S = \rho\int \overline{S}dV$ is

$$\frac{1}{\rho}\frac{\partial H_S}{\partial t} = -\oint \overline{\mathbf{u}}\cdot\mathbf{n}\ \overline{S}dA_L - \oint \overline{\mathbf{u}'S'}\cdot\mathbf{n}dA_L + \oint k_{hS}\mathbf{n}\cdot\nabla\overline{S}dA_L + \int k_{vS}\frac{\partial\overline{S}}{\partial z}dA_S \quad (1.9)$$

The open boundaries of the Nordic Seas consist of the GSR, Fram Strait and the connection to the Barents and Kara Seas. Equation 1.8 in this case is:

$$\frac{1}{\rho c_p}\frac{\partial H_T}{\partial t} = Fh_{GSR} + Fh_{FS} + Fh_{BK} + Qh_S - Qh_B \quad (1.10)$$

where Fh_{GSR}, Fh_{FS} and $FhBK$ are the lateral mean and eddy-induced fluxes of heat in the GSR, Fram Strait and to the Barents and Kara Seas respectively and shown graphically in Figure 1.5. Qh_S is the integral surface net heat flux, and Qh_B is the geothermal heat. The existing estimates of the Qh_B in the ocean are relatively small with respect to the other terms of Equation 1.10. Similarly, the salt budget of the basin is

$$\frac{1}{\rho}\frac{\partial H_S}{\partial t} = Fs_{GSR} + Fs_{FS} + Fs_{BK} + Qs_B \quad (1.11)$$

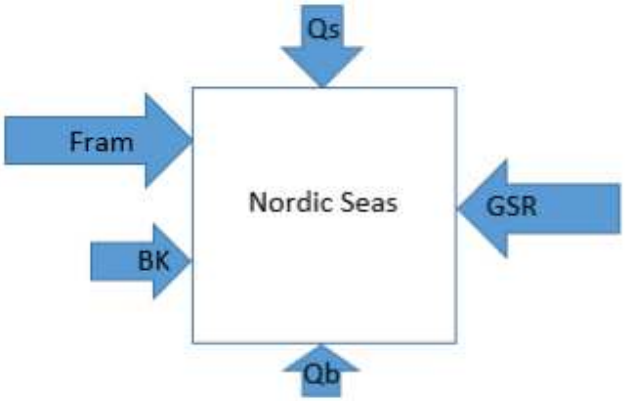

Figure 1.5: Diagram of fluxes into and out of the Nordic Seas. The arrows represent the lateral fluxes into the Nordic Seas through the Fram Strait, Barents and Kara Seas (BK) and over the Greenland Scotland Ridge (GSR) and the surface flux (Q_s) and the geothermal heat (Q_b).

The transport through the GSR involves flow of surface modified Atlantic waters into the Nordic Seas over the Iceland-Faroe Ridge and through the Faroe-Shetland Channel, and a return flow of PW and dense-water overflow into the Atlantic Ocean (Hansen & Østerhus, 2000). The difference in the characteristics of the inflow and outflow through the GSR implies net heat and salt fluxes into the Arctic Mediterranean of about 330 $TW (1\ TW = 10^{12}\ W)$ and $303 \times 10^6\ kg/s$ (Serreze et al., 2006), respectively. The long-term variations in heat and salt transport through the GSR influences the climate variability of the Arctic Mediterranean (Yashayaev & Seidov, 2015); (Polyakov, Alekseev, et al., 2004). Understanding the dynamics and variability of this transport is essential for understanding of the meridional exchange of energy and mass in the subarctic.

1.5 Aims and Objectives

1.5.1 Research Questions

- What role, if any, the heat and salt transports through the GSR play in the long-term interannual and decadal variability of the Nordic Seas?
- What are the characteristics of the convergence of *surface* mean and eddy induced transport of heat in the ocean region adjacent to the GSR?
- What is the spatial and temporal variability of the convergence of mean advective heat and salt transport in the water ocean region adjacent to the GSR?

1.5.2 Aim

To explore and further understand the processes of exchange between the Arctic Mediterranean and North Atlantic.

1.5.3 Objectives

1. To estimate interannual variability of temperature and salinity transport through the GSR and assess its impact on the heat and salt budgets of the Nordic Seas using ensemble simulations with a global ocean model.

2. To explore the physical causes of past long-term variability in the heat and salt content in the Nordic Seas.

3. To assess the characteristics of mesoscale eddies in the ocean region adjacent to the GSR using ocean satellite and in-situ observations.

4. To assess the mean and eddy induced fluxes of heat and salt in the surface layer using observations.

5. To explore the vertical structure of the heat and salt flux convergence by using ocean reanalysis.

1.5.4 Layout of the Dissertation

The study is composed of three sub-projects. Chapter 2 presents results from a model study of long-term variability of volume and heat transport through the GSR and its impact on the Nordic Seas. In Chapter 3 the mean and eddy-driven heat advection in the surface ocean region adjacent to the GSR derived from satellite

altimetry are discussed. Chapter 4 presents results from a study of vertical structure of convergence of mean advection of temperature and salinity. A discussion of key results and conclusions of the dissertation is presented in Chapter 5.

This thesis is written in manuscript format. The content is presented in three journal articles that have either been published in journals or are being prepared for publication. They are written as standalone articles and therefore some information may be repeated in the introduction. Memorial University thesis guidelines requires each article be presented with its associated bibliography with an additional bibliography for the entire thesis. All appendices are appended after the thesis bibliography.

1.6 Co-Authorship statement

Authorship for the research paper presented in Chapter 2 is in the following order: Sarah Lundrigan and Dr. Entcho Demirov (thesis supervisor). Model implementation, model runs and analysis of results were performed by Ms. Lundrigan with direction from Dr. Demirov. The manuscript was prepared by Ms. Lundrigan and critically reviewed by Dr. Demriov.

Authorship for the research paper presented in Chapter 3 is in the following order: Sarah Lundrigan and Dr. Entcho Demirov. Experimental design and analysis was performed by Ms. Lundrigan. The manuscript was prepared by Ms. Lundrigan and critically reviewed by Dr. Demirov.

Authorship for the research paper presented in Chapter 4 is in the following order: Sarah Lundrigan and Dr. Entcho Demirov. The data analysis was performed by Ms. Lundrigan. The manuscript was prepared by Ms. Lundrigan and critically reviewed

by Dr. Demirov.

References

Abernathey, R. & J Marshall (2013). "Global surface eddy diffusivities derived from satellite altimetry". In: *Journal of Geophysical Research: Oceans* 118(2), pp. 901–916. DOI: https://doi.org/10.1002/jgrc.20066.

Bersch, M. (1995). "On the circulation of the northeastern North Atlantic". In: *Deep Sea Research Part I: Oceanographic Research Papers* 42(9), pp. 1583–1607.

Blindheim, J. & S Osterhus (2005). "The Nordic Seas, main oceanographic features". In: *Geophysical Monograph-American Geophysical Union* 158, p. 11. DOI: https://doi.org/10.1029/158GM03.

Burchard, H. & J. Beckers (2004). "Non-uniform adaptive vertical grids in one-dimensional numerical ocean models". In: *Ocean Modelling* 6(1), pp. 51–81.

Chelton, D., R. DeSzoeke, et al. (1998). "Geographical variability of the first baroclinic Rossby radius of deformation". In: *Journal of Physical Oceanography* 28(3), pp. 433–460.

Coachman, L.K. & K. Aagaard (1974). "Physical oceanography of Arctic and subarctic seas". In: *Marine geology and oceanography of the Arctic seas*. Springer, pp. 1–72.

Dickson, B., J. Meincke & P. Rhines (2008). "Arctic-Subarctic ocean fluxes: Defining the role of the Northern Seas in climate. A general introduction". In: *Arctic-Subarctic Ocean Fluxes - Defining the role of the northern seas in climate*. Ed. by R.R. Dickson, J. Meincke & P. Rhines. Springer, pp. 1–14.

Dickson, R.R. & J. Brown (1994). "The production of North Atlantic Deep Water: sources, rates, and pathways". In: *Journal of Geophysical Research: Oceans* 99(C6), pp. 12319–12341. DOI: https://doi.org/10.1029/94JC00530.

Dong, C. et al. (2014). "Global heat and salt transports by eddy movement". In: *Nature communications* 5, p. 3294.

Eldevik, T. et al. (2009). "Observed sources and variability of Nordic seas overflow". In: *Nature Geoscience* 2(6), p. 406.

Gill, A. (1982). *Atmosphere—ocean dynamics*. Elsevier.

Hansen, B. & S Østerhus (2000). "North atlantic–nordic seas exchanges". In: *Progress in oceanography* 45(2), pp. 109–208. DOI: https://doi.org/10.1016/S0079-6611(99)00052-X.

Ince, E. et al. (2019). "ICGEM–15 years of successful collection and distribution of global gravitational models, associated services, and future plans". In: *Earth System Science Data* 11(2), pp. 647–674.

Isachsen, P.E., I Koszalka & JH LaCasce (2012). "Observed and modeled surface eddy heat fluxes in the eastern Nordic Seas". In: *Journal of Geophysical Research: Oceans* 117(C8). DOI: https://doi.org/10.1029/2012JC007935.

Johannessen, O.M., K. Lygre & T. Eldevik (2005). "Convective chimneys and plumes in the Northern Greenland Sea". In:

Karimova, S. (2017). "Performance of gridded and along-track altimetry products in eddy manifestation in the western mediterranean". In: *2017 IEEE International Geoscience and Remote Sensing Symposium (IGARSS)*. IEEE, pp. 2991–2998.

Latarius, K. & D. Quadfasel (2010). "Seasonal to inter-annual variability of temperature and salinity in the Greenland Sea Gyre: heat and freshwater budgets". In: *Tellus A: Dynamic Meteorology and Oceanography* 62(4), pp. 497–515.

Marshall, J. & G. Shutts (1981). "A note on rotational and divergent eddy fluxes". In: *Journal of Physical Oceanography* 11(12), pp. 1677–1680. DOI: https://doi.org/10.1175/1520-0485.

Mauritzen, C. (1996a). "Production of dense overflow waters feeding the North Atlantic across the Greenland-Scotland Ridge. Part 1: Evidence for a revised circulation scheme". In: *Deep Sea Research Part I: Oceanographic Research Papers* 43(6), pp. 769–806. DOI: https://doi.org/10.1016/0967-0637(96)00037-4.

Mauritzen, C. (1996b). "Production of dense overflow waters feeding the North Atlantic across the Greenland-Scotland Ridge. Part 2: An inverse model". In: *Deep Sea Research Part I: Oceanographic Research Papers* 43(6), pp. 807–835. DOI: 10.1016/0967-0637(96)00038-6..

Meincke, J, B Rudels & HJ Friedrich (1997). "The Arctic Ocean–Nordic Seas thermohaline system". In: *ICES Journal of Marine Science* 54(3), pp. 283–299.

Mohn, H. (1887). *Den Norske Nordhavsekspedition 1876-1878. Temperatur og Stromingar*. Version Bd II. Christiania, Norway: Nordhavets Dybder.

Myers, P., N. Kulan & M. Ribergaard (2007). "Irminger water variability in the West Greenland Current". In: *Geophysical Research Letters* 34(17). DOI: https://doi.org/10.1029/2007GL030419.

Nurser, AJG & S Bacon (2014). "The rossby radius in the Arctic Ocean". In: *Ocean Science* 10(6), pp. 967–975.

Osborn, T. & C. Cox (1972). "Oceanic fine structure". In: *Geophysical & Astrophysical Fluid Dynamics* 3(1), pp. 321–345. DOI: https://doi.org/10.1080/03091927208236085.

Pawlowicz, R. et al. (1995). "Thermal evolution of the Greenland Sea Gyre in 1988–1989". In: *Journal of Geophysical Research: Oceans* 100(C3), pp. 4727–4750.

Pickart, R., D. Torres & P. Fratantoni (2005). "The east Greenland spill jet". In: *Journal of Physical Oceanography* 35(6), pp. 1037–1053. DOI: https://doi.org/10.1175/JPO2734.1.

Polyakov, I., G. Alekseev, et al. (2004). "Variability of the Intermediate Atlantic Water of the Arctic Ocean over the Last 100 years." In: *Journal of Climate* 17(23). doi:10.1175/JCLI-3224.1, pp. 4485–4497.

Rhein, M. (1996). "Convection in the Greenland Sea, 1982–1993". In: *Journal of Geophysical Research: Oceans* 101(C8), pp. 18183–18192.

Rudels, B., E. Fahrbach, et al. (2002). "The East Greenland Current and its contribution to the Denmark Strait overflow". In: *ICES Journal of Marine Science* 59(6), pp. 1133–1154. DOI: https://doi.org/10.1006/jmsc.2002.1284.

Rudels, B., H. Friedrich & D. Quadfasel (1999). "The Arctic circumpolar boundary current". In: *Deep Sea Research Part II: Topical Studies in Oceanography* 46(6-7), pp. 1023–1062. DOI: https://doi.org/10.1016/S0967-0645(99)00015-6.

Rudels, B., D. Quadfasel, et al. (1989). "Greenland Sea convection in the winter of 1987–1988". In: *Journal of Geophysical Research: Oceans* 94(C3), pp. 3223–3227.

Serreze, M. et al. (2006). "The large-scale freshwater cycle of the Arctic". In: *Journal of Geophysical Research: Oceans* 111(C11). DOI: https://doi.org/10.1029/2005JC003424.

Straneo, F. (2006). "Heat and freshwater transport through the central Labrador Sea". In: *Journal of Physical Oceanography* 36(4), pp. 606–628. DOI: https://doi.org/10.1175/JPO2875.1.

Våge, K. et al. (2011). "The Irminger gyre: circulation, convection, and interannual variability". In: *Deep Sea Research Part I: Oceanographic Research Papers* 58(5), pp. 590–614. DOI: https://doi.org/10.1016/j.dsr.2011.03.001.

Vallis, G.K. & L. Lam (1996). "From Laminar Flow to Turbulence". In: *An introduction to nonlinear physics*, pp. 308–357.

Wunsch, C. (1999). "Where do ocean eddy heat fluxes matter?" In: *Journal of Geophysical Research: Oceans* 104(C6), pp. 13235–13249. DOI: https://doi.org/10.1029/1999JC900062.

Yashayaev, I. & D. Seidov (2015). "The role of the Atlantic Water in multidecadal ocean variability in the Nordic and Barents Seas". In: *Progress in Oceanography* 132, pp. 68–127. DOI: https://doi.org/10.1016/j.pocean.2014.11.009.

Zhu, J & E Demirov (2011). "On the mechanism of interannual variability of the Irminger Water in the Labrador Sea". In: *Journal of Geophysical Research: Oceans* 116(C3). DOI: https://doi.org/10.1029/2009JC005677.

Connecting Text

The first article in this thesis addresses objectives 1 and 2 described in Section 1.5.3.

It investigates the interannual and decadal variability of the Nordic Seas. Results from ensemble model simulations are used to asses the impact of the heat flux through the lateral boundaries of the Nordic Seas on its heat budget. The ocean model is a coarse-resolution global circulation model forced with surface fluxes from the reanalysis of the National Center for Environmental Predictions (NCEP). The model results focus specifically on the role of the imbalance of the lateral fluxes of heat through the GSR and Fram Strait on the strong events of interannual ocean variability like the Great Salinity Anomaly and warming of the Nordic Seas in the late 1980s early 1990s.

This article appeared as S. Lundrigan & E. Demirov (2012) in *Atmosphere Ocean*.

Chapter 2

Long-Term Variability of Volume and Heat Transport in the Nordic Seas: A Model Study

2.1 Abstract

The article presents results from a model study of interannual and decadal variability of the Nordic Seas. Fifty years of simulations are conducted in an initial condition ensemble mode forced with the NCEP reanalysis. We study two major events in the interannual and interdecadal variability of the Nordic Sea during the past fifty years: the Great Salinity Anomaly in the 1960s and early 1970s and the warming of Arctic and subarctic in the late 1990s.

Previous studies demonstrated that the Great Salinity Anomaly observed in the sub-Arctic in 1960 was originally generated by intensified sea-ice and fresh water

inflow from Arctic Ocean. Our model results demonstrate that the increase in the transport of fresh and cold waters through the Fram Strait in the 1960s was concurrent with a reduction in the meridional water exchange through the Greenland Scotland Ridge. The resulting imbalance in salinity and heat fluxes through the two straits contributed additionally to the freshening of the water masses of the Nordic Seas and intensified the Great Salinity Anomaly in the Nordic Seas.

The warming of the Atlantic Waters in the Nordic Seas and Arctic Ocean in recent decades had an important impact on the variability of these two ocean basins. The observations and model results suggest that the warming of sub-polar Atlantic Ocean in the late 1990s had a significant contribution to this process. The warming of the Atlantic Water (AW) in the Nordic Seas, however, started earlier in the 1980s and according to our model results was triggered by the disbalance in the lateral heat fluxes through the straits. In the late 1980s the AW transport over the Greenland-Scotland Ridge was stronger than normal while the exchange through the Fram Strait was close to normal. The related imbalalnce in the lateral heat fluxes through the straits warmed up the Nordic Seas and caused an increase in the temperature of the Atlantic Water inflow to the Arctic in late 1980s, i.e. about a decade earlier than the warming of the source of AW in the sub-polar North Atlantic. The model results suggest that the disbalance of lateral heat and salinity fluxes through the straits connecting the Nordic Seas with the North Atlantic and Arctic can potentially amplify the interannual variability in the subarctic.

2.2 Introduction

The subarctic ocean plays an important role in the climate system. Previous studies demonstrated that the interannual variability in this region has an impact on major circulation patterns, water mass properties and sea-ice (B. Dickson, J. Meincke & P. Rhines, 2008; Hakkinen & P.B. Rhines, 2004; Lohmann, Drange & Bentsen, 2008; Marsh et al., 2008; Schlichtholz, 2011). Driven primarily by changes in atmospheric circulation regimes (Lohmann, Drange & Bentsen, 2008) interannual variability in this ocean region includes influences influences on the meridional exchange of fresh water, sea-ice and heat between the North Atlantic and Arctic (Hakkinen & P.B. Rhines, 2004) with ultimately a potential strong feedback on weather and climate (P. Rhines, Häkkinen & Josey, 2008). The Nordic Seas (Figure 2.1(a)) are located between the Arctic and the North Atlantic and play an important role for the variations of the meridional heat and volume fluxes (Orvik & Niiler, 2002). In this article we discuss the interannual variability of the Nordic seas and their impact on the volume and heat exchange between the Arctic Ocean and sub-polar North Atlantic. More specifically we focus on two events that recently had a strong signature in the interannual variability of the polar ocean. These are the Great Salinity Anomaly (R. Dickson et al., 1988) and warming of the Arctic and subarctic in the 1990s (Quadfasel et al., 1991).

The largest sea-ice and fresh water export from the Arctic Ocean takes place through the Fram Strait. In the Nordic Sea the sea-ice/surface fresh waters are carried southward by the Eastern Greenland Current. R. Dickson et al. (1988) and Belkin et al. (1998) suggested that the stronger than normal advection of Arctic Waters

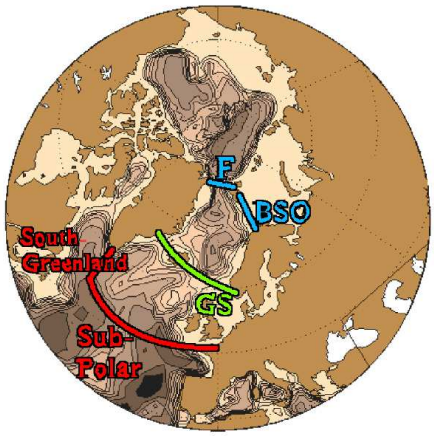

(a)

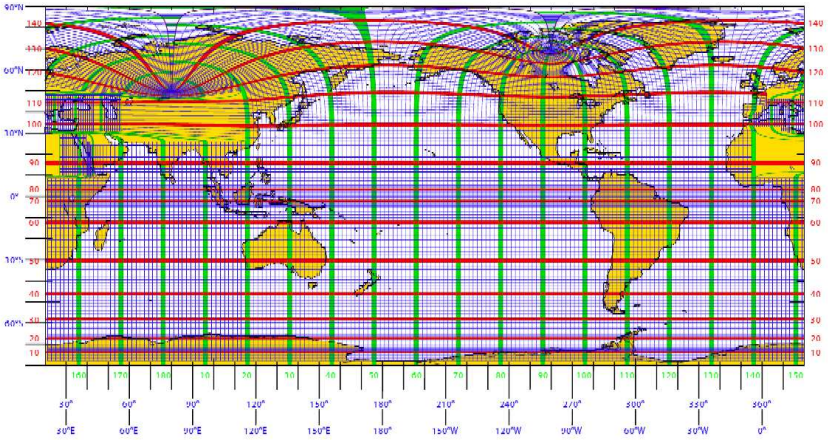

(b)

Figure 2.1: (a) Sections used to study climatic characteristics and variability of fluxes in and out of the Nordic and Sub-polar seas. F- Fram Strait, BSO- Barents Sea Opening, GS- Greenland Scotland Ridge. The "South Greenland" and "Sub-Polar" lines define the boundary of what is defined as the Sub-Polar Ocean. (b) Two degree global grid (ORCA2) used in model simulations (NEMO (Nucleus for European Modelling of the Ocean), 2011)

in the late 1960s and early 1970s created a cold and fresh anomaly, known as the Great Salinity Anomaly (GSA) which propagated cyclonically through the subarctic for about fifteen years. Mysak, Manak & Marsden (1990) and Mysak & Power (1992) explained the formation of the GSA with the existence of a teleconnection pattern with origin in the western Arctic Ocean. The existing observations suggest that when the GSA propagates in the Nordic Seas and sub-polar North Atlantic it tends to intensify locally. In particular, as the GSA propagated through the Labrador sea, it was shown that the GSA can be amplified by the fresh water inflow from the Hudson Bay (Hilmer & Jung, 2000) and modulated by the variations in deep convection (Khatiwala, Schlosser & Visbeck, 2002).

R. Dickson et al. (1988) found that in the 1960s there were at least two processes in that amplified the GSA the Nordic Seas. (1) The increased contribution of the Polar Waters in the Eastern Greenland and Eastern Icelandic Current. Both current systems became colder and fresher than usual. The Eastern Greenland Current expanded, and the Eastern Icelandic Current which is normally ice-free, was transporting ice in the late 1960s. (2) The low salinity of the surface layer north of Iceland strengthened the vertical stratification and prevented these waters from mixing with intermediate and deep saltier waters. That kept the low salinity anomaly stable and expanding. In this article we study another mechanism that may potentially have strengthened the GSA in the Nordic Seas in the 1960s. It is related to specific variations in the local heat and salt balance of the basin at that time.

Observational studies (Quadfasel et al., 1991; Polyakov, Alekseev, et al., 2004) revealed a warming trend in the Atlantic Water (AW) layer in the Arctic in the 1990s. The mechanism of this warming is still not well known. There are in general

two main hypotheses about the causes of this event. The model results of Zhang, Rothrock & Steele (1998); Häkkinen & Geiger (2000) suggest that the inflow of AW into the Arctic intensified in the 1990s. Zhang, Rothrock & Steele (1998) and Aksenov et al. (2010) found that the increase in the volume inflow of the AW occurred mostly via the Barents Sea route. Häkkinen & Geiger (2000) related the intensified AW inflow with a shift in the Arctic Ocean in the early 1990s.

The second hypothesis relates the warming of the AW in Arctic with a shift in atmospheric conditions over the Nordic Seas. R.R. Dickson, J. Osborn, et al. (2000) suggested that a reduction in the surface heat loss to the atmosphere and warming of the AW in the Nordic Seas was related to the rising of the NAO index in the early 1990s.

Hydrographic observations (S. Østerhus & Gammelsrød, 1999; Tereshchenko, 1997) confirm (see also Section 2.4) that warming in the Nordic Seas (S. Østerhus & Gammelsrød, 1999) in the 1980s correlates well with the temperature increase of the AW (Tereshchenko, 1997) inflow to the Arctic. In this article we study another possible mechanism of the AW warming in Arctic which is related to the local heat balance of the Nordic Seas.

The article is organized as follows: Section 2.3 describes the model set up, Section 2.4 presents some characteristics of recent variability of Arctic and subarctic from model and observations. Section 2.5 discusses the mean circulation and transports of the Nordic Seas. Section 2.6 discusses the effect of the variability in the volume fluxes through the straits and their impact on the Nordic Seas and on the local amplification of the GSA and warming in the 1990s. Finally, Section 2.7 offers conclusions.

2.3 Model Setup

In this study we use a coupled ocean and sea-ice models OPA 9.0 (Madec, 2008). It is a z-coordinate, primitive equation, free surface ocean model coupled with the multi-layered sea-ice LIM2 model (T.Fichefet & M.A.Morales Maqueda, 1997). The equation of state is represented using the formulation of Jackett & McDougall (1995). Isopycnical eddy-induced advection is parameterized following Gent & McWilliams (1990). Lateral mixing for tracers is defined along isopycnal surfaces. Vertical mixing coefficients are calculated by using level-1.5 turbulence model of (Blanke & Delecluse, 1993). Lateral momentum mixing is biharmonic along the model level surfaces. Double diffusion mixing is computed following the Merryfield, Holloway & Gargett (1999) parameterization. Advection in the bottom layer is improved through application of the Beckmann & Döscher (1997) scheme for geopotential-coordinate models.

The sea-ice model is the Louvain-la-Neuve sea ice model (LIM). It is a dynamic-thermodynamic model specifically designed for climate studies (T.Fichefet & M.A.Morales Maqueda, 1997; Fichefet & M.A. Maqueda, 1999) and uses a viscous-plastic rheology (Hibler, 1979). The thermodynamic part of LIM uses a three-layer model (one layer for snow and two layers for ice) for sensible heat storage and vertical heat conduction within snow and ice.

The ocean and sea-ice models equations are written in a curvilinear coordinate system. The ORCA2-LIM model grid configuration is based on a 2 degree Mercator mesh. It has 31 vertical levels, 20 of which are in the top 500 m. In the northern hemisphere the mesh has two poles (Figure 2.1)b. The mean grid spacing is about 2/3 of the nominal value or 1.3 degrees. The meridional grid spacing is about 0.5

degrees near the equator to improve the equatorial dynamics and increases to about $2^o \cos(\phi)$ at 20 degrees latitude. The highest grid resolution is about 65 km in Arctic. The bottom topography is computed from ETOPO2 data set.

The model is initialized with Levitus climatology (Antonov et al., 2005). A 30 year spin-up is forced using NCEP-NCAR monthly mean climatological fields for atmospheric 2 m temperature, humidity, wind speed at 10 m, total cloudiness and surface wind stress. The river discharge is defined from monthly mean climatology. Surface fluxes are computed by using standard bulk empirical formulas and model SST.

The model is spun up by a 30 years run with seasoonal mean surface forcing. After 30 years of simulations, the global model does not reach an equilibrium state in a stric sense. However as mentioned by Timmermann et al. (2005) "in contrast to the low latitude ocean, in which deep water properties change on time scales of decades to centuries, communication between the surface and the deep ocean in polar regions occurs as part of the seasonal signal or an interannual variability. So, in order to investigate ice-ocean interaction, the model does not need to be integrated for hundreds of years provided that areas that feature a much slower variability are initialized close to reality". Additionally in our simulations, a spectral nudging scheme (Thompson et al., 2006) is applied to reduce model bias. The model temperature and salinity are nudged towards the observed climatology with a prescribed frequency-wavenumber band and is not constrained outside of this interval.

After the initial period of spin up, the model is run for 50 years, from 1948-2005, using the NCEP/NCAR forcing. Six configurations were then chosen to form the initial conditions for each ensemble member after the first 37 years of simulation

with 6 hourly NCEP/NCAR forcing. The chosen years for the initial conditions were 1985, 1989, 1992, 1994, 1996 and 1997. Each of these 6 initial conditions were used to run ensemble members from 1948-2005 saving the output monthly for analysis. The output from 1965-2005 is used for analysis in this study. The results presented in this paper are an average of the ensemble members and the error is the standard deviation between the ensemble members.

In a previous study Timmermann et al. (2005) validated the OCRA2_LIM model configuration and assessed its skills in representing high-latitude processes. These authors demonstrated that the ORCA2_LIM model represents realistically large scale seasonal and interannual variability in the sea-ice extent and drift, the major patterns of circulation and the location of the main sites of deep convection. Here we use the ORCA2_LIM model configuration to study the subarctic interannual variability and related meridional volume and heat fluxes through the Fram Strait and over the Greenland-Scotland Ridge.

2.4 Arctic and Subarctic Temperature Interannual Variability from Observations and Model Simulations

Figure 2.2 shows the observed interannual variability of temperature characteristics of three regions. It shows the heat balance of the sub-polar North Atlantic (Figure 2.2a), three-year annual mean $0-200\ m$ temperature anomaly at the Kola transect in the Barents Sea and three year mean July-September SST anomaly at Ocean Weather

Station Mike (Figure 2.2b)and temperature of the core of the AW in Arctic (Figure 2.2c). The temperature in the three regions decreases in the 1960s and 1970s and increases after 1995. In the late 1980s and early 1990s the surface and intermediate water masses of the sub-polar North Atlantic were colder than usual (see Figure 2.2a, (Straneo et al., 2009; Yashayaev, 2007)). Surface cooling and winter deep convection during this period were stronger than normal and the temperatures and salinities in the surface and intermediate Labrador Sea water were the coldest observed in this region since the 1950s (Yashayaev, 2007). During the same period the AW started warming up in the Nordic Seas and Arctic (see Figure 2.2b,c).

The variations in model heat content in Arctic and subarctic are shown on Figure 2.3. Simulated temperatures follow broad changes found in observations, including cooling of the polar ocean in the 1960s and 70s followed by warming after 1995 In particular the sub-polar ocean in the model was colder than normal between 1989 and 1994 (Figure 2.3a) and started warming up only in 1995. The warming of the Nordic Seas and the AW in Arctic started earlier, in late 1980s and early 1990s. This increase in the temperature developed locally and appears to be related to the local variability in Nordic Seas. Our estimations (not shown here) suggest that the contributions of the lateral heat transport through the Fram Strait and over the Scotland-Greenland Ridge dominate the heat balance of the Nordic Sea during the studied period.

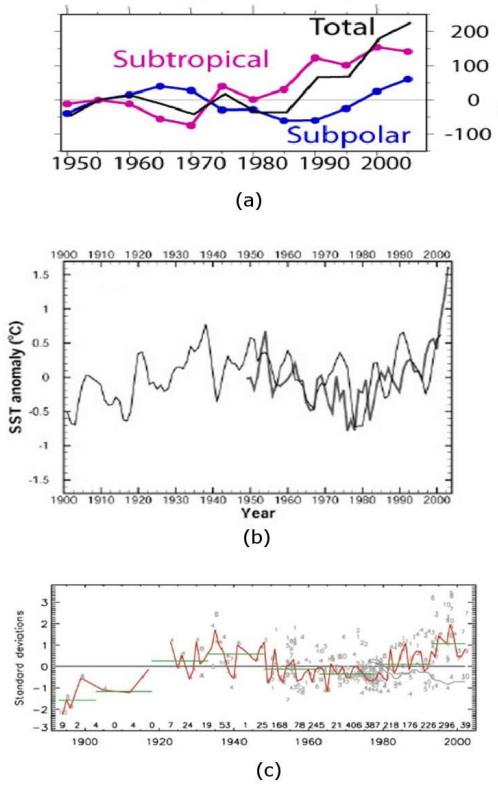

Figure 2.2: (a) Time series of heat storage anomaly (10^{20} J) for the upper ocean ($0 - 1200\ m$) of the subtropical (20^o-50^oN), the subpolar (50^oN to Davis Strait and the Greenland-Scotland Ridge) basins of the North Atlantic and for the two combined (reproduced from (Straneo et al., 2009) by permission). (b) Observed three-year annual mean $0 - 200\ m$ temperature variations at the Kola transect in the Barents Sea (70^o30'-72^o30'N, 33^o30'E, thin line, Tereshchenko (1997) and observed three-year mean July-September SST variations at OWS M (66^oN, 2^oE, thick gray line (reproduced from Drange et al. (2005) by permission of American Geophysical Union) and (c) observed temperature of the core of the Atlantic water mass in the Arctic Ocean (reproduced from Polyakov, Alekseev, et al. (2004) by permission of the American Meteorological Society).

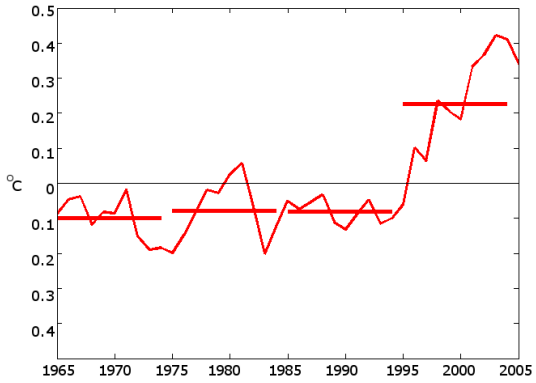

(a)

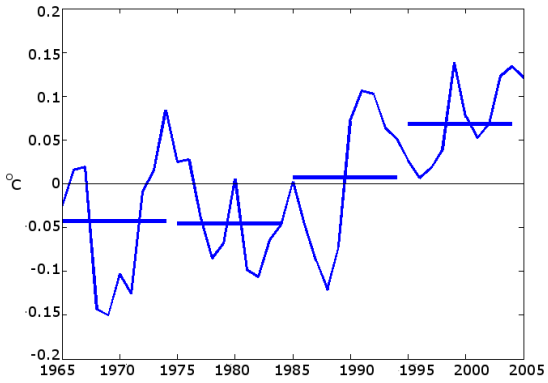

(b)

Figure 2.3: Standard Deviations in the average temperature of the (a) Sub-polar ocean, and (b) Nordic Seas.

2.5 Model Simulation of Mean Circulation in the Nordic Sea

The schematic circulation in the surface layer of the Nordic Seas and the simulated barotropic streamfunction averaged over the period 1965 - 2005 are shown on Figure 2.4. The AW flows into the Nordic Seas by crossing the Greenland-Scotland Ridge. It does so in three branches: the Iceland, Faroe and Shetland branches (Figure 2.4). The warmest and saltiest water is flowing over the eastern side of the ridge and the coldest and freshest over the western side. North of the Greenland-Scotland Ridge the main part of the Atlantic Water flows along the coast of Norway as a slope current with a speed between 5 and 20 cm/s (Haugan et al., 1991). This slope current follows the Norwegian Coast until it splits so that a small part of the current enters the Barents Sea while the remainder continues north to Spitsbergen. This portion of the current either passes through the Fram Strait with a velocity of about 2.0 cm/s - 5.5 cm/s or recirculates in the Nordic Seas (Schauer et al., 2008). The average volume flux of Atlantic Water through the Fram Strait, defined as water above 1^oC, was about 5 Sv in the late 1990s (Schauer et al., 2008). The Fram Strait is also a passage for the cold Arctic waters to enter the Nordic Seas. The cold fresh water enters the Nordic Seas with an average annual speed of 8 cm/s (Muench et al., 1992) as the East Greenland Current. This current follows the coast of Greenland southward from the Fram Strait to the tip of Greenland.

Both the observations and model results show that the circulation is cyclonic (Voet et al., 2010; Isachsen, J.H LaCasce, et al., 2003; Rossby, Prater & Søiland, 2009) in each of the basins in the Nordic Seas with stronger velocities at the rims. An exception

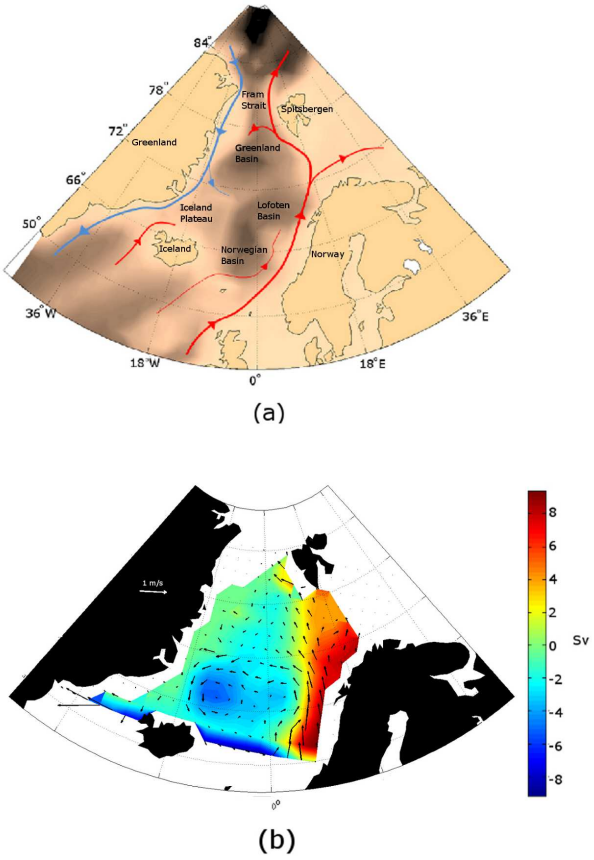

Figure 2.4: Mean Circulation in the Nordic Seas. (a) Major Currents and (b) Mean Barotropic Streamfunction calculated from model results. Arrows indicate model transport over study period.

is the Lofoten Basin where the flow has cyclonic vorticity in the western part and anticyclonic vorticity near the coasts of Norway. The strongest barotropic currents are in the Norwegian Basin and Iceland Plateau. The volume transport here is about 10-15 Sv which is close to observational estimate of Voet et al. (2010). The Norwegian Atlantic Current branches in the northern part of the Norwegian Basin. Part of the AW is recirculated here within the cyclonic gyre in this basin and mixes with the waters in the gyre. The dominant mode of variability of the basin circulation is related to changes in the intensity of this recirculation.

Figure 2.5a shows the 1^{st} Empirical Orthogonal Function (EOF) of satellite sea surface altimetry (AVISO, 2011) and Figure 2.5b shows the 1^{st} EOF of the barotropic streamfunction for the model results. Both are calculated for the period from 1993 to 2005. The sea surface height is the geostrophic stream function for the barotropic flow in the deep part of the ocean. Therefore, suing sea level anomalies the barotropic streamfunction can be calculated. The variability of the model circulation resembles the major elements of the structure of the first ssh EOF in the deep part of the ocean. The spatial pattern of the first dominant mode of variability in both model and data is related mostly to the variations in the intensity of the cyclonic gyre in the Norwegian Sea and Iceland Plateau. The model also captures a prominent cycle in the strength of the first EOF of SSH. The Principal component for both the ssh observations and model stream function show a trend of decrease in the strength of the cyclonic circulation in the Norwegian Sea from 1993 to 1998. Later the two principle components show a long term trend of increase in the circulation intensity from 1998 to 2005.

The volume flux and temperature of the AW averaged over the period 1999-

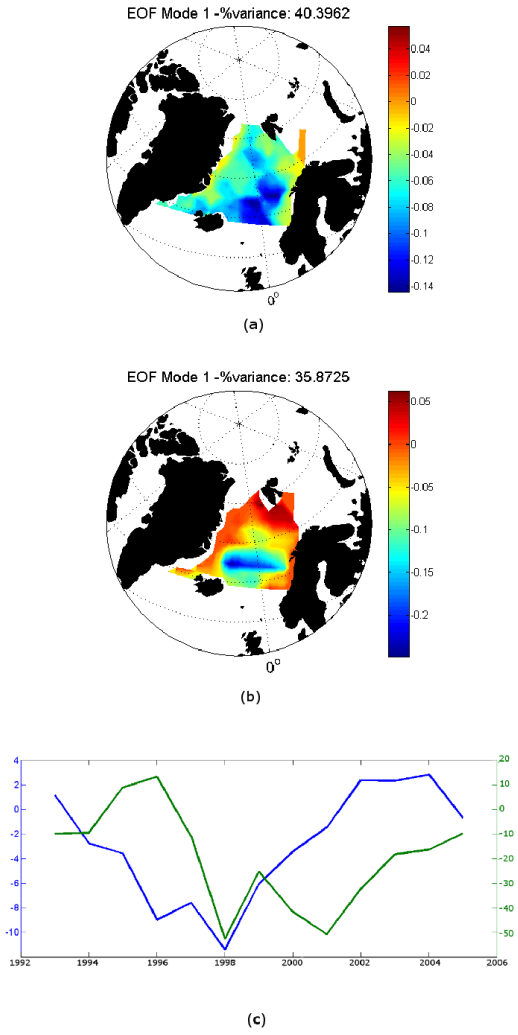

Figure 2.5: Main mode of variations in circulation in the Nordic Seas. The 1^{st} EOF of (a) SSH from satellite altimetery (AVISO, 2011) and (b) barotropic streamfunction calculated from model results. The principal component of the1^{st} EOF for observations (green line) and for the calculated barotropic stream function (blue) are shown in (c). All EOFs here are calculated for the period 1993-2005 for the ice-free months only.

	Modeled			Observations		
Branch	**Vol. (Sv)**	**T^{o}C**	**Salinity**	**Vol.(Sv)**	**T^{o}C**	**Salinity**
Iceland	1.6 ± 0.1	5.7 ± 0.2	35.10 ± 0.03	0.8 ± 1	6	< 35
Faroe	3.1 ± 0.4	6.0 ± 0.2	35.21 ± 0.04	3.8 ± 1	8.2	35.23
Shetland	4.0 ± 0.3	9.1 ± 0.1	35.28 ± 0.02	3.8 ± 1	9.5	35.32
Total Atl.	8.7 ± 0.8	6.9 ± 0.5	35.19 ± 0.03	8.5	8.5 ± 3	35.25

Table 2.1: Table of modeled and observed (Hansen, S. Osterhus, et al., 2008) Greenland-Scotland Ridge Atlantic Water characteristics

2001 for the three branches of the Greenland Scotland ridge are shown on Table 2.1. The model results are given with in error calculated as standard deviations of each quantity in ensemble runs. The results are compared with the observations for the same period of time given by Hansen, S. Osterhus, et al. (2008). The Atlantic Water of the model results is defined using the same definition as the observations in Hansen, S. Osterhus, et al. (2008). The mean volume transports through all three branches of the AW (see Table 2.1) correspond to data within the limits of the uncertainty of the model solutions and observations. The temperature of the AW in all of the branches over the Greenland-Scotland Ridge is cooler for the model results than for the observations. The modelled AW salinity is higher near the west coast of Iceland and less in the two other branches when compared with observations. However, these differences are within the uncertainty of observations as defined by Hansen, S. Osterhus, et al. (2008).

The main part of the AW passes through the Faroe and Shetland Branches. The flow through the Iceland Branch is cooler and fresher than the other two due to the

close proximity of the cold, fresh East Greenland Current. The observed northward volume flux through the Fram Strait is 12±1 Sv (Schauer et al., 2008). It is lower, 7.5± 0.7 Sv in the model results. Similarly, the southward volume flux from observations is 14 ± 1 Sv and is 10.7 ± 0.6 Sv from model results. The total volume flux through the Fram Strait calculated from model results is 3.1 ± 1 Sv and corresponds to the observed 2 ± 2 Sv (Schauer et al., 2008) within the uncertainty of observations and model simulation. This net inflow flux into the Nordic Seas balances the net inflow from Pacific Ocean into the Arctic.

2.6 Interannual Variability of the Nordic Seas from 1965 to 2005

Figure 2.6 shows the time evolution of the anomalies of northward and southward volume annual mean fluxes separately for the Greenland-Scotland Ridge (GS) and the Fram Strait (FS). The variation in the model solution is computed from the ensembles and accounts for error due to uncertainty in the initial conditions. There is relatively high uncertainty in the amplitude of quasi-decadal variation of the FS flux between 1980 and 1990 and in the GS volume transport from 1973 to 1978. Here we focus our discussion on two periods when all ensemble members suggest that there was strong inter-annual and inter-decadal variability in the volume transport through the GS and FS. The first one is the late 1960s and beginning of the 1970s and the second one is the period 1980 - 2005.

In the late 1960s the model water exchange through the FS is intensified and its

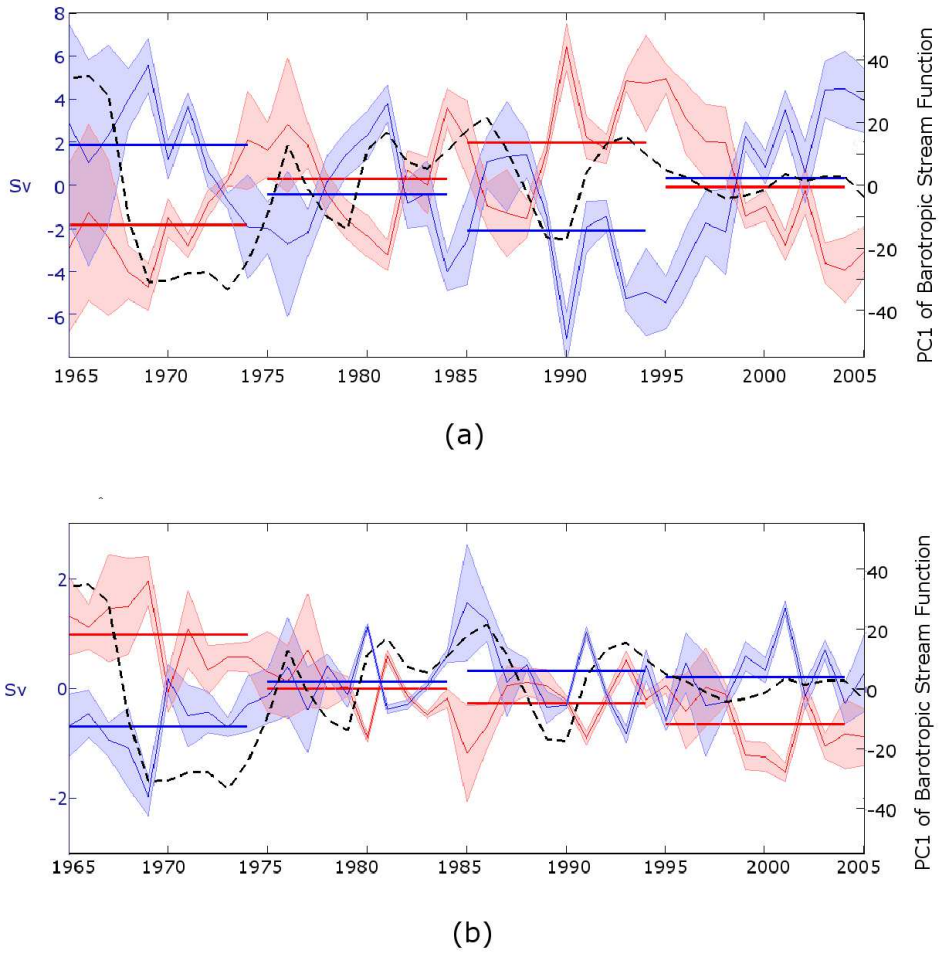

Figure 2.6: Northward (pink) and Southward (blue) volume fluxes (a) over the Greenland-Scotland Ridge and (b) through the Fram Strait. Where north flows are positive and southward negative. The dashed black line in both (a) and (b) indicates the principal component for the 1^{st} EOF of the barotropic stream function for the period 1965 to 2005 (calculated from model results).

anomaly reaches the highest value of 2 Sv in 1969. This increase in the transport is balanced approximately by the outflow to the Arctic Ocean. The model volume fluxes in and out the Nordic Seas through the GS during the same period of time was weaker than normal. The flow anomaly reached its lowest value of about -4 Sv in the 1969. These variations in the transport through the GS and FS in the late 1960s favored intensification of the low salinity anomaly (reduction of water mass saltiness) in the Nordic Sea through two processes (i) reduction of inflow of salty Atlantic waters through the GS and intensification outflow of AW through the FS; (ii) intensification of inflow of fresh and cold Arctic Waters through the FS and reduction of the fresh water outflow to the Atlantic through the GSA. In this way the variations of the volume transport through the FS and GS created a disbalance in the heat and salt transport through the two straits which additionally strengthened the GSA in the model solution originally generated by the intensified advection of Arctic waters.

The model water exchange through the GS intensified in 1987 and remained higher than normal until 1997. In 1990 the magnitude of this intensification was between 6 and 8 Sv and in 1993 between 4 and 7Sv. The interannual variations of the model volume flux through the Fram Strait during this period were relatively low and had magnitudes below 1Sv. The Nordic Sea gained heat during this period through two processes (i) intensification of the inflow of salty AW and (ii) stronger than normal outflow of fresh and cold waters into the Atlantic Ocean.

After 1997 the volume flux through the two straits, FS and GS, is weaker than normal (Figure 2.6). At the same time during this period the properties of the source water of the inflow into the Nordic Seas through the GS changed, see Figure 2.3. This inflow consists of the AW and modified Atlantic Water (MAW) (Dickson et al,

1988). The AW originates from the warm and salty waters of the North Atlantic Current (NAC). The MAW is formed through mixing of the waters of the sub-polar North Atlantic and the North Atlantic Current. It is fresher and colder than the AW. Here we calculated the AW transport through GS and FS by using the approach of Hansen, S. Osterhus, et al. (2008). The model long term mean transport of AW through the GS is 8.7 Sv (see Table 1). The interannual variations of AW inflow have magnitude of about 1Sv (Figure 2.7). On average it was below normal before 1985 and higher than normal after 1985. In the period after 1997 when the total volume inflow through the GS weakens (see Figure 2.6) the AW transport remains higher than normal (Figure 2.7). The AW transport through FS is larger than average in the 1960s and decays by about 4Sv between 1990 and 2000. The variations of the volume flux influenced the heat balance of the Nordic Seas.

The normalized rate of change of the heat content calculated as the sum of lateral and surface heat fluxes is shown on Figure 2.8 separately for the Nordic Seas and Sub-Polar North Atlantic. The variations of the volume transport through the straits affected the heat balance of the Nordic Seas in the two periods discussed in this work. The heat loss due to intensified inflow of cold Arctic waters and outflow of AW through the Fram Strait in the 1960 was in disbalance with the reduced heat gain due to the weaker than normal inflow of AW from the Atlantic Ocean during the same period. The intensified inflow of AW from Atlantic in the late 1980s and early 1990s was not balanced by equivalent heat loss through the Fram Strait. In the later period from 1998 to 2005 the volume transport through the two straits is lower than normal but the AW volume transport over the GS remains high. In this period the heat balance of the Nordic Seas is positive (Figure 2.8).

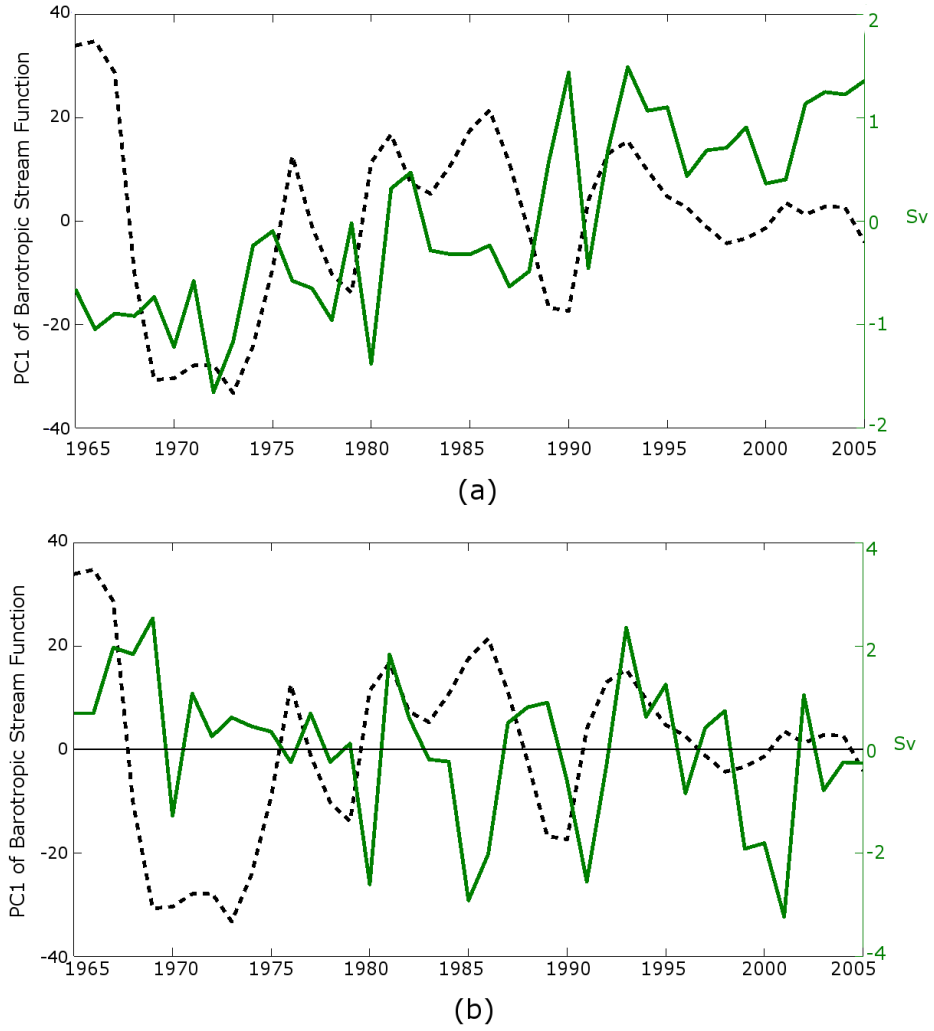

Figure 2.7: Annual average volume transport (Sv) of the Atlantic water crossing (a) over the Greenland Scotland Ridge and (b) through the Fram Strait. The Atlantic water mass is defined using the definitions in Hansen, S. Osterhus, et al. (2008) and O. Skagseth et al. (2008). The dashed black line in both (a) and (b) indicates the principal component for the 1^{st} EOF of the barotropic stream function for the period 1965 to 2005 (calculated from model results).

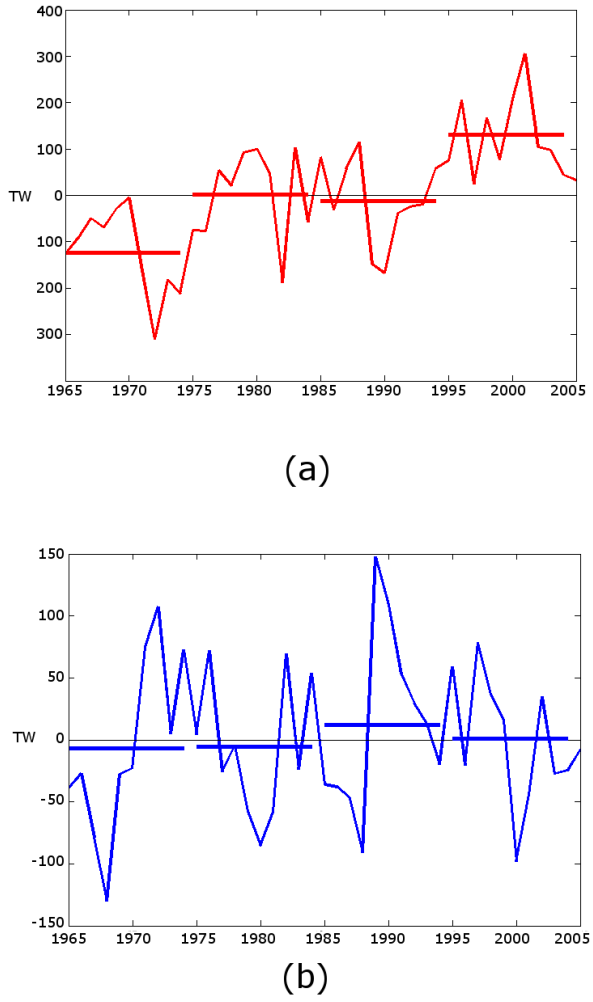

Figure 2.8: The normalized rate of change of the heat content calculated as sum of lateral and surface heat fluxes into (a) Sub-polar North Atlantic and (b) into the Nordic Seas for the period 1965-2005. Horizontal bars are 10 year averages.

The lateral heat and salt transport has an impact on the change of the water mass properties in the Nordic Seas. These changes interact in a complex way with the intensity of the general circulation and boundary currents in the Nordic Seas. The black curve on the Figure 2.6 shows the principle component of the dominant EOF of the barotropic stream function. The strongest intensification of simulated circulation occurred in the late 1960s. The intensified advection of fresh and cold water anomalies in the surface $200 - 300\ m$ layer in the 1960s and early 1970s strengthened stratification. Surface ice formation and strong stratification limited intense vertical mixing typical of the region through the 1960s and early 1970s. This large scale anomaly intensified the horizontal density gradients and the circulation in the 1960s. Intensified circulation, reduced inflow from the Atlantic Ocean and horizontal mixing were factors that favored spreading of the fresh water anomaly in the Nordic Seas in the late 1960s. This caused a weakening of horizontal density gradients and a sharp decline in the intensity of simulated cyclonic circulation in the late 1960s.

Figure 2.9 shows the dominant mode of variability of the surface wind stress curl. It defines the variations of the intensity of a cyclonic pattern in the central part of the basin (Figure 2.9a). When this mode is in it's positive phase, the atmospheric circulation favors intensification of cold Arctic air transport over the Nordic Seas, strong surface cooling and deep convection. The cyclonic boundary current in the Nordic Seas intensifies between 1973 and 1987 (Figure 2.5). This change correlates well with the increase of the strength of the surface forcing during the same period of time (Figure 2.9). The intensified circulation in the Nordic Seas and reduced transport through the GS and FS (Figure 2.6) along with the weak surface forcing (Figure 2.9) between 1987 and 1989 favored reduction in the horizontal density gradients and

caused a sharp decline in the cyclonic circulation between 1985 and 1989 (Figure 2.5). The annual mean SSH data used in this figure are obtained over a period of 12 years. The calculation of the correlation coefficient from a timeseries with 12 elements can not be done with an acceptable statistical significance. Therefore, the discussion focuses on the comparison of the long-term trends in the two curves. In the last 10 years of simulation the surface forcing and lateral transport over the GS and through FS are weaker than normal and hence there is not much variability in the intensity of circulation during this period.

2.7 Conclusion

The article presents results from a model study of the mechanism of the variability of the Nordic Seas in the past 50 years. We study the processes that had impact on the GSA in the late 1960s and early 1970s and warming of the sub-arctic and arctic in the 1990s. Previous studies (R. Dickson et al., 1988; Marsh et al., 2008; Polyakov, Beszczynska, et al., 2005; Karcher et al., 2003; Zhang, Rothrock & Steele, 1998) demonstrated that advection played an important role in these two events for propagation of anomalies of water characteristics between the Arctic and sub-polar North Atlantic. The atmospheric forcing related to changes of the NAO is considered another factor which had a major impact on the dynamics of this region (R.R. Dickson, J. Osborn, et al., 2000) during the GSA and in the 1990s.

In this article we study interannual variability of the volume and heat transport through the Nordic Seas in the last 50 years and the impact which it had on water mass properties. Previous studies demonstrated that transport through the straits show a

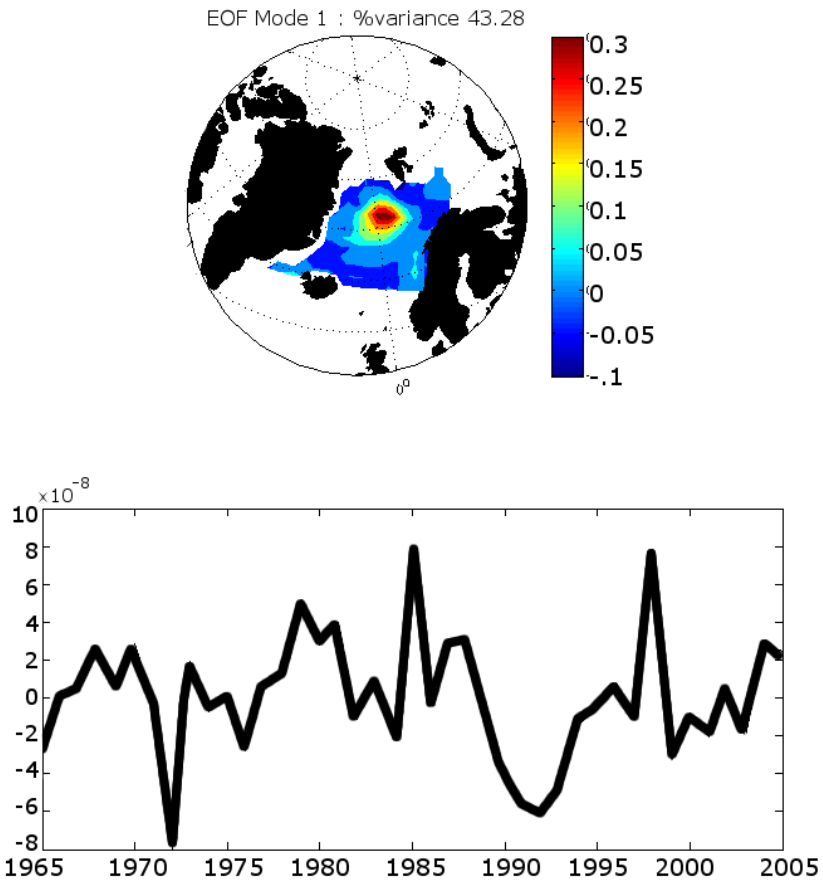

Figure 2.9: (a) 1^{st} EOF of the wind stress curl over the Nordic Seas and (b) its principal component.

good correlation with NAO atmospheric forcing (see Zhang, Steele, et al., 2004). At the same time our results suggest the exchange through the Fram Strait and over the Greenland-Scotland Ridge can also differ significantly in time. In the past fifty years, there were two periods of time when this difference had large amplitude - the time period of the GSA and the late 1990s.

The model net volume flux through the Fram Strait is about 3 Sv, which is the difference of the rate of inflow of Arctic Waters and outflow of Atlantic Waters. The interannual variability is related to change in both inflow and outflow while the net flux does not change significantly. The intensification of transport through the Fram Strait is related to loss of heat and salt by the Nordic Seas through both increase of the fresh and cold water inflow and intensified AW outflow. Similarly, the intensified exchange over the Greenland-Scotland Ridge is related to increased salt and heat flux into the Nordic Sea. When anomalies of the inflow and outflow through the two straits have opposite signs, they have the same effect on the heat and salt balance of the Nordic Seas, either contributing to the cooling/freshening or to the warming of the region. In the 1960s they both contributed to the freshening and cooling of the Nordic Seas, in the 1980s they initiated the warming of the basin. In both periods, the cyclonic circulation intensified, seen in the principal component of the barotropic streamfunction, as a response to the changes in the water mass transport through the straits.

The potential of the Nordic Seas to amplify the interannual variability in the subarctic through the disbalance of lateral heat and salinity fluxes through the straits that connect it with the North Atlantic and Arctic Oceans is an important feature that should not be ignored when studying the effects of climate change on this region.

In conclusion, our model results suggest that there are common elements in the dynamics of the Nordic Seas during the warming of the Arctic and subarctic in the 1990s and during the GSA: (1) During both periods the heat and salt exchange through the Greenland - Scotland Ridge and Fram Strait had opposite signs and large magnitudes. (2) In the 1960s they favored the intensification the large scale fresh and cold anomaly in the surface layer caused by the GSA. In the 1980s and 1990s it produced anomalous warm AW entering Arctic. (3) The variations of the thermohaline properties that were created by the variations in the lateral exchange through the straits were associated with intensified the barotropic circulation during the two periods.

Acknowledgment This work was funded by Canadian Foundation for Climate and Atmospheric Science through the GOAPP and GR-631. We also wish to thank Jieshun Zhu for his help with the model set up.

References

Aksenov, Y. et al. (2010). "The North Atlantic inflow to the Arctic Ocean: High-resolution model study". In: *Journal of Marine Systems* 79(1-2), pp. 1–22.

Antonov, J. et al. (2005). "World Ocean Atlas 2005, Volume 2:Salinity". In: *NOAA Atlas NESDIS 62*. Ed. by S. Levitus. U.S. Government Printing Office, Washington, D.C., 182p.

AVISO (2011). *AVISO (Archiving and Validation and Interpretation of Satellite Oceanographic data)*. Tech. rep. The altimeter products were produced by Ssalto/Duacs and distributed by Aviso, with support from Cnes.

Beckmann, A & R Döscher (1997). "A method for improved representation of dense water spreading over topography in geopotential-coordinate models". In: *Journal of Physical Oceanography* 27(4), pp. 581–591.

Belkin, I. et al. (1998). "Great Salinity Anomalies". In: *Progress in Oceanography* 41, pp. 1–68.

Blanke, B. & P. Delecluse (1993). "Variability of the tropical Atlantic ocean simulated by a general circulation model with two different mixed layer physics." In: *J. Phys. Oceanogr.* 23, pp. 1363–1388.

Dickson, B., J. Meincke & P. Rhines (2008). "Arctic-Subarctic ocean fluxes: Defining the role of the Northern Seas in climate. A general introduction". In: *Arctic-*

Subarctic Ocean Fluxes - Defining the role of the northern seas in climate. Ed. by R.R. Dickson, J. Meincke & P. Rhines. Springer, pp. 1–14.

Dickson, R.R., J.J. Osborn, et al. (2000). "The Arctic response to the North Atlantic Oscillation". In: *J. Clim.* 15, pp. 2671–2696.

Dickson, R. et al. (1988). "The Great Salinity Anomaly in the northern North Atlantic". In: *Progress in Oceanography* 20(2), pp. 103–151.

Drange, H. et al. (2005). "The Nordic seas: an overview". In: *GEOPHYSICAL MONOGRAPH-AMERICAN GEOPHYSICAL UNION* 158, p. 1.

Fichefet, T. & M.A. Maqueda (1999). "Modelling the influence of snow accumulation and snow-ice formation on the seasonal cycle of the Antarctic sea-ice cover". In: *Climate Dynamics* 15(4), pp. 251–268.

Gent, P.R. & J.C. McWilliams (1990). "Isopycnal mixing in ocean circulation models". In: *J. Phys. Oceanogr* 20, pp. 150–155.

Häkkinen, S. & C. Geiger (2000). "Simulated low-frequency modes of circulation in the Arctic Ocean". In: *Journal of Geophysical Research: Oceans* 105(C3), pp. 6549–6564.

Hakkinen, S. & P.B. Rhines (2004). "Decline of subpolar North Atlantic circulation during the 1990s". In: *Science* 304(5670), pp. 555–559.

Hansen, B., S. Osterhus, et al. (2008). "The Inflow of Atlantic Water, Heat and Salt to the Nordic Seas". In: *Arctic-Subarctic Ocean Fluxes - Defining the role of the northern seas in climate*. Ed. by R.R. Dickson, J. Meincke & P. Rhines. Springer, pp. 15–43.

Haugan, P.M. et al. (1991). "Modeled and observed mesoscale circulation and wave current refraction during the 1988 Norwegian continental shelf experiment". In: *Geophysical Research* 96, pp. 10487–10506.

Hibler III, W.D. (July 1979). "A Dynamic Thermodynamic Sea Ice Model". In: *Journal of Physical Oceanography* 9, pp. 815–846.

Hilmer, M. & T. Jung (2000). "Evidence for a recent change in the link between the North Atlantic Oscillation and Arctic sea ice export". In: *Geophysical Research Letters* 27(7), pp. 989–992.

Isachsen, P.E., J.H LaCasce, et al. (2003). "Wind-Driven Variability of the Large-Scale Recirculating Flow in the Nordic Seas and Arctic Ocean". In: *Phys. Oceanography* 33, pp. 2535–2550.

Jackett, DR & TJ McDougall (1995). "Stabilization of hydrographic data". In: *J. Atmos. Oceanic Technol* 12, pp. 381–389.

Karcher, M. et al. (2003). "Arctic warming: Evolution and spreading of the 1990s warm event in the Nordic seas and the Arctic Ocean". In: *Journal of Geophysical Research: Oceans* 108(C2).

Khatiwala, S., P. Schlosser & M. Visbeck (Feb. 2002). "Rates and Mechanisms of Water Mass Transformation in the Labrador Sea as Inferred from Tracer Observations". In: *Journal of Physical Oceanography* 32, pp. 666–686.

Lohmann, K., H. Drange & M. Bentsen (2008). "Response of the North Atlantic subpolar gyre to persistent North Atlantic oscillation like forcing." In: *Clim Dyn* 32, pp. 273–285.

Madec, G. (2008). *NEMO ocean engine: version 3.1.* Laboratoire d'Oceanographie et du Climat: Experimentation et Approches Numeriques.

Marsh, R. et al. (2008). "Mechanisms for recent warming of the North Atlantic: Insights gained with an eddy-permitting model". In: *Journal of Geophysical Research,* 113. doi:10.1029/2007JC004096.

Merryfield, W.J., G. Holloway & A. E. Gargett (June 1999). "A Global Ocean Model with Double-Diffusive Mixing". In: *Journal of Physical Oceanography* 29, pp. 1124–1142.

Muench, R.D. et al. (1992). "Winter oceanographic conditions in the Fram Strait Yermak Plateau region". In: *Journal of Geophysical Research* 97, pp. 3469–3483.

Mysak, L., D. Manak & R. Marsden (1990). "Sea-ice anomalies observed in the Greenland and Labrador Seas during 1901-1984 and their relation to an interdecadal Arctic climate cycle". In: *Climate Dynamics* 5(2), pp. 111–133.

Mysak, L. & S. Power (1992). "Sea-ice anomalies in the western Arctic and Greenland-Iceland Sea and their relation to an interdecadal climate cycle." In: *Climatological Bulletin* 26(3), pp. 147–176.

NEMO (Nucleus for European Modelling of the Ocean) (Nov. 2011). *Meshmask grid.* http://www.nemo-ocean.eu/About-NEMO/Gallery/Meshmask-grid.

Orvik, K. & P. Niiler (2002). "Major pathways of Atlantic waters in the North Atlantic and Nordic Seas towards Arctic." In: *Geophys. Res. Lett.* 29(19), doi:10, 1029/2002GL01502.

Østerhus, S. & T. Gammelsrød (1999). "The abyss of the Nordic Seas is warming". In: *Journal of Climate* 12(11), pp. 3297–3304.

Polyakov, I., G. Alekseev, et al. (2004). "Variability of the Intermediate Atlantic Water of the Arctic Ocean over the Last 100 years." In: *Journal of Climate* 17(23). doi:10.1175/JCLI-3224.1, pp. 4485–4497.

Polyakov, I., A. Beszczynska, et al. (2005). "One more step toward a warmer Arctic". In: *G. Res. Lett.* 32(L17605). doi:10.1029/2005GL023740.

Quadfasel, D. et al. (1991). "Warming in the Arctic". In: *Nature*.

Rhines, P., S. Häkkinen & S. Josey (2008). "Is Oceanic Heat Transport Significant in the Climate System". In: *Arctic-Subarctic Ocean Fluxes - Defining the role of the northern seas in climate*. Ed. by R.R. Dickson, J. Meincke & P. Rhines. Springer, pp. 87–110.

Rossby, T., M.D. Prater & H. Søiland (2009). "Pathways of inflow and dispersion of warm waters in the Nordic seas." In: *Geo. Phys. Res.* 114. doi:10.1029/2008JC005073.

Schauer, U. et al. (2008). "Variation of Measured Heat Flow Through the Fram Strait Between 1997 and 2006." In: *Arctic-Subarctic Ocean Fluxes - Defining the role of the northern seas in climate*. Ed. by R. R. Dickson, J. Meincke & P. Rhines. Springer, pp. 65–85.

Schlichtholz, P. (2011). "Influence of oceanic heat variability on sea ice anomalies in the Nordic Seas". In: *Geophys. Res. Lett.* 38, doi:10.1029/2010GL045894.

Skagseth, O et al. (2008). "Arctic-Subarctic Ocean Fluxes - Defining the role of the northern seas in climate". In: Springer. Chap. Volume and Heat Transports to the Arctic Ocean.

Straneo, F. et al. (2009). "Did changes in the Subpolar North Atlantic trigger the recent mass loss from the Greenland Ice Sheet?" In: *US Clivar Variations Newsletter* 7, pp. 1–4.

T.Fichefet & M.A.Morales Maqueda (1997). "Sensitivity of a global sea ice model to the treatment of ice thermodynamics and dynamics." In: *J. Geophys. Res.* 102, pp. 12609–12646.

Tereshchenko, V. (1997). "Seasonal and year-to-year variation in temperature and salnity of the main currents in Kola section in the Barents SeaHistorical data on water temperature in the 0-200m layer in the Kola section in the Barents Sea (1". In: *PINRO*. PINRO Press, 71p.

Thompson, K.R. et al. (2006). "A simple method for reducing seasonal bias and drift in eddy resolving ocean models". In: *Ocean Model*, pp. 122–138.

Timmermann, R. et al. (2005). "On the representation of high latitude processes in the ORCA-LIM global coupled sea ice–ocean model". In: *Ocean Modelling* 8(1-2), pp. 175–201.

Voet, G. et al. (2010). "The mid-depth circulation of the Nordic seas derived from profiling float observations". In: *Tellus*(62A). doi:10.1111/j.1600-0870.2010.00444.x, pp. 516–529.

Yashayaev, I. (2007). "Hydrographic changes in the Labrador Sea, 1960-2005". In: *Prog. Oceanogr.* 73(3-4), pp. 242–276.

Zhang, J., D A. Rothrock & M. Steele (1998). "Warming of the Arctic Ocean by a strengthened Atlantic inflow: Model results". In: *Geophysical Research Letters* 25(10), pp. 1745–1748.

Zhang, J., M. Steele, et al. (2004). "Increasing exchanges at Greenland-Scotland Ridge and their links with the North Atlantic Oscillation and Arctic sea ice". In: *Geophysical research letters* 31(9).

Connecting Text

This article addresses objectives 3 and 4 described in Section 1.5.3 .

Chapter 2 demonstrates that advection of heat through the GSR had an essential impact on the long-term variability of the heat budget in the adjacent region. The study was based on a coarse resolution global ocean general circulation model. As such, it is limited in realistically representing important details of the water dynamics in the ocean region adjacent to the GSR and the impact of mesoscale processes on heat transport.

The complex bottom topography in the region is a challenge that limits the realism in present-day ocean model simulations in this region. Therefore, the study of ocean heat transport in the following article is based on ocean observations. Argo data, satellite along-track altimeter and SST observations are used to asses the mean and eddy-induced heat advection.

This article appears as Lundrigan and Demirov (2019) in *Journal of Geophysical Research: Oceans.*

Chapter 3

Mean and Eddy-Driven Heat Advection in the Ocean Region Adjacent to the Greenland-Scotland Ridge Derived from Satellite Altimetry

3.1 Abstract

Along-track altimeter and sea surface temperature (SST) satellite observations and ARGO in-situ measurements of temperature and salinity are used to investigate the heat transport by mean currents and eddies in the ocean region adjacent to the Greenland-Scotland Ridge (GSR) from 2003 to 2008. Our results show that heat

advection by the mean flow in the surface layer is zonally asymmetric with a higher magnitude in the western part of the region. This asymmetry is associated with an excessive mean heat advection in an area adjacent to the Denmark Strait. The advection of heat is high and positive south of the strait and low and negative north of it. We suggest that this heat advection impacts the local budgets of heat and potential energy of the mean flow in the surface layer.

Mesoscale eddies are identified and their characteristics, including radius, sea-level anomaly, lifetime, and paths of propagation, are assessed using along-track altimeter data. About 70% of the eddies are observed in the eastern part of the studied region. The eddy-induced heat transport by warm mesoscale eddies in the Norwegian Sea was found to be about two-and-a-half times larger than the mean advection by the Norwegian Atlantic Current. We suggest, therefore, that the eddy-induced transport is a dominant factor in the heat budget of this region.

3.2 Introduction

The ocean circulation and transport over the Greenland Scotland Ridge (GSR) are crucial for maintaining heat, freshwater, and sea-ice exchange between the Arctic Mediterranean and the Subpolar North Atlantic Ocean. The Arctic Mediterranean is the region north of the GSR, which comprises the Arctic and Nordic Seas. Like the Mediterranean Sea, the Arctic Mediterranean receives low-density Atlantic Water and transforms it into dense water (Meincke, Rudels & HJ Friedrich, 1997). The dense water overflow over the GSR contributes to the North Atlantic Deep Water mass formation, which feeds the lower limb of the Atlantic Meridional Overturning

Circulation (AMOC) (R.R. Dickson & Brown, 1994).

Warm and salty Atlantic Water enters the Arctic Mediterranean mainly in the eastern part of the GSR over the Iceland-Faroe Ridge and through the Faroe-Shetland Channel (see Figure 3.2). The return flow into the Atlantic Ocean includes cold and fresh surface Polar Water and dense-water overflow (Hansen & Østerhus, 2000). The different characteristics of the inflow and outflow through the GSR imply a net heat and salt flux into the Arctic Mediterranean of about 330 TW (1 TW=10^{12} W) and 303 $\times$ 10^6 kg/s (Serreze et al., 2006), respectively. The long-term variations in heat and salt transport through the GSR have significant implications for the variability of the Arctic Mediterranean (Yashayaev & Seidov, 2015). These variations are driven by changes (1) in the volume transport through the GSR (S. Lundrigan & E. Demirov, 2012) and (2) in the temperature and salinity of the Atlantic Water entering the Nordic Seas (Glessmer et al., 2014).

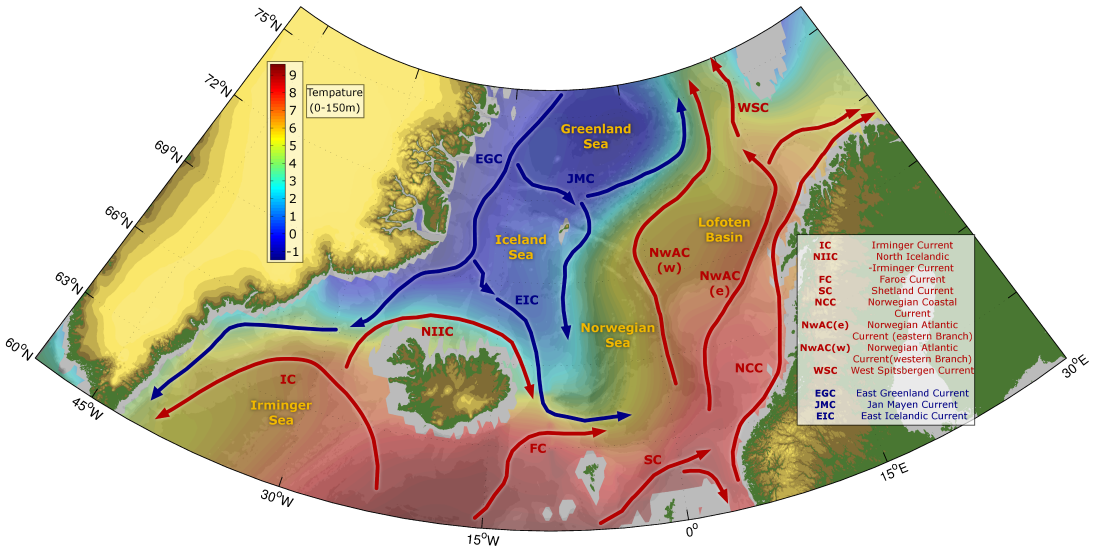

Figure 3.1: Sea Surface Temperature in the Northeast Subpolar North Atlantic Ocean and Nordic Seas, bottom topography, and major currents (after AMAP, 1998).

When the main surface water masses involved in heat and freshwater transport spread through the region adjacent to the GSR, they experience a gradual transformation (Brambilla, Talley & Robbins, 2008). South of the GSR, the warm and salty waters of the subtropical North Atlantic enter the region along the multiple branches of the North Atlantic Current (Figure 3.2). These waters are cooled and transformed in the subpolar gyre, where they are the origin of the surface Subpolar Mode Waters (SPMW) (McCartney & Talley, 1982). The SPMW are vertically nearly uniform and gradually change as they spread horizontally. Because of their uniform temperature and large volume, the SPMW are a source of heat for the atmosphere of the subpolar Atlantic Ocean (Hanawa & Talley, 2001). A remnant of the SPMW called the Irminger Water spreads (see Myers, Kulan & Ribergaard, 2007) at intermediate

depths and plays a significant role in the heat budget of the Irminger and Labrador Seas (Straneo, 2006; Zhu & Demirov, 2011).

North of the GSR, the surface Atlantic Water is intensively transformed and cooled as it is transported northward by the Norwegian Atlantic Current (NwAC) (Mauritzen, 1996a; Mauritzen, 1996b). The processes of air-sea exchange, advection by mean currents, and eddy-induced diffusion drive the transformation of surface water masses and determine their heat and freshwater budgets (Brambilla, Talley & Robbins, 2008). Mesoscale eddies in this region play an essential role in the transformation of the Atlantic Water and the exchange of heat and freshwater between the NwAC and the central part of the Norwegian Sea. Isachsen, Koszalka & JH LaCasce (2012) demonstrated that the horizontal eddy-induced heat transport in the NwAC is "of first-order importance to the total buoyancy budget of the region and, ultimately, to the exchanges across the Greenland–Scotland Ridge."

Here, we focus on the horizontal mean and eddy-induced heat advection and diffusion and their impact on the heat budget of the surface layer. We use satellite altimeter and SST observations to assess the contribution to the heat budget of the divergent part of the advective mean and eddy heat flux in the surface layer. The non-divergent (rotational) eddy-induced heat advection vanishes in the equations of the heat budget. During eddy decay, this transport indirectly affects the heat content of the surface layer through local enhancement of stirring, the formation of fine-scale filaments, and irreversible mixing. These processes are generally unresolved in the regular data from the global ocean observing system. In this study, we assess their contribution as the change in local heat content in the area of eddy decay.

The article is organized as follows. Section 3.3 describes the data and method of

the study. Section 3.4 discusses the characteristics of mean flow and eddies over the GSR, which determine the advection and eddy-induced diffusion of heat. Section 3.5 presents an analysis of the mean and eddy-induced fluxes of heat in the area adjacent to the GSR. The last section provides discussions and conclusions.

3.3 Data and Method of Analysis

In this study, we use satellite altimeter observations of mean sea level (MSL) and sea level anomaly (SLA), gridded SST weekly maps, and ARGO temperature and salinity profiles for the period from 2003 to 2008. Two satellite missions, Geodetic and Oceanographic SATellite Follow-On (GFO) and Envisat (EN), were active during this time and provided observations for six years with a relatively regular temporal and spatial resolution over the studied area.

The GFO traverses the earth with a 17-day repetitive orbit up to 72^oN with a precision of $\pm$ 3.5 cm. The altimeter noise level for this satellite is between 2.5 and 2.58 cm for a significant wave height (SWH) of 2 m (Conger et al., 2009; Tran et al., 2002). The EN traverses the earth with a 35-day repetitive orbit up to about 80^oN. The noise in the EN altimeter observations is $\pm$ 4.5 cm (AVISO, 2013).

The ocean mesoscale is defined as variability with spatial scales between 10 km and 500 km (Chelton, Schlax & Samelson, 2011). In this study, the along-track altimeter data (AVISO, 2011) are averaged over one-second time bins, which correspond to distances of about 6.6 km for GFO and 6.5 km for EN at the latitude of the GSR. The previous study of Stammer & Dieterich (1999) demonstrated that the error of estimates of geostrophic velocities based on this method is sensitive to the spatial track

separation. These authors demonstrated, in particular, that zonal track separation of $0.5 - 0.75$ degrees leads to the best results and reported a substaintial degradation of the method for a track separation beyond 1 degree. In this study we use data from two satellites which improves the spatial resolution of the data and estimates of geostrophic velocities. The results still should be carefully used especially in the high-energy regions (see Stammer & Dieterich, 1999).

Therefore, the GFO and EN along-track data resolve the lower end of the mesoscale spectrum. The data is de-spiked, and gaps in the data of up to 10 points are linearly interpolated, following the work of Lilly et al. (2003). Gaps larger than 10 points and track sections shorter than 7 km are ignored. A five-point Hanning window is applied to filter out the high-frequency noise in the sea level anomaly data. Then, the altimeter data are used (a) to calculate the surface mean ($\overline{u}$,$\overline{v}$) and eddy (u',v') components of the geostrophic velocity and mean and eddy components of heat flux divergence and (b) to detect eddies automatically and study mesoscale eddy characteristics.

3.3.1 Method of Calculation of Surface Geostrophic Velocity and Heat Flux Divergence

The current velocity $\mathbf{v}$ and temperature T can be written as sums of their mean and eddy components:

$$\mathbf{v} = \overline{\mathbf{v}} + \mathbf{v}', \tag{3.1}$$

$$T = \overline{T} + T' \tag{3.2}$$

Here, the eddy temperature T' and velocity $\mathbf{v}'$ are defined as the variations relative to all record mean $\overline{T}$ and $\overline{\mathbf{v}}$. The components of the mean geostrophic velocity are

computed using the mean sea surface height $\overline{\eta}$:

$$\overline{u}_{i,j} = \frac{-g}{fa}\frac{\overline{\eta}_{i,j+1}-\overline{\eta}_{i,j-1}}{2\Delta\phi} \tag{3.3}$$

$$\overline{v}_{i,j} = \frac{g}{fa\cos\phi}\frac{\overline{\eta}_{i+1,j}-\overline{\eta}_{i-1,j}}{2\Delta\lambda} \tag{3.4}$$

Here, a is the radius of Earth; (i, j) are the indexes of gridded mean sea level $\overline{\eta}(i, j)$ data points in longitude and latitude, respectively; and $\Delta\lambda$, $\Delta\phi$ is the spatial resolution of the observations. The mean horizontal advection of heat flux is:

$$\left(\overline{\mathbf{v}}\cdot\nabla T\right)_{i,j} = \frac{\overline{u}_{i,j}}{a\cos\phi}\frac{\overline{T}_{i+1,j}-\overline{T}_{i-1,j}}{2\Delta\lambda} + \frac{\overline{v}_{i,j}}{a}\frac{\overline{T}_{i,j+1}-\overline{T}_{i,j-1}}{2\Delta\phi} \tag{3.5}$$

where $\overline{\mathbf{v}} = (\overline{u}, \overline{v})$ is the vector of mean velocity and $\overline{T}$ is the mean surface temperature. The surface eddy velocity (u', v') and eddy-induced heat flux $(\overline{\mathbf{u}'\nabla T'})$ are computed based on the method of Stammer & Dieterich (1999), which uses altimeter observations from parallel satellite tracks to define the two orthogonal components of geostrophic velocity. Appendix B provides a detailed description of this method. The method was previously used in studies on eddy kinetic energy, surface circulation, and eddy-induced heat transport in the subpolar ocean (see Brath et al., 2010).

The SST data set used in this study is the Reynolds $1/4^o$ gridded observations from the High-Resolution SST (GHRSST) Level 4 AVHRR OI daily SST product from 2003 to 2008 (available from http://ghrsst.jpl.nasa.gov). The data set includes measurements from Advanced Very High-Resolution Radiometers (AVHRR) NOAA series satellites, calibrated by and blended with *in-situ* observations (Reynolds et al., 2007). In the heat flux calculations, the temperature is interpolated on the regular mean altimeter grid points in Equation (3.5) and along-track points in Equation (B.2).

3.3.2 Eddy Detection

The method of automatic detection of mesoscale eddies (see Lilly et al., 2003) uses wavelet analysis of along-track altimeter observations (see Appendix C). It was previously applied in studies of the Labrador Sea (Lilly et al., 2003) and the Bay of Biscay (Dussurget et al., 2011). In this method, the eddies are defined as long-living isolated potential vorticity anomalies associated with distinct patterns in the SLA. The eddy sea-level anomaly (Lilly, 2002; Lilly et al., 2003) has an azimuthally symmetric spatial structure with a surface displacement δ_0 and a radius R_0. δ_0 is positive for anticyclonic and negative for cyclonic eddies. The radius R_0 is defined as the distance between the eddy's center and the position of the maximum azimuthal speed.

Satellite tracks would not necessarily pass over the centers of the eddies that were observed. Therefore, the estimates of the "apparent" radius (R_*) and "apparent" surface displacement (δ_*) found in the wavelet analysis (see Appendix C) have magnitudes equal to or smaller than R_0 and δ_0, respectively. The Rossby number (ζ_*) of each eddy based on apparent eddy characteristics is

$$\zeta_* = 2b\frac{g\delta_*}{R_*^2 f^2} \tag{3.6}$$

where b is a constant that depends on eddy type (Lilly et al., 2003).

Based on this analysis, we identified 5103 eddies in the period from 2003 to 2008. Of these, 3077 are anticyclonic, and 2026 are cyclonic. Figure 3.2a shows the event census histogram for all the eddies observed in the studied area. Most eddies have spatial scales between 15 and 40 km, with maximum apparent sea level anomalies δ_* of up to 30 cm. The noise in the altimeter observations is an inherent problem that can potentially impact the analysis based on the along-track data sets, especially

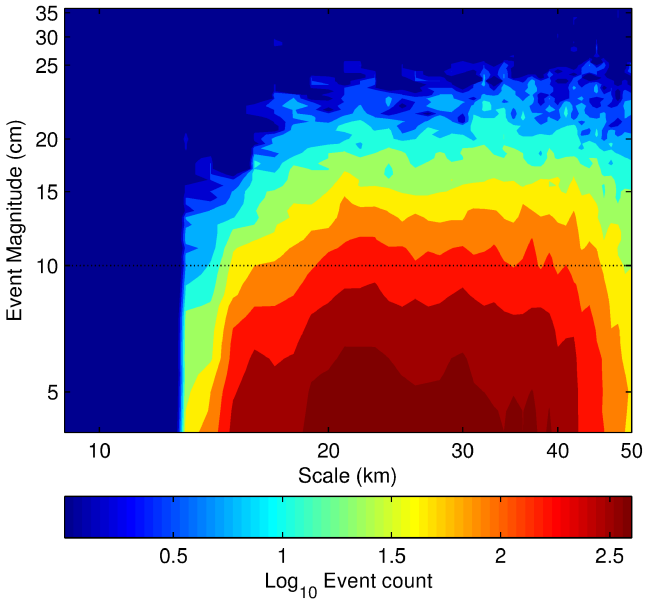

(a)

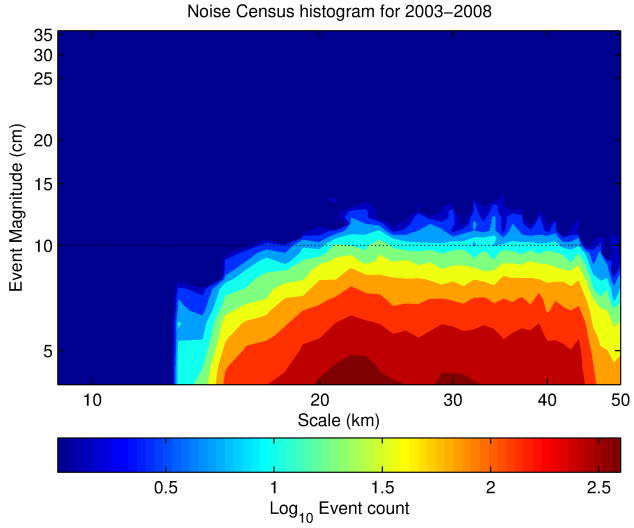

(b)

Figure 3.2: Histogram of all eddy events within the study area as a function of scale and sea-level height anomalies for (a) along-track altimeter observations and (b) synthetic noise data. See the main text for more details

for small sea level elevations. To determine the effect of noise on the event census histogram, we use a synthetic data set with characteristics identical to that of the observational error. The observational error is simulated as a Gaussian white noise time series with a standard deviation of 2.58 *cm* and the same spatial structure as in the GFO altimeter data. The synthetic data are then filtered in the same way as the observations, and the wavelet analysis is applied. The scale magnitude histogram of the noise data set is shown in Figure 3.2b. "Events" in the synthetic data occur predominantly at small scales and amplitudes. The number of these events vanishes for sea level amplitudes larger than 6-7 cm. Based on these results, a cut-off value of 10 cm is used. All events with magnitudes smaller than 10 cm are discarded in our analysis. The same cut-off value was applied in a previous study on along-track altimeter observations in the Labrador Sea by Lilly et al. (2003).

The ARGO floats data from the National Oceanographic Data Center (NOAA & NODC, 2007) are used to study the vertical structure of mesoscale eddies. The ARGO archive is searched for profiles with positions that fall within mesoscale events identified from the SLA data. They are used to estimate eddy-induced anomalies in heat and salt content and heat flux. The standard instrumental error of temperature sensors of the ARGO floats is $\pm 0.002^{o}$C for temperature, ± 2.4 dbar for pressure, and ± 0.01 PSU for salinity. The measurement accuracy of eddy-driven heat and salt anomalies, however, is affected by additional uncertainties in the estimates of the center positions and radii of eddies.

3.4 Characteristics of Mean Flow and Mesoscale Eddies over the Greenland-Scotland Ridge

The study area extends meridionally from 59^{o}N in the south to 72^{o}N in the north (see Figure 3.2). Zonally, it is limited by the coast of Norway to the east and East Greenland to the west. To account for the large spatial variations in water mass characteristics and dynamics in this region, the analysis of the mean flow, mesoscale eddies, and heat advection is done separately for the four subregions shown in Figure 3.3a. The 65^{o}N parallel divides the northern and southern parts of the region. In the zonal direction, the subregions are separated by the 10^{o}W meridian.

3.4.1 Surface Mean Circulation

Figure 3.3b shows the surface mean geostrophic currents and SST averaged over the period from 2003 to 2008. The inflow of subtropical Atlantic waters influences the surface water mass and flow characteristics in Subregions 3 and 4 in Figure 3.3a. The waters enter the southeastern part of the studied area (see Figure 3.3b) along multiple branches of the North Atlantic Current, often collectively referred to as the North Atlantic Drift Current (NADC). The NADC is a relatively slow, wind-driven, and widespread current system (Veron et al., 1999). A part of the NADC passes over the Iceland-Faroe Ridge and the Faroe-Shetland Channel and continues as the NwAC in the Nordic Seas. The NwAC (see Figure 3.3b) consists of two branches, which are relatively narrow and have persistent currents. The two branches are topographically constrained along quasi-permanent paths. The eastern NwAC branch, also called

the Norwegian Atlantic Slope Current, is a barotropic current along the continental slope off the coast of Norway. The western branch of the NwAC is the Norwegian Atlantic Front Current. It is a baroclinic, topographically steered jet linked to the Arctic Front (K. Mork & Ø. Skagseth, 2010).

In the western part of the studied region, the East Greenland Current (EGC) transports cold and fresh waters (see Figure 3.3b) and sea ice of Arctic origin along the coast of Greenland (B. Rudels, H. Friedrich & Quadfasel, 1999; B. Rudels, Fahrbach, et al., 2002). At the Jan Mayen Fracture Zone, the flow in the EGC that is deeper than 1800 m is diverted eastward. In the upper layer, the EGC branches, with the main branch flowing along the coast of Greenland. The second, smaller branch extends eastward as the Jan Mayen current (see Figure 3.3b). Further south, another branch separates from the EGC (see Figure 3.3b) and forms the East Icelandic Current (Blindheim & Osterhus, 2005). This current brings cold and fresh waters from the EGC along the northern and eastern coasts of Iceland.

South of the Denmark Strait, the EGC flows over the shelf along the coast of Greenland parallel to the Irminger Current (IC). The IC originates as a branch of the North Atlantic Current in the southern part of the Irminger Sea at about 30^{o}W and travels northward along the Reykjanes Ridge (Bersch, 1995). In the northern part of the Irminger Sea, the IC separates into two branches. A major part of the IC turns westward toward the Greenland coast and flows over the continental slope parallel to the EGC (see Figure 3.3b). The parts of the IC and the EGC that flow southward along the East Greenland/Irminger hydrographic front are collectively referred to as the East Greenland Irminger Current (EGIC) (Pickart, Torres & Fratantoni, 2005). The second branch of the IC in the northern part of the Irminger Sea extends over the

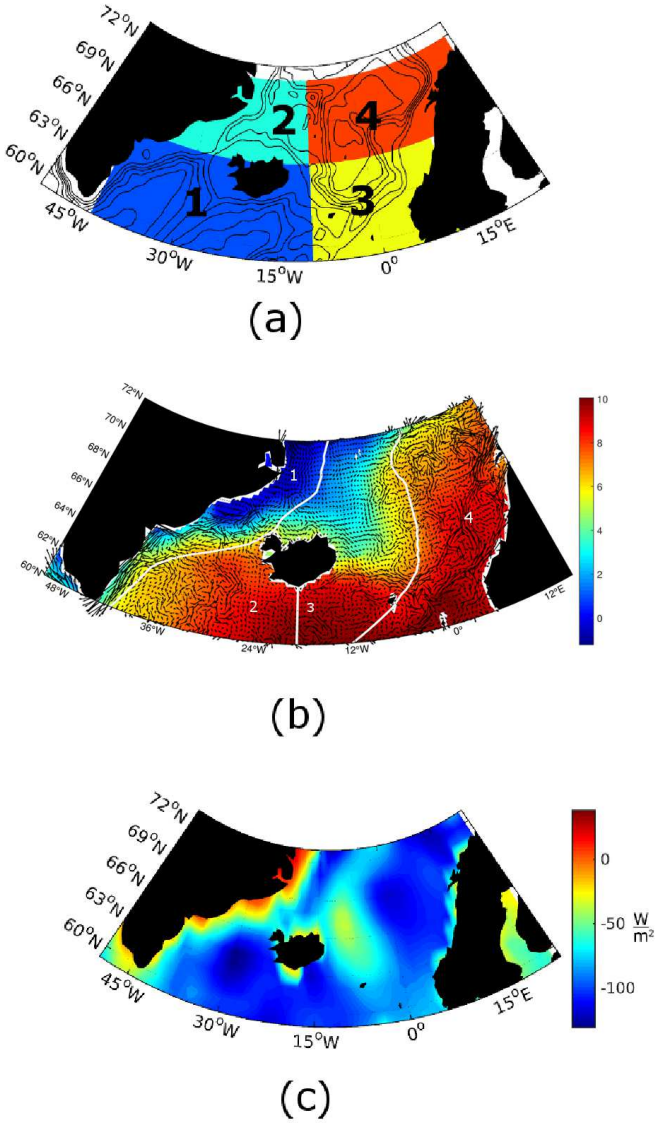

Figure 3.3: (a) Four subregions of the ocean region adjacent to the GSR used in the data analysis. (b) Mean surface temperature and geostrophic velocities between 2003 and 2008. The white solid lines show the boundaries of the areas used in the advective heat flux calculations in Section 3.5.2. (c) Annual mean air-sea turbulent heat flux between 2003 and 2008.

western and northern shelves of Iceland. This current is the North Icelandic Irminger Current, which brings salty and warm surface SPMW along the Iceland coast.

Figure 3.3c shows the annual mean surface turbulent heat flux Q_{st}, calculated as the sum of sensible and latent heat flux from NCEP. It is predominantly negative over the studied area. Its magnitude is relatively small over the coastal areas. The sea ice partly covers these areas during the coldest months of the year and prevents surface ocean waters from interacting with cold subarctic air. The turbulent heat exchange, shown in Figure 3.3c, is generally intense in the areas where the Atlantic Water and the SPMW spread and transform into the Norwegian Sea and the Irminger Sea, respectively. The presence there of relatively warm surface waters intensifies the temperature contrast between ocean and cold subpolar air and strengthens the heat exchange between ocean and atmosphere. The ocean dynamics over the GSR additionally contribute to the intensity of the heat exchange between sea and near-surface air. In winter, the vertical advection in the central part of the subpolar gyre brings relatively warm subsurface waters up. It intensifies the surface air-sea temperature contrast and heat exchange in the Irminger Sea (see Figure 3.3c). The mesoscale dynamics and eddy-driven transport also affect the air-sea exchange. Isachsen, Koszalka & JH LaCasce (2012) suggested that the transport of the warm surface Atlantic Water by the mesoscale eddies toward the central part of the Norwegian Sea intensifies the surface air-sea exchange there (see Figure 3.3c). Therefore, the horizontal heat flux due to mean circulation and eddies is an essential element of the heat budget in the surface layer of the region adjacent to the GSR.

3.4.2 Characteristics of Mesoscale Eddies

Figure 3.4 shows maps of the eddy kinetic energy and the number of mesoscale eddies observed during the studied period. The eddy kinetic energy (Figure 3.4a) is calculated by using the surface geostrophic velocity anomalies in Equation (B.1):

$$EKE = \frac{1}{2}(\overline{u'^2} + \overline{v'^2}) \tag{3.7}$$

In general, high values of EKE are observed in the areas where the surface waters originating from the subtropical Atlantic (Figure 3.4a) spread. The processes that contribute to the EKE include baroclinic instability, meandering of the main currents, mesoscale filaments as well as eddies (Chelton, Schlax & Samelson, 2011). The EKE has high values in the NwAC, NADC, and EGIC. The maximum value of 500 cm^2/s^2 in the NwAC corresponds well with the standard deviation of the velocity of about 30 cm/s observed in this region by Isachsen, Koszalka & JH LaCasce (2012). Values of EKE higher than 600 m^2/s^2 are found in the Reykjanes Rise, Rockwell Rise, Faroe and Shetland islands, and Denmark Strait (Greenland-Iceland Rise). All these regions have substantial slopes in their bottom topography. Previously, Hurlburt et al. (2008) demonstrated that the topographically constrained abyssal currents steer the mean paths of currents in the surface layer over regions with large bottom slopes. The coupling of the upper and deep layers triggers instability in surface ocean currents.

Figure 3.4b shows the number of eddies observed in each $1^o \times 1^o$ box normalized by the total number of along-track observations in that box. About 70% of all eddy events in this study are found in Subregions 3 and 4, and a major part of them are in the NwAC. Baroclinic instability is the essential mechanism driving the strong mesoscale variability of the Norwegian Sea (Ikeda et al., 1989). The local bottom topography

and time-varying winds play a role in triggering the instability of the NwAC (M. Mork, 1981). Studies based on ARGO float observations in the Norwegian Sea have shown that mesoscale eddies with a diameter of larger than 50 km and lifetimes of up to one to two weeks have a marked impact on the circulation and water transport in the region (Gascard & K. Mork, 2008).

Figure 3.5 shows histograms of eddy radius (Figure 3.5a) and sea-level anomaly (Figure 3.5b) for eddy events with $|\delta| \geq 10\ cm, |\zeta| \geq 0.1$. These cutoffs ensure the eddy events are clearly not noise ($|\delta| \geq 10\ cm$) and are dynamically meaningful ($|\zeta| \geq 0.1$). The values of these cutoffs are defined based on obervational data in the the subpolar ocean by Lilly et al. (2003). They define a statistically significant subset of events that can be identified as coherent eddies or "eddy band". The red curves in Figure 3.5 show the distributions for the anticyclonic eddies, and the blue curves the distributions for the cyclonic eddies. In total, the population of anticyclonic eddies exceeds the population of cyclonic eddies by 35% in the ocean region adjacent to the GSR.

The core radius histograms (in the "eddy band" $|\delta| \geq 10\ cm, |\zeta| \geq 0.1$) for all four subregions have maxima at about 23 km. The eddies with this core radius ($R_* = 23\ km$) are observed for seven data points in along-track altimeter observations and hence are resolved by our analysis. Previous estimates of the typical scale of eddies in the Subpolar North Atlantic Ocean showed very similar values. Lilly et al. (2003) showed that the dominant radius of eddies in the Labrador Sea is 22.7 km. Fan et al. (2013) observed anticyclonic eddies with a radius of about 20 km in the Irminger Sea.

The histograms in Figure 3.5a show some differences between the radius distribu-

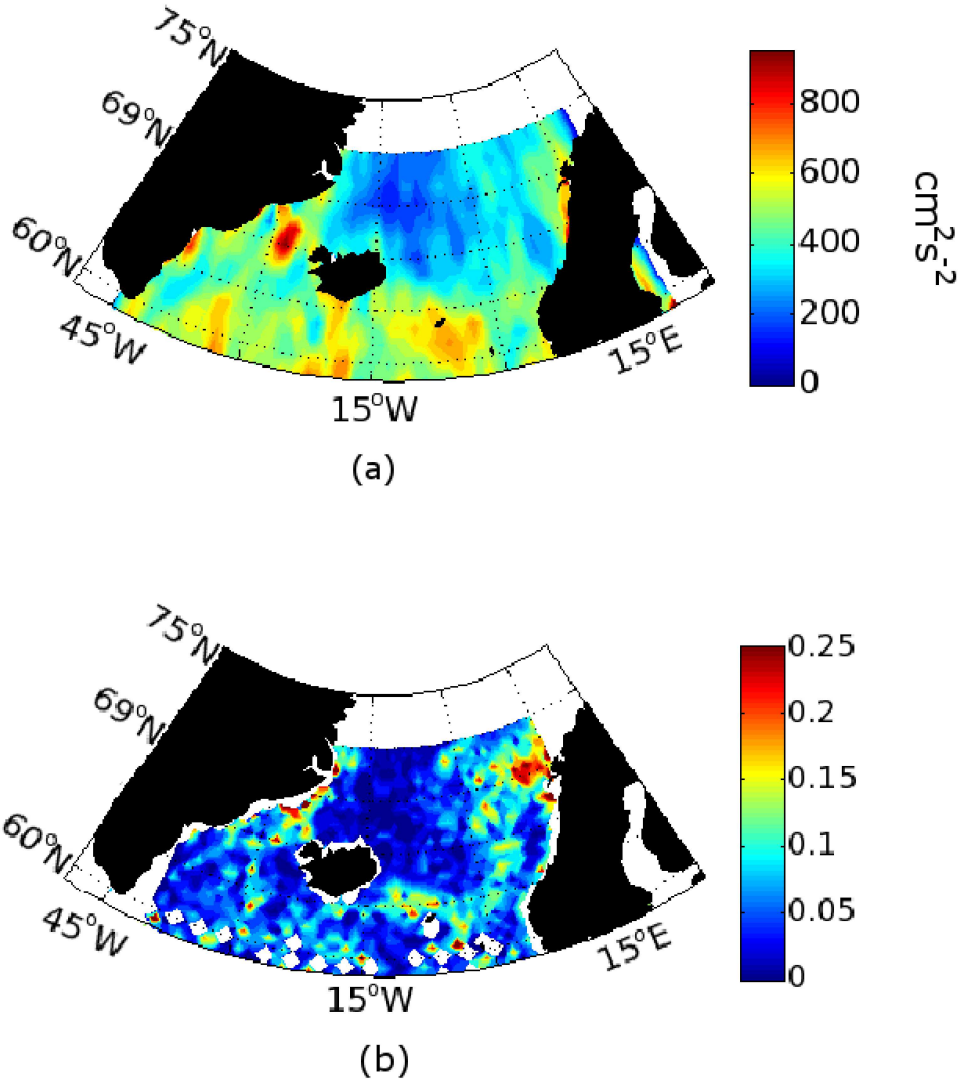

Figure 3.4: (a) Eddy kinetic energy of surface geostrophic flow, (b) Number of eddies observed in 1^ox1^o box normalized by the total number of satellite observations in that box.

tions for the four subregions, which reflect differences in eddy dynamics. The peak at 23 km is two to six times higher in Subregion 4 than in the other subregions (Figure 3.5a). This result is consistent with the observation that the overall num-

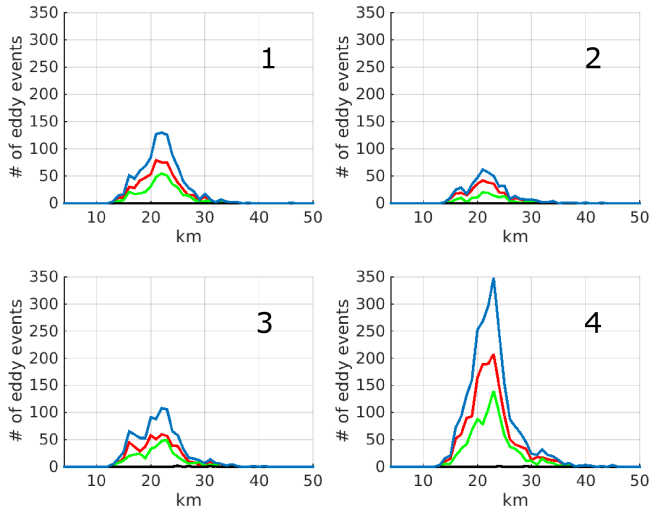

(a)

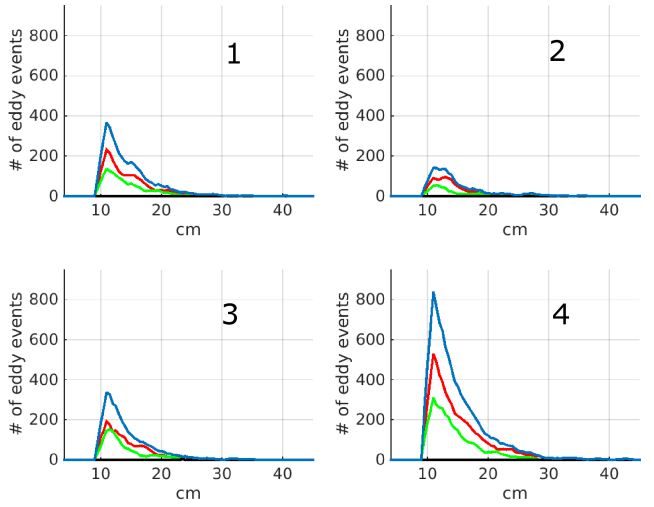

(b)

Figure 3.5: Histograms of eddy events ($\delta_* > 0.1\ m$, and $\zeta > 0.1$) versus (a) apparent radius R_* and (b) eddy sea level anomaly (δ_*). The curves are red for anticyclonic, green for cyclonic, and blue for all eddy events. The number of the subregions are indicated in the upper right part of the figures.

ber of eddies is significantly higher in Subregion 4 than in the rest of the studied area (Figure 3.4b). The radius distribution in Subregion 4 (Figure 3.5a) is skewed to the right, with a significant tail for eddy radii larger than 30 km (kurtosis$\approx$ 3.5, skewness$\approx$ 1.3). The histograms in the three other subregions (Subregions 1, 2, and 3) are more symmetric and have somewhat smaller tails at large eddy scales (kurtosis between 1.8 and 2.9, skewness between 0.5 and 0.98). The modes in the histograms of eddy amplitudes (Figure 3.5b) are about 12 cm. This value is close to the cut-off value of 10 cm for the anomalies in this study(see Section 3.3.2). Therefore, in all four subregions, the distributions of amplitudes have maxima at the smallest sea-level anomalies that can be resolved in this analysis. The distributions of eddy sea-level anomalies have a kurtosis between 3.4 and 5.1 and a skewness between 1.4 and 1.7.

The paths traveled by the eddies are found by an iterative search for eddy events in subsequent observation points. The Norwegian Sea is the most densely populated with long-living eddies. In this basin, 173 eddies were found to have paths longer than 500 km. Other areas densely populated with eddies are the Irminger Sea and the regions adjacent to the Denmark Strait and southeastern Iceland. The lifetimes and distances traveled by eddies are shorter in Subregion 2 than in the other areas. Only nine of the eddies found in this subregion have tracks longer than 500 km. Because of the significant zonal contrast in temperature in the studied area (see Figure 3.3b), the zonal propagation of eddies has a substantial impact on heat transport. Figure 3.6 shows for each subregion the fraction of eddy tracks that travel eastward. A general tendency is that many eddies propagate in the direction pointing toward the central part of the ocean subregions. In all subregions except Subregion 2, between 65-70% of the eddies that travel distances longer than 500 km propagate toward the central

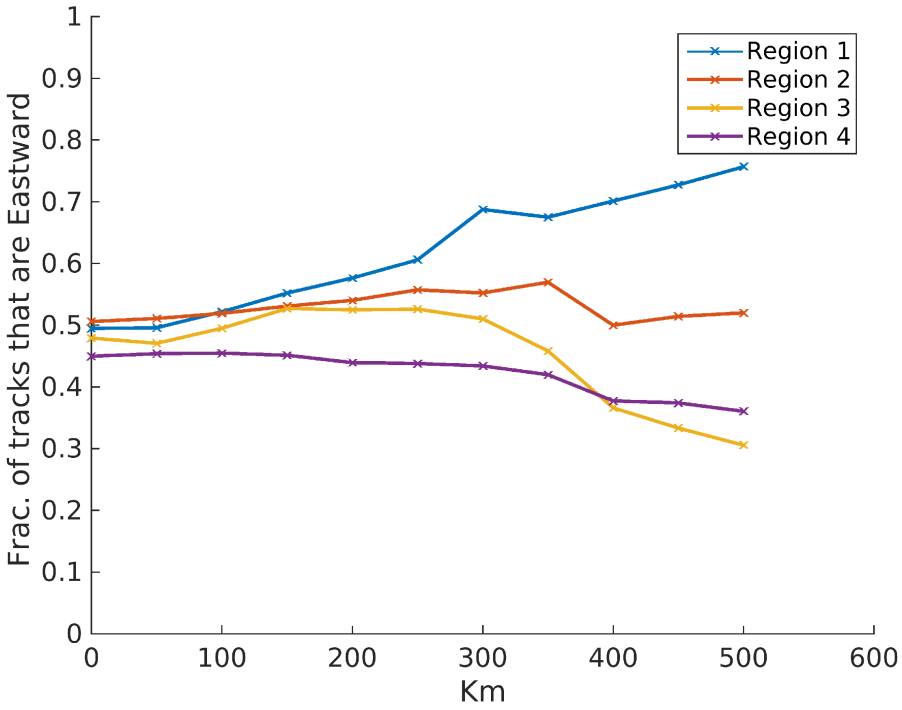

Figure 3.6: The fraction of eddy tracks moving eastward as a function of distance traveled.

parts of the subregions (see Figure 3.6). In Subregion 2, the number of eddies moving in both directions is approximately equal.

3.5 Mean and Eddy-Induced Transport of Heat

Mean currents and eddies of the GSR (Section 3.4) play an essential role in the meridional heat and freshwater transports by bringing warm and salty Atlantic Water poleward and cold and fresh waters of Arctic and Subarctic origin equatorward. In the ocean region adjacent to the GSR, these waters are intensively transformed due to surface air-sea exchange, advection, and mixing. The change in heat content in a

surface layer of depth h during this transformation is defined by

$$\frac{1}{\rho c_p}\frac{\Delta H}{\Delta t} = \frac{Q_s}{\rho c_p} - k_v \left.\frac{\partial \overline{T}}{\partial z}\right|_{-h} - \int_{-h}^{0} \left(\overline{\mathbf{u}\cdot\nabla T} + \overline{w\frac{\partial T}{\partial z}} + \nabla \cdot k_H \nabla \overline{T} \right) dz \qquad (3.8)$$

Here Q_s is the surface air-sea turbulent and radiative heat flux to a surface layer of thickness h, with the heat content H determined as

$$H = \int_{-h}^{0} \rho c_p \overline{T} dz,$$

where ρ and c_p are the density and heat capacity of seawater, respectively; $\mathbf{u} = (u, v)$ is the vector of horizontal velocity; ∇ is the horizontal divergence operator; and k_H and k_v are the horizontal and vertical turbulent diffusivities, respectively. The mean $\overline{()}$ is computed as a time average over the whole period of the study (2003 to 2008). Assuming that the vertical variations in u, v, T in the surface layer are small, we omit the vertical integration on the right-hand side of this equation. All the estimates of advective heat flux in this article refer to a layer of unit thickness $h = 1\ m$.

The horizontal heat transport in Equation (3.8) includes three components:

$$\overline{\mathbf{u}\cdot\nabla T} + \nabla \cdot k_H \nabla \overline{T} = \overline{\mathbf{u}}\cdot\nabla\overline{T} + \overline{\mathbf{u}'\cdot\nabla T'} + \nabla \cdot k_H \nabla \overline{T} \equiv \qquad (3.9)$$

$\equiv$ Advection by mean flow + Advection by mesoscale eddies + Small-scale turbulence.

The first term on the right-hand side of Equation (3.9) is the large-scale advection by the mean flow; the second term represents the contribution of the mesoscale eddies with scales of tens of kilometers; the last term is associated with irreversible eddy-induced fine-scale mixing at scales from centimeters to kilometers. The heat advection by mean flow ($\overline{\mathbf{u}}\cdot\nabla\overline{T}$) is a dot product of mean velocity and mean temperature gradient. The heat advection is significant in areas where the current velocity points along

the temperature gradient, i.e., where velocity has a significant component across the isotherms. The vector of eddy-driven heat flux is the correlation between velocity and gradient of eddy-induced temperature anomalies $\overline{\mathbf{u}' \cdot T'}$. This vector can be written as a sum (see J. Marshall & Shutts, 1981) of its rotational $\overline{(\mathbf{u}' \cdot T')}_R$ and divergent $\overline{(\mathbf{u}' \cdot T')}_D$ components. The contribution of the rotational component that is related to the growth and decay of mesoscale eddies (J. Marshall & Shutts, 1981) vanishes in the equation for the temperature (see Equation (3.8)). This component influences the ocean heat budget indirectly through irreversible fine-scale mixing during eddy decay (Eden, 2010). The heat flux due to fine-scale mixing appears in the last term on the right-hand side of Equation (3.9). The eddy-diffusion k_H in this term is a sum of three components (Abernathey & Marshall, 2013):

$$k_H = k + k_K + k_{OC}$$

Here k is diffusivity of temperature, and k_K includes the contribution from the rotational component of eddy-driven heat flux. The associated heat flux can be positive or negative locally but vanishes in the equation of globally integrated heat budget. The eddy-induced diffusion contributes to heat transport through the local enhancement of irreversible mixing created by eddy stirring and fine-scale patterns. This mixing is represented by k_{OC}, which is the Osborn-Cox diffusivity (T. Osborn & Cox, 1972).

3.5.1 Integral Heat Transport in the Four Subregions.

In Equation (3.8), the horizontal mean and eddy-induced heat advection in the surface layer are estimated based on the method described in Section 3.3 and Appendix B. Our preliminary analysis (not shown here) demonstrated that the observational

	Subregion 1	Subregion 2	Subregion 3	Subregion 4
Eddy Heat Advection (EHA)	2.3 ± 0.1	-5.5 ± 0.2	-0.4 ± 0.1	1.1 ± 0.1
Mean Heat Advection (MHA)	8.2 ± 0.2	-6.8 ± 0.2	-2.6 ± 0.1	4.7 ± 0.1
Total Heat Advection (THA)	10.5 ± 0.3	-12.3 ± 0.4	-2.9 ± 0.2	5.8 ± 0.2

Table 3.1: Eddy (EHA), mean (MHA), and total (THA) heat advection in the surface layer integrated over the four subregions. The units are $10^4\ m^2\ ^oC/s$.

estimate of the spatial distribution of eddy-driven heat advection (EHA) is noisy and notoriously difficult to analyze. The interpretation of this spatial distribution is further complicated by its non-Gaussian statistics (Chinn & Gille, 2007). Following the approach of Isachsen, Koszalka & JH LaCasce (2012), we determine area integrals of mean and eddy-driven advection by

$$MHA = -\int_A \overline{\mathbf{u}} \cdot \nabla \overline{T} dA \tag{3.10}$$

$$EHA = -\int_A \overline{\mathbf{u}' \cdot \nabla T'} dA \tag{3.11}$$

The integrals MHA and EHA and their sum $THA = MHA + EHA$ over the four subregions in Figure 3.3a are presented in Table 3.1. The total heat advection (THA) is positive in Subregions 1 and 4 and negative in Subregions 2 and 3. The positive THA in Subregions 1 and 4 $(16.3 \pm 0.5) \times 10^4\ m^2\ ^oC\ /\ s$ is approximately balanced by the advective heat loss in Subregions 2 and 3 $-(15.2\ \pm\ 0.6)\ \times\ 10^4\ m^2.^oC\ /\ s$. The THA integrated over the whole area is $1.1\ \times\ 10^4\ m^2\ ^oC\ /\ s$, which is only about 7% of the total heat gain due to the THA in Subregions 1 and 4.

We also observe that the magnitude of THA shows significant zonal differences

(asymmetry), with high THA values in the western Subregions 1 and 2 and low values in the eastern Subregions 3 and 4. The magnitude of THA in the Subregion 2 is almost twice as large as the magnitude of THA in Subregion 4 and more than three times larger than the THA in Subregion 3. Both the EHA and the MHA contribute to these zonal differences (see Table 3.1). The link between the intensified THA in the western part of the region and the dynamics of main currents is discussed in the following Section 3.5.2.

The eddy heat flux advection (EHA) has significant contributions to the THA in all four subregions (see Table 1). The eddy components of u', v', T' are defined (see also Wunsch, 1999) as the variability with respect to the record mean, regardless of its dynamical cause. This variability includes intraseasonal, seasonal, and interannual processes. To assess the contributions of processes with different time scales, we separate the eddy variability in temperature (T') and velocity (u', v') over the studied period from 2003 to 2008 into sums of interannual (linear) trends ($u'_{in}, v'_{in}, T'_{in}$) and seasonal ($u'_s, v'_s, T'_s$) and intraseasonal ($u'_{is} = u' - u'_{in} - u'_s, T'_{is} = T' - T'_{in} - T'_s$) variability:

$$T' = T'_{in} + T'_s + T'_{is} \tag{3.12}$$

$$u' = u'_{in} + u'_s + u'_{is} \tag{3.13}$$

$$v' = v'_{in} + v'_s + v'_{is} \tag{3.14}$$

To calculate the interannual, seasonal, and intraseasonal components of u',and v', the eddy velocity (u', v') is first linearly interpolated onto a regular grid with a resolution of $1/4^o$. Then, the interannual trends in T'_{in}, u'_{in}, and v'_{in} are removed from the interpolated data. The contributions of the seasonal (EHA_s) and intraseasonal

	Subregion 1	Subregion 2	Subregion 3	Subregion 4
EHA_{is}	0.5 ± 0.1	0.1 ± 0.2	-0.2 ± 0.1	0.3 ± 0.1
EHA_s	-0.8 ± 0.1	-0.9 ± 0.2	0.2 ± 0.1	-0.1 ± 0.1
EHA_{cov}	-0.1 ± 0.1	0.1 ± 0.2	0.0 ± 0.1	0.0 ± 0.1
Total	-0.4 ± 0.3	-0.7 ± 0.6	0.4 ± 0.3	0.2 ± 0.3

Table 3.2: Seasonal (EHA_s) and intraseasonal (EHA_{is}, EHA_{cov}) contributions to the eddy-driven advective heat flux. The units are $10^4\ m^2\ {}^oC/s$.

(EHA_{is}) variability and the covariance (EHA_{cov}) are computed as follows:

$$EHA_s = -\int_A \overline{\mathbf{u'}_s \nabla T'_s} dA \tag{3.15}$$

$$EHA_{is} = -\int_A \overline{\mathbf{u'}_{is} \nabla T'_{is}} dA \tag{3.16}$$

$$EHA_{cov} = -\int_A \left(\overline{\mathbf{u'}_s \nabla T'_{is}} + \overline{\mathbf{u'}_{is} \nabla T'_s} \right) dA \tag{3.17}$$

The values of $EHA_s, EHA_{is}, EHA_{cov}$ integrated over the four subregions are shown in Table 3.2. The seasonal contribution to the eddy heat transport to the surface layer heat budget has the largest magnitude in Subregions 1 and 2. Our analysis (not shown here) suggests that the seasonal component of eddy heat advection in these subregions is mostly due to seasonal variability in the cores of the IC and EGC. The intraseasonal component of eddy heat transport has relatively high values in Subregions 1 and 4. This component includes variations in eddy heat flux due to processes like meanders, mesoscale eddies, and Rossby waves. The magnitudes of EHA_s, EHA_{is}, and EHA_{cov} in all four subregions (Table 3.2) are significantly smaller than the total eddy-driven THA in Table 3.1.

These smaller magnitudes in all four subregions are somewhat surprising because

the sum of the three components, EHA_{is}, EHA_s, and EHA_{cov} defines the total eddy-driven EHA. However, their estimates computed by using interpolated data are significantly smaller than the eddy EHA calculated from along-track data. The intensity of the intraseasonal variability (see Table 3.2) is significantly affected (reduced) by the interpolation of u', v' onto a regular grid with $1/4^o$ resolution.

Our analysis (not shown here) suggests that only eddies with a radius higher than 50 km in Subregions 1, 2, and 4 are not affected by the interpolation procedure.

At the same time, the event census analysis (Figure 3.2a) and the results described in Section 3.4.2 demonstrate that eddies with a radius of 50 km and larger constitute only a small part of the mesoscale eddies identified using satellite along-track sea level anomalies. Therefore, the EHA based on interpolated data (Table 3.2) does not account for the impact of many of the eddies found in the along-track observations. This result is also supported by findings of Isachsen, Koszalka & JH LaCasce (2012), who demonstrated that eddy advective heat fluxes calculated using gridded altimeter data (with $1/4^o$ resolution) are several times smaller than eddy heat fluxes calculated based on drifter observations and high-resolution model simulations.

3.5.2 Advection of Heat by the Main Current Systems

To elucidate further the links between the estimates of MHA and EHA (Table 3.1) and the dynamics of the main currents we sub-divide the four subregions into boxes with a meridional extent of 1.5 degrees. The east-west boundaries of the boxes of integration are shown as white solid lines in Figure 3.3b. They separate the studied region into four parts. The first part (see Figure 3.3b) is over the EGC north and the

EGIC south of the Denmark Strait. The second part is over the Irminger Sea. The third part includes the southern part of the Greenland Sea, the Iceland Sea, and the western part of the NADC. The fourth part is over the eastern part of the NADC and the NwAC. The MHA and EHA averaged over the boxes ,which have a width shown as white lines in Figure 3.3b and a meridional extension of 1.5^o are shown in Figure 3.7.

The mean (MHA) and eddy (EHA) heat advection integrated over the four parts are shown in Figures 3.7a, b, c, d. The highest MHA magnitudes for the whole region are observed in two of the boxes positioned north and south of the Denmark Strait (Figure 3.7a). These boxes cover the areas of branching of the EGC and IC in the vicinity of the Iceland-Greenland Ridge. South of the Denmark Strait, the IC branches at about $64^o - 65^o$N (see Figure 3.2). Its main branch turns westward and then flows southward along the Greenland shelf, while a second branch creates the origin of the North Irminger Iceland Current (NIIC). The maximum of advective heat gain (MHA) over the area of the IC is $(5.6 \pm 0.3) \times 10^4 \ \ ^oC/m^2$, which is the highest MHA value found in the whole studied region (see Figure 3.7). A minimum of the MHA is observed north of the Denmark Strait at latitudes $67^o - 69^o$N in the box covering the area where the East Icelandic Current (see Figures 3.2 and 3.3b) separates from the EGC in the vicinity of the Iceland-Greenland Ridge. The maximum heat loss due to the MHA over this area is $(-3.6 \pm 0.1) \times 10^4 \ \ ^oC/m^2$. This distribution of MHA in Figure 3.7a implies that there is a meridional variation in the mean advective heat flux contribution to the heat budget of the surface layer across the Denmark Strait. The large magnitudes of both the gradient in mean temperature and the along-gradient component of mean velocity (see Equation (3.9) in the

branches of the IC and EGC are responsible for these high MHA values (Figure 3.3b).

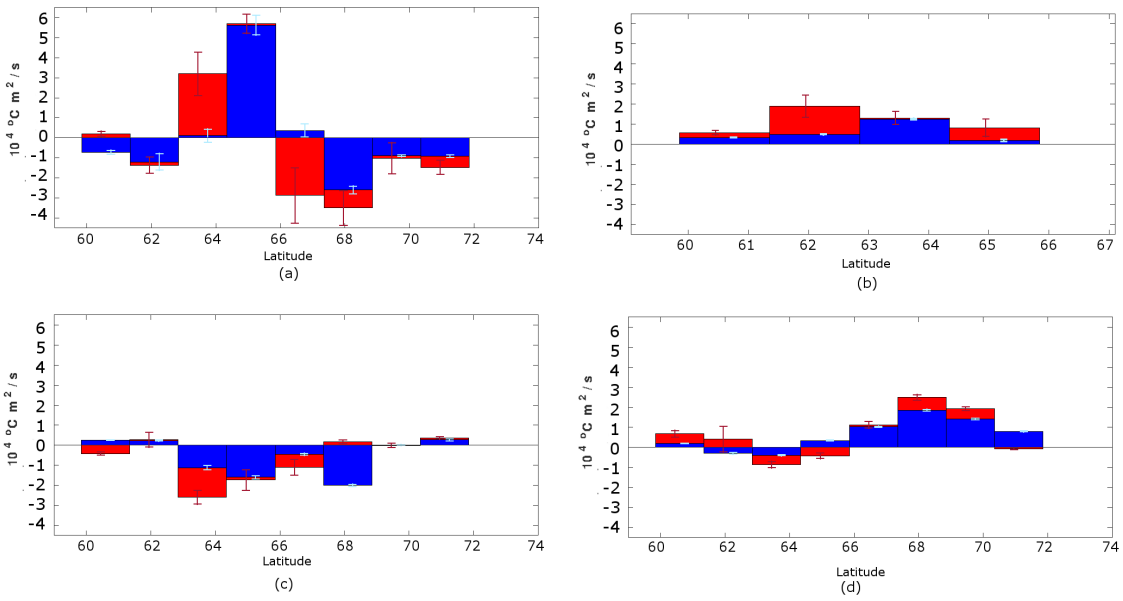

Figure 3.7: Mean (blue bars) and eddy (red bars) advective fluxes integrated over (a) the EGC and EGIC, (b) the Irminger Sea, (c) the Iceland Sea and NADC, and (d) the NwAC. The error bars represent the standard error.

The EHA and MHA integrated over the Irminger Sea (Figure 3.7b) have smaller magnitudes than those integrated over the other areas. The $THA = MHA + EHA$ in the Irminger Sea is about $1 \rightarrow 2 \times 10^4 \ \ ^oC/m^2$. A larger THA magnitude of $1.5 \rightarrow 3 \times 10^4 \ \ ^oC/m^2$ is observed in the third area (Figure 3.7c) between 63^o and 69^oN and over the Jan Mayen Current and the East Icelandic Current (EIC) (Figure 3.2). These currents bring cold and fresh Arctic waters into the central part of the Greenland and Iceland Seas. The associated advective heat loss in the surface layer over this area is

high in the Iceland Sea and along the east coast of Iceland.

Figure 3.7d shows the EHA and MHA over the NwAC. In the southern part of the NwAC, the THA (see Figure 3.7d) is negative due to the influence of the cold East Icelandic Current. This influence is maximal at about 63^o-64^oN, where the THA is about $-1 \times 10^4\ m^2\ {}^oC/s$. The positive THA over the NwAC represents the source of heat for the ocean surface layer in the area where the Atlantic Water spreads into the Norwegian Sea between latitudes 64^o and 72^oN. Both eddy and mean heat flux convergence contribute to the heat gain by the NwAC, which has a maximum of $(2.5 \pm 0.1) \times 10^4\ m^2\ {}^oC/s$ at 68^oN.

Assuming that the surface layer heat content is quasi-stationary, we can derive that

$$\int_A \left(\overline{\mathbf{u}}\nabla\overline{T} + \overline{\mathbf{u}'\nabla T'}\right) dA = \int_A \left(\frac{Q_s}{\rho c_p}\right) dA - \int_A \left(k_v \left.\frac{\partial \overline{T}}{\partial z}\right|_{z=-h} + \overline{w\frac{\partial T}{\partial z}}\right) dA + \int_A \nabla\cdot k_H \nabla\overline{T} dA \tag{3.18}$$

The left-hand side of this equation defines the mean heat advection (MHA) and the divergent part of the eddy-driven heat flux (EHA) in Figure 3.7. These fluxes are balanced by the three groups of processes represented on the right-hand side of Equation (3.18): (i) surface heat flux $Q_s/(c_p\rho)$, (ii) vertical advective and turbulent transport, and (iii) irreversible eddy-induced mixing. Our analysis (not shown here) suggests that the surface heat flux (Q_s) has a relatively small contribution to the heat budget of the surface layer over the Denmark Strait. According to Equation (3.18), the large values of MHA are balanced by the surface heat flux, vertical transport at the bottom of the surface layer and the irreversible eddy-induced mixing. These processes occur over the region where the Denmark Strait Overflow Water is formed

and spreads out. The large advection of heat has potentially important consequences for the heat content and the potential energy of the mean flow in the surface layer.

An important question that arises from this analysis is whether the results in Figure 3.7 are sensitive to the data and method used in our study. To address this question, we present MHA and EHA estimates based on independent data from the SODA ocean reanalysis version 2.2.4 (Carton & Giese, 2008). The SODA reanalysis is a global ocean simulation with 50 vertical levels and a horizontal resolution of $1/4^o \times 1/4^o$. The data assimilation scheme is an optimal interpolation that also includes a method for correcting the model bias.

Figure 3.8 shows the MHA and EHA estimated from the SODA reanalysis over the same four areas as in Figure 3.7 and for the period from 2003 to 2008. The MHA distributions computed from our data (Figure 3.7) are substantially similar to the ones calculated based on the SODA reanalysis (Figure 3.8). These two independent data sets demonstrate that the largest MHA values for the whole studied area are observed north and south of the Denmark Strait. The maximum of the MHA over the IC south of the Denmark Strait in the SODA data (Figure 3.8a) is equal to our MHA estimate in Figure 3.7a, within the standard error of the estimation. The minimum of the MHA north of the Denmark Strait (Figure 3.8b), however, is more than two times larger than our estimate based on satellite data in Figure 3.7a.

The net heat advection (THA=MHA+EHA) in the Irminger Sea (Figure 3.8b) estimated by SODA data is generally positive and close to our observational estimates (Figure 3.7b). The SODA data also show the negative THA over the Jan Mayen Current and the East Icelandic Current (EIC) at 65^o and 66^oN (see Figure 3.8c). The MHA is generally positive over the NwAC between 64^o and 72^oN (Figure 3.8d)

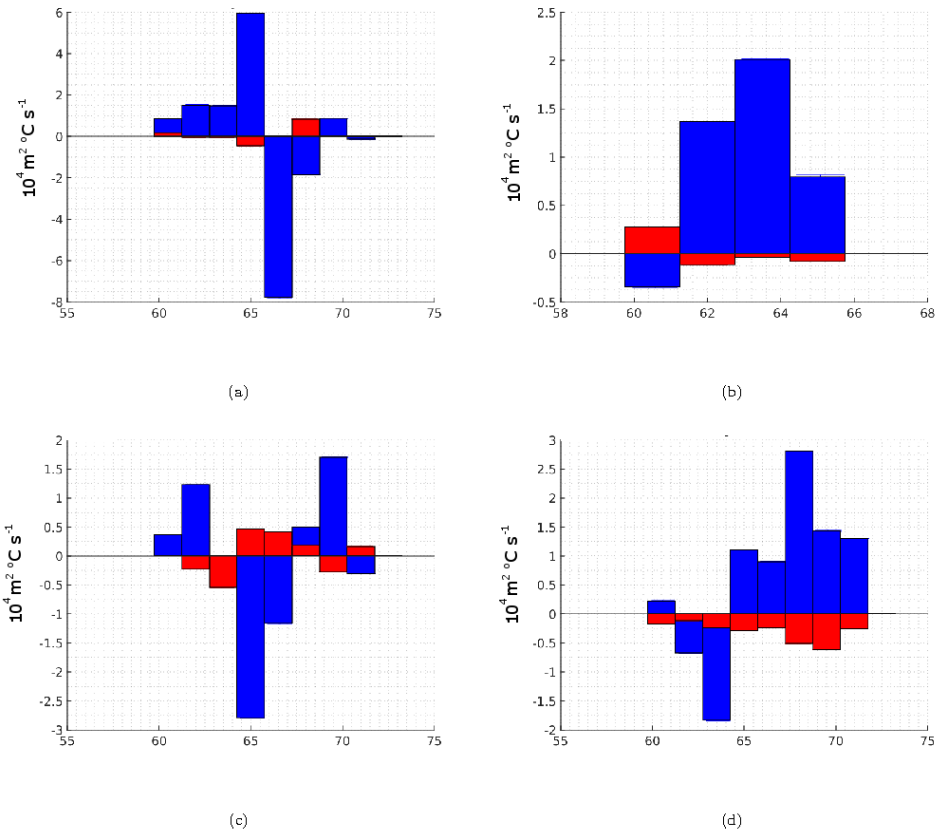

Figure 3.8: Mean (blue bars) and eddy (red bars) advective fluxes computed using SODA (Carton & Giese, 2008) data and integrated over (a) the EGC and EGIC, (b) the Irminger Sea, (c) the Iceland Sea and NADC, and (d) the NwAC.

and has a maximum of about 2.75×10^4 m^2 $^oC/s$ at 69^{o}N. This maximum occurs approximately in the area where the NwAC leaves the shallow Vøring Plateau as it flows northward along the Norwegian coast. Our estimate of this maximum from satellite data (Figure 3.7d) is $(2.5 \pm 0.1) \times 10^4$ m^2 $^oC/s$ at 68^{o}N.

The MHA distributions derived from satellite data (Figure 3.7) and SODA re-

analysis (Figure 3.8) show some minor differences. The extreme values of MHA in the estimates based on SODA data exceed our estimates in a few areas with substantial topographical irregularities. The bottom topography is a significant factor in the ocean dynamics in the region adjacent to the GSR. The details of the way in which the flow interacts with the bathymetry in z-coordinate models, however, depend on the resolution of the numerical grid, especially in regions with a steep bottom slope. We also observe that the eddy-driven EHA has a significantly smaller magnitude in SODA simulations (Figure 3.8) than in our results (Figure 3.7). The SODA model is not eddy-resolving and therefore underrepresents the eddy dynamics in this region, which, according to our estimates, have a dominant radius of about 20 km (Figure 3.2a). Beyond these minor differences, the SODA simulations and the results from our analysis agree about the main patterns in the MHA distributions in the studied region. In particular, both the results from our data analysis (Figure 3.7) and the SODA simulations (Figure 3.8) show that a substantial advective heat gain/loss in the surface layer occurs in a relatively narrow region adjacent to the Denmark Strait.

3.5.3 Irreversible Eddy-Induced Horizontal Mixing

When eddies move across the studied area, they trap waters with characteristics typical of the region of their formation. During their decay, the eddies release these waters, affecting the heat and salt content of the water column at their final position. The associated eddy-induced irreversible heat flux depends on eddy size, the path of eddy propagation, and temperature and salinity anomalies. The most significant

contributions to this flux are made by long-living and large eddies, which can travel considerable distances during their lifetime. Their impact on the heat content of the water column during eddy decay is associated with the processes of eddy stirring and small-scale turbulent mixing.

ARGO profiles were previously used to study the three-dimensional structure of ocean mesoscale eddies and their contribution to the volume, heat, and freshwater transport (Chaigneau et al. (2011) and Johnson & McTaggart (2010)). The positions and spatial characteristics of mesoscale vortices in these studies are determined based on gridded satellite altimeter observations. The ARGO profiles are used to determine the vertical structure of eddy-induced temperature and salinity anomalies of composite cyclonic and anticyclonic eddies (Chaigneau et al., 2011). We follow a similar approach in the assessment of eddy-induced temperature and salinity anomalies of mesoscale vortices detected in our study by using along-track satellite altimeter observations (see Sections 3.3.2 and 3.4.2).

The observations from ARGO profiles that remained inside individual eddies for a period longer than 12 weeks were used to compute the average eddy-induced anomalies in temperature (T) and salinity (S). Our analysis (not shown here) suggests that the T and S profiles inside eddies are determined mainly by the water mass characteristics in the region of eddy formation. They depend less on their polarity (cyclonic or anticyclonic) or on the properties of the local environment where the eddies propagate. Temperature and salinity profiles identified in this analysis are inside Subregions 1 and 4. No ARGO profiles were found inside eddies in the other two subregions (Subregions 2 and 3) for a period long enough to assess anomalies in eddy heat and salt content. Furthermore, only a few profiles were found inside the eddies in Subregion 1. Our

discussion in this section focuses only on Subregion 4.

Figure 3.9 shows the temperature and salinity anomalies inside the composite eddies in Subregion 4. The anomalies are calculated relative to the Levitus decadal climatology for the period 2005-2012 (http://data.nodc.noaa.gov). The horizontal bars show the standard deviations of the anomalies at each depth. The temperature and salinity profiles of eddies in Subregion 4 fall into two groups. The first one includes the temperature and salinity anomalies observed south of 69.5^{o}N (Figure 3.9a), and the second group (Figure 3.9b) consists of the profiles found north of 69.5^{o}N.

The maxima of eddy-induced temperature and salinity anomalies south of 69.5^{o}N are 2^o and 0.1psu, respectively (see Figure 3.9a). They are observed at about a depth of 150-200-m, which is the depth of the cores of the eddies. Below and above this depth, the anomalies decrease monotonically. The magnitudes of the eddy-induced temperature and salinity anomalies north of 69.5^{o}N (see Figure 3.9b) are similar and close to 2^o and 0.1psu, respectively. The vertical structure of the profiles, however, is different. The anomalies related to the warm eddies are relatively uniform across the whole layer, from the surface down to a depth of 500 m (Figure 3.9b). These eddies trap Atlantic Waters as they propagate in the central Norwegian Sea, keeping them exposed to surface cooling during their whole lifetime. The intense mixing and transformation of the Atlantic Water north of 69.5^{o}N cause the homogenization of the vertical thermohaline structure of the surface 500 m layer. The magnitudes of temperature and salinity anomalies in the cold eddies increase monotonically with depth and reach a maximum in their core at about 600 m deep (Figure 3.9b).

The mean geometric and thermohaline characteristics of the composite cold and warm eddies for Subregion 4 are shown in Table 3.3. The range of eddy radii used in

these calculations is between 19 km and 25 km. The average radii of warm and cold composite eddies are 21 km and 23 km, respectively. The average distance between the initial and final positions of both types of eddies is about 100 km. Their paths, however, are generally not straight lines, and the distance traveled can be several times larger than 100 km. The average lifetime of the composite eddies is about 100 days. These characteristics are used to assess the eddy-induced anomalies and the heat and salt fluxes associated with the motion of eddies. Following Hátún, Eriksen & P.B Rhines (2007) and Chaigneau et al. (2011), we first define the vertical integrals of Available Heat and Salt Anomalies (AHA and ASA):

$$AHA = \pi R_e^2 \int_{-1000m}^{0m} \rho c_p \left(\Delta T(z)\right) dz$$

and

$$ASA = \pi R_e^2 \int_{-1000m}^{0m} \left(\Delta S(z)\right) dz$$

where $\Delta T(z)$ and $\Delta S(z)$ are the temperature and salinity anomalies of each eddy. Based on the estimates of AHA and ASA, we calculate the advective heat and salt transport over the lifetimes of the eddies normalized by the depth of the surface 1000 m layer. The mean heat transport by warm and cold eddies are $-180\ ^oCm^2s^{-1}$ and $160\ ^oCm^2s^{-1}$, respectively. These values are two orders of magnitude smaller than the surface EHA estimates in Subregion 4 (see Table 3.1). The heat flux due to eddy-induced irreversible mixing is still significant because of the large number of eddies in Subregion 4 (see Section 3.4.2). Assuming that the estimated values of AHA and ASA are representative of eddies with a radius between 19 km and 25 km, the total heat transport by these eddies (referenced to a vertical thickness of 1 m) is $(1.7\pm0.3)\times10^5\ m^2\ ^oC/s$ for warm and $(-1.0\pm0.2)\times10^5\ m^2\ ^oC/s$ for cold eddies. This

flux is estimated based on the total numbers of warm (1088) and cold (639) eddies observed in Subregion 4 with radii between 19 km and 25 km over the period from 2003 to 2008. Notice that these values are 2 to 2.5 times higher than the total heat advection (THA) in the surface layer (see Table 3.1). The THA is, however, close to the estimate of the total irreversible eddy-induced heat mixing $(7 \pm 5) \times 10^4\ m^2\ {}^oC/s$ computed based on the sum of heat fluxes by warm and cold eddies.

The errors in the estimates of eddy-induced irreversible heat mixing are related to observational uncertainties in eddy radii, temperature and salinity anomalies, eddy paths, and eddy lifetimes. Moreover, these estimates are based only on ARGO profiles found inside mesoscale vortices with radii from 19 km to 25 km. There is a significant number of eddies in Subregion 4 with size greater than 25 km (see Figure 3.5) that are known to have a substantial impact on ocean dynamics and transport (see Gascard & K. Mork (2008)). In this context, the values of AHA, ASA, and heat transport found in this section should be considered as an approximation and lower limit of the real eddy-induced irreversible heat mixing. When comparing these fluxes with the divergent eddy-driven heat, we need to consider also that the latter is representative for a sub-surface mixed layer whose exact depth is generally unknown. The eddy-driven irreversible heat transport is averaged over a column of 1000 m, and its values are subject to uncertainties due to the limited number of observed eddies by ARGO observations.

The estimates of AHA and ASA for all eddies observed by ARGO profilers in Subregion 4 are presented graphically in Figure 3.10. The arrows are red for positive and blue for negative values of AHA and ASA. The thickness of the arrows is proportional to the magnitudes of AHA and ASA, and arrow length and direction

Table 3.3: Characteristics of Composite Eddies in Subregion 4.

	radius km	lifetime days	distance traveled km	AHA $\times 10^{18}$ J	ASA $\times 10^{10}$ kg	Heat flux ${}^{o}Cm^2/s$
warm eddy	21 ± 1	100 ± 30	100 ± 20	5.0 ± 1.0	5.0 ± 2.0	160 ± 30
cold eddy	23 ± 2	100 ± 20	130 ± 30	-6.0 ± 1.0	-4.0 ± 2.0	-180 ± 30

define the displacement of an eddy during its lifetime. As can be seen in Figure 3.10, the motion of eddies is somewhat chaotic. The mesoscale vortices moving in a zonal direction have the highest impact on eddy-induced heat exchange. In particular, the highest heat transport is in the Lofoten Basin and is due to eddies that propagate predominantly in a zonal direction across the NwAC. The velocities of cold eddies tend to have large southward or eastward components.

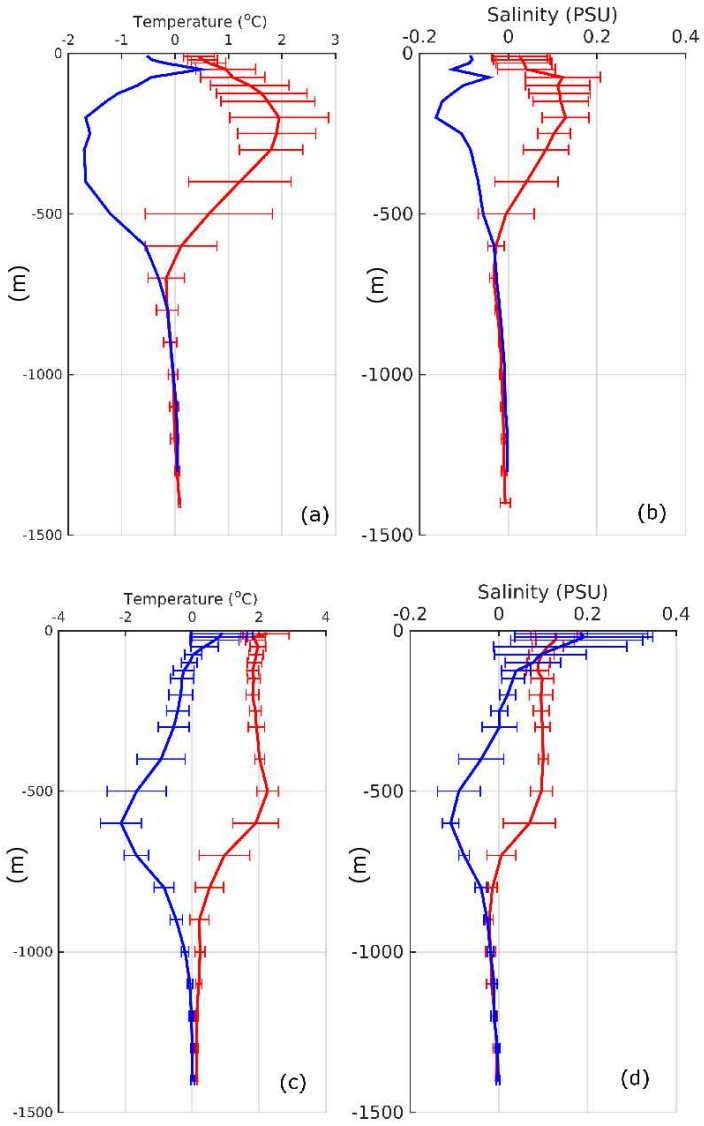

Figure 3.9: Mean vertical profiles of temperature (T) and salinity (S) inside warm (red curves) and cold (blue curves) composite eddies in Subregion 4. Figures (a) and (b) show the eddy-induced T and S anomalies south of 69.5^{o}N. Figures (c) and (d) show the eddy-induced T and S anomalies warm (red curves) and cold (blue curves) eddies north of 69.5^{o}N. The horizontal lines indicate the standard deviation of the profiles. ARGO profiles were found in only one cold eddy south of 69.5^{o}N

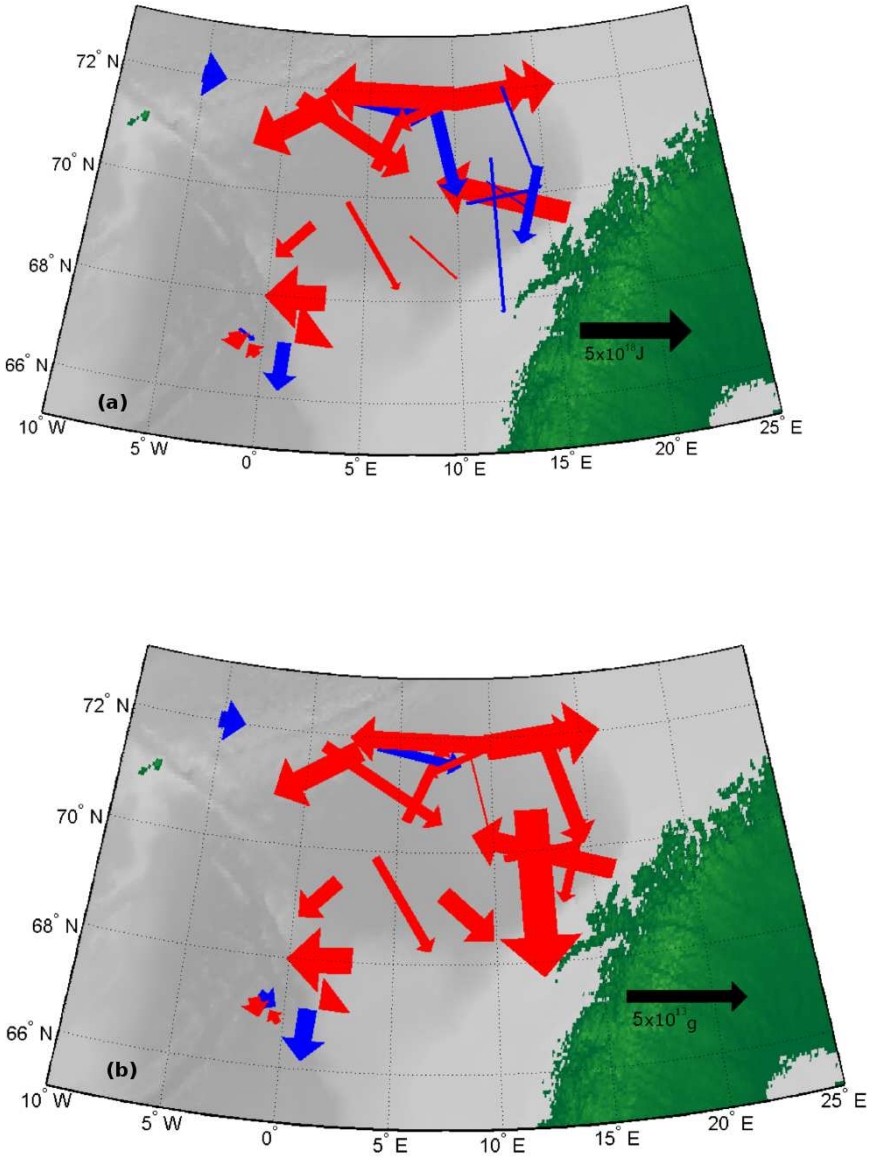

Figure 3.10: Eddy-induced (a) AHA and (b) ASA in Subregion 4. The arrows show the direction and distance traveled by eddies; the thickness of the arrows is proportional to the magnitudes of AHA and ASA. The red arrows show positive AHA and ASA while the blue arrows show the negative.

3.6 Conclusions

This article presents results from a study on advective heat fluxes in the ocean region adjacent to the Greenland-Scotland Ridge based on altimeter satellite observations and SST and ARGO data. Two types of advective fluxes are studied: (a) mean and eddy-driven divergent advective heat transport in the surface layer and (b) eddy-induced irreversible heat transfer. The results from this analysis demonstrate that there are significant zonal variations in the magnitude of heat advection in the surface layer. The heat advection is between two and three times higher in the western part of the region (see Table 3.1) than in the eastern part. This zonal asymmetry is due to intense heat advection by the mean flow (MHA) and eddies (EHA) in the ocean surface layer adjacent to the Denmark Strait. The MHA has opposite signs north and south of the strait. It is high and positive over the area where the NIIC separates from the IC in the south, whereas it is low and negative over the region where the North Icelandic Current forms north of the strait.

The intense heat advection in the surface layer over the Denmark Strait is approximately balanced by surface heat flux, vertical transport, and irreversible horizontal mixing. The strong heat advection can influence this ocean region in at least two ways: (a) it increases the meridional contrast in the heat content of the water column across the Denmark Strait, and (b) it is a source of potential energy for the mean flow.

During the studied period, most eddies (about 70%) are found in the eastern half of the studied region (Figures 3.4b, and 3.5). The heat advection due to quasi-geostrophic eddies is predominantly non-divergent (rotational) (J. Marshall & Shutts, 1981).

It is associated with the growth and decay of eddies. The rotational flux vanishes in the heat budget equation. Eddies can affect heat content through the processes of irreversible mixing and small-scale turbulence.

The distribution of eddy radii in the studied region has a maximum at 23 km. As eddies move across the studied region, they trap waters with characteristics typical of the area in which they were formed. During their decay, they rerelease these waters, affecting the heat and salt content of the water column at their final position. The associated eddy-induced irreversible heat flux depends on eddy size, the path of eddy propagation, and temperature and salinity anomalies. Our estimates of the transport by eddies and associated eddy-induced irreversible mixing exceed about two-and-a-half times the mean heat advection by the NwAC. The heat exported by warm eddies toward the central part of the Norwegian Sea exceeds two to three times the advective of heat by the NwAC. This transfer, together with the transport by cold mesoscale eddies, constitutes a potentially significant component of the heat transport in the Nordic Seas.

Acknowledgments

The altimeter satellite data used in this study are from an AVISO project (Archiving and Validation and Interpretation of Satellite Oceanographic data) available from https://www.aviso.altimetry.fr/en/home.html. The SST data are the NOAA Reynolds $1/4^o$ computed from the High Resolution SST (GHRSST) Level 4 AVHRR OI daily SST product from 2003 to 2008 available from http://ghrsst.jpl.nasa.gov. The ARGO floats data are from the US National Oceanographic Data Center available from www.nodc.noaa.gov/argo

This research was supported by the National Sciences and Engineering Research Council of Canada (NSERC) and the Ocean Frontier Institute (OFI). OFI is funded by the Canada First Research Excellence Fund and by various private and public sector organizations.

References

Abernathey, R. & J Marshall (2013). "Global surface eddy diffusivities derived from satellite altimetry". In: *Journal of Geophysical Research: Oceans* 118(2), pp. 901–916. DOI: https://doi.org/10.1002/jgrc.20066.

AMAP (1998). *AMAP assessment report: Arctic pollution issues*. Arctic Monitoring and Assessment Programme (AMAP), Oslo, Norway.

AVISO (2011). *AVISO (Archiving and Validation and Interpretation of Satellite Oceanographic data)*. Tech. rep. The altimeter products were produced by Ssalto/Duacs and distributed by Aviso, with support from Cnes.

AVISO (2013). *AVISO (Archiving and Validation and Interpretation of Satellite Oceanographic data)*. Tech. rep. GFO.

Bersch, M. (1995). "On the circulation of the northeastern North Atlantic". In: *Deep Sea Research Part I: Oceanographic Research Papers* 42(9), pp. 1583–1607.

Blindheim, J. & S Osterhus (2005). "The Nordic Seas, main oceanographic features". In: *Geophysical Monograph-American Geophysical Union* 158, p. 11. DOI: https://doi.org/10.1029/158GM03.

Brambilla, E., L. Talley & P. Robbins (2008). "Subpolar Mode Water in the northeastern Atlantic: 2. Origin and transformation". In: *Journal of Geophysical Research: Oceans* 113(C4). DOI: https://doi.org/10.1029/2006JC004063.

Brath, M. et al. (2010). "Altimeter-based estimates of eddy variability and eddy transports in the subpolar North Atlantic". In: *Marine Geodesy* 33(S1), pp. 472–503.

Carton, J. & B. Giese (2008). "A reanalysis of ocean climate using Simple Ocean Data Assimilation (SODA)". In: *Monthly Weather Review* 136(8), pp. 2999–3017.

Chaigneau, A. et al. (2011). "Vertical structure of mesoscale eddies in the eastern South Pacific Ocean: A composite analysis from altimetry and Argo profiling floats". In: *Journal of Geophysical Research: Oceans* 116(C11). DOI: https://doi.org/10.1029/2011JC007134.

Chelton, D., M. Schlax & R. Samelson (2011). "Global observations of nonlinear mesoscale eddies". In: *Progress in Oceanography* 91(2), pp. 167–216. DOI: https://doi.org/10.1016/j.pocean.2011.01.002.

Chinn, B. & S. Gille (2007). "Estimating eddy heat flux from float data in the North Atlantic: The impact of temporal sampling interval". In: *Journal of Atmospheric*

and Oceanic Technology 24(5), pp. 923–934. DOI: https://doi.org/10.1175/JTECH2057.1.

Conger, AM et al. (2009). "GFO and JASON Altimeter Engineering Assessment Report. Update: GFO-Acceptance to End of Mission on October 22, 2008, JASON-Acceptance to September 29, 2008". In:

Dickson, R.R. & J. Brown (1994). "The production of North Atlantic Deep Water: sources, rates, and pathways". In: *Journal of Geophysical Research: Oceans* 99(C6), pp. 12319–12341. DOI: https://doi.org/10.1029/94JC00530.

Dussurget, R. et al. (2011). "Fine resolution altimetry data for a regional application in the Bay of Biscay". In: *Marine Geodesy* 34(3-4), pp. 447–476. DOI: https://doi.org/10.1080/01490419.2011.584835.

Eden, C. (2010). "Anisotropic rotational and isotropic residual isopycnal mesoscale eddy fluxes". In: *Journal of Physical Oceanography* 40(11), pp. 2511–2524. DOI: https://doi.org/10.1175/2010JPO4397.1.

Fan, X. et al. (2013). "Observations of Irminger Sea anticyclonic eddies". In: *Journal of Physical Oceanography* 43(4), pp. 805–823. DOI: https://doi.org/10.1175/JPO-D-11-0155.1.

Gascard, J. & K. Mork (2008). "Climatic importance of large-scale and mesoscale circulation in the Lofoten Basin deduced from Lagrangian observations". In: *Arctic–Subarctic Ocean Fluxes*. Springer, pp. 131–143.

Glessmer, M. et al. (2014). "Atlantic origin of observed and modelled freshwater anomalies in the Nordic Seas". In: *Nature Geoscience* 7(11), p. 801. DOI: https://doi.org/10.1038/ngeo2259.

Hanawa, K. & L. Talley (2001). ".4 Mode waters". In: *International Geophysics*. Vol. 77. Elsevier, pp. 373–386. DOI: https://doi.org/10.1016/S0074-6142(01)80129-7.

Hansen, B. & S Østerhus (2000). "North atlantic–nordic seas exchanges". In: *Progress in oceanography* 45(2), pp. 109–208. DOI: https://doi.org/10.1016/S0079-6611(99)00052-X.

Hátún, H., C. Eriksen & P.B Rhines (2007). "Buoyant eddies entering the Labrador Sea observed with gliders and altimetry". In: *Journal of Physical Oceanography* 37(12), pp. 2838–2854. DOI: https://doi.org/10.1175/2007JPO3567.1.

Hurlburt, H. et al. (2008). "Steering of upper ocean currents and fronts by the topographically constrained abyssal circulation". In: *Dynamics of Atmospheres and Oceans* 45(3-4), pp. 102–134. DOI: https://doi.org/10.1016/j.dynatmoce.2008.06.003.

Ikeda, M et al. (1989). "A process study of mesoscale meanders and eddies in the Norwegian Coastal Current". In: *Journal of Physical Oceanography* 19(1), pp. 20–35. DOI: https://doi.org/10.1175/1520-0485.

Isachsen, P.E., I Koszalka & JH LaCasce (2012). "Observed and modeled surface eddy heat fluxes in the eastern Nordic Seas". In: *Journal of Geophysical Research: Oceans* 117(C8). DOI: https://doi.org/10.1029/2012JC007935.

Johnson, G. & K. McTaggart (2010). "Equatorial Pacific 13 C water eddies in the eastern subtropical South Pacific Ocean". In: *Journal of Physical Oceanography* 40(1), pp. 226–236. DOI: https://doi.org/10.1175/2009JPO4287.1.

Lilly, J.M. (2002). "Observations of the Labrador Sea eddy field". PhD thesis. University of Washington.

Lilly, J.M. et al. (2003). "Observations of the Labrador Sea eddy field". In: *Progress in Oceanography* 59(1), pp. 75–176. DOI: https://doi.org/10.1016/j.pocean.2003.08.013.

Lundrigan, S. & E. Demirov (2012). "Long-Term Variability of Volume and Heat Transport in the Nordic Seas: A Model Study". In: *Atmosphere-Ocean* 50(2), pp. 156–168. DOI: https://doi.org/10.1080/07055900.2012.683769.

Marshall, J. & G. Shutts (1981). "A note on rotational and divergent eddy fluxes". In: *Journal of Physical Oceanography* 11(12), pp. 1677–1680. DOI: https://doi.org/10.1175/1520-0485.

Mauritzen, C. (1996a). "Production of dense overflow waters feeding the North Atlantic across the Greenland-Scotland Ridge. Part 1: Evidence for a revised circulation scheme". In: *Deep Sea Research Part I: Oceanographic Research Papers* 43(6), pp. 769–806. DOI: https://doi.org/10.1016/0967-0637(96)00037-4.

Mauritzen, C. (1996b). "Production of dense overflow waters feeding the North Atlantic across the Greenland-Scotland Ridge. Part 2: An inverse model". In: *Deep Sea Research Part I: Oceanographic Research Papers* 43(6), pp. 807–835. DOI: 10.1016/0967-0637(96)00038-6..

McCartney, M. & L. Talley (1982). "The subpolar mode water of the North Atlantic Ocean". In: *Journal of Physical Oceanography* 12(11), pp. 1169–1188. DOI: https://doi.org/10.1175/1520-0485(1982)012<1169:TSMWOT>2.0.CO;2.

Meincke, J, B Rudels & HJ Friedrich (1997). "The Arctic Ocean–Nordic Seas thermohaline system". In: *ICES Journal of Marine Science* 54(3), pp. 283–299.

Mork, K. & Ø. Skagseth (2010). "A quantitative description of the Norwegian Atlantic Current by combining altimetry and hydrography". In: *Ocean Science* 6(4), pp. 901–911. DOI: https://doi.org/10.5194/os-6-901-2010.

Mork, M. (1981). "Circulation phenomena and frontal dynamics of the Norwegian Coastal Current". In: *Philosophical Transactions of the Royal Society of London A: Mathematical, Physical and Engineering Sciences* 302(1472), pp. 635–647. DOI: 10.1098/rsta.1981.0188.

Myers, P., N. Kulan & M. Ribergaard (2007). "Irminger water variability in the West Greenland Current". In: *Geophysical Research Letters* 34(17). DOI: https://doi.org/10.1029/2007GL030419.

NOAA & NODC (2007). *Operational oceanography group: Global ARGO data*. Tech. rep. date of access: July 2012. National Oceanic Atmospheric Administration.

Osborn, T. & C. Cox (1972). "Oceanic fine structure". In: *Geophysical & Astrophysical Fluid Dynamics* 3(1), pp. 321–345. DOI: https://doi.org/10.1080/03091927208236085.

Pickart, R., D. Torres & P. Fratantoni (2005). "The east Greenland spill jet". In: *Journal of Physical Oceanography* 35(6), pp. 1037–1053. DOI: https://doi.org/10.1175/JPO2734.1.

Reynolds, R. et al. (2007). "Daily high-resolution-blended analyses for sea surface temperature". In: *Journal of Climate* 20(22), pp. 5473–5496. DOI: https://doi.org/10.1175/2007JCLI1824.1.

Rudels, B., E. Fahrbach, et al. (2002). "The East Greenland Current and its contribution to the Denmark Strait overflow". In: *ICES Journal of Marine Science* 59(6), pp. 1133–1154. DOI: https://doi.org/10.1006/jmsc.2002.1284.

Rudels, B., H. Friedrich & D. Quadfasel (1999). "The Arctic circumpolar boundary current". In: *Deep Sea Research Part II: Topical Studies in Oceanography* 46(6-7), pp. 1023–1062. DOI: https://doi.org/10.1016/S0967-0645(99)00015-6.

Serreze, M. et al. (2006). "The large-scale freshwater cycle of the Arctic". In: *Journal of Geophysical Research: Oceans* 111(C11). DOI: https://doi.org/10.1029/2005JC003424.

Stammer, D. & C. Dieterich (1999). "Space-borne measurements of the time-dependent geostrophic ocean flow field". In: *Journal of Atmospheric and Oceanic Technology* 16(9), pp. 1198–1207. DOI: https://doi.org/10.1175/1520-0426(1999)016<1198:SBMOTT>2.0.CO;2.

Straneo, F. (2006). "Heat and freshwater transport through the central Labrador Sea". In: *Journal of Physical Oceanography* 36(4), pp. 606–628. DOI: https://doi.org/10.1175/JPO2875.1.

Tran, N et al. (2002). "Assessment of the cycle-to-cycle noise level of the Geosat Follow-On, TOPEX, and Poseidon altimeters". In: *Journal of Atmospheric and Oceanic Technology* 19(12), pp. 2095–2107. DOI: https://doi.org/10.1175/1520-0426(2002)019<2095:AOTCTC>2.0.CO;2.

Veron, AJ et al. (1999). "Stable lead isotopic ratios trace thermohaline circulation in the subarctic North Atlantic". In: *Deep Sea Research Part II: Topical Studies in Oceanography* 46(5), pp. 919–935. DOI: https://doi.org/10.1016/S0967-0645(99)00009-0.

Wunsch, C. (1999). "Where do ocean eddy heat fluxes matter?" In: *Journal of Geophysical Research: Oceans* 104(C6), pp. 13235–13249. DOI: https://doi.org/10.1029/1999JC900062.

Yashayaev, I. & D. Seidov (2015). "The role of the Atlantic Water in multidecadal ocean variability in the Nordic and Barents Seas". In: *Progress in Oceanography* 132, pp. 68–127. DOI: https://doi.org/10.1016/j.pocean.2014.11.009.

Zhu, J & E Demirov (2011). "On the mechanism of interannual variability of the Irminger Water in the Labrador Sea". In: *Journal of Geophysical Research: Oceans* 116(C3). DOI: https://doi.org/10.1029/2009JC005677.

Connecting Text

This article addresses objective 5 described in Section 1.5.3

The results in Chapter 3 demonstrate that the convergence of advective heat flux in the surface layer has the largest magnitude in a relatively small area near the Denmark Strait. The convergence of heat flux there exceeds several times the values of this characteristic in the rest of the region. The question if and how this pattern projects in the subsurface distribution of the heat flux convergence can not be answered using surface satellite observations only.

The following article presents results from a study of the vertical structure and temporal variability of convergence of the advective fluxes of temperature and salinity based on an ocean reanalysis. The reanalysis data are obtained by using a numerical model and data assimilation.

At time of thesis completion, this article has been submitted for publication.

Chapter 4

Vertical Structure and Temporal Variability of Heat and Salt Flux Convergence over the Greenland-Scotland Ridge Derived from SODA Ocean Reanalysis

4.1 Abstract

The article presents results from the analysis of the vertical structure of the convergence of horizontal advective fluxes of heat (HFC) and salt (SFC) over the Greenland-Scotland Ridge. The fluxes are calculated from the ocean reanalysis Simple Ocean Data Assimilation (SODA) for the period from 1965 to 2010. Empirical orthogonal

function analysis is used to study the dominant modes of coherent spatial variability of HFC and SFC. Results from the analysis of the HFC and SFC in the surface layer are in good agreement with our previous study based on satellite data. Therefore, the article focuses on the "fingerprints" in the water column of the patterns in the surface distribution of HFC and SFC identified from observations.

Based on analysis of the HFC and SFC derived from the SODA reanalysis we found that (1) the mean HFC and SFC over the Denmark Strait and Iceland-Faroe Ridge exceed by an order of magnitude the HFC and SFC in the Irminger Sea and are more than twice as large as these characteristics in the Norwegian Sea; (2) The layer of high HFC over the Denmark Strait extends through the whole water column with the maximum at the surface, while the high values of SFC over both the Denmark Strait and Iceland-Faroe Ridge are observed at intermediate depths between 500 m and 1500 m. (3) The spatial distribution of the HFC and SFC in the Irminger Sea includes two characteristic features in the upper 1500 m layer in the northern part of the basin, a layer of negative HFC and SFC at depths 1500 - 2000 m, and a surface area of negative HFC in the central part of the subpolar gyre. (4) The time variability of the HFC and SFC over the Greenland-Scotland Ridge is dominated by modes of coherent oscillations in the two characteristic features over the Denmark Strait and Iceland-Faroe Ridge.

4.2 Introduction

The ocean stores about 84% of the heat added to the climate system by global warming (Levitus et al., 2000). The related rise in ocean temperature is a major contributor

to human-induced changes in sea level and has profound effects on the sea-ice and ocean environment (Stocker, 2014; Kuhlbrodt & Gregory, 2012). The impact of climate warming on the ocean heat content, however, is non-uniform across the planet (Barnett et al., 2005). The heat absorbed in the surface layer is distributed in a complex way by the ocean currents and mixing. This transport plays a fundamental role in global and regional climate dynamics (C.D. Roberts et al., 2016).

Factors that affect regional variations in the ocean's heat content include surface forcing and ocean advection and diffusion. Observational estimates of the contribution of ocean transport to the heat budget are often determined as the residue of the surface radiative and turbulent heat flux and the time derivative of the heat content (see C. Roberts et al., 2017). These estimates include the effects of wind-driven transport, advection by the mean currents, and diffusion. The results of C. Roberts et al. (2017) demonstrated, in particular, that in areas with strong currents, apart from the ocean regions of deep convection and intense water mass transformation, interannual variations in the ocean's heat content are dominated by advection. The effect of advective transport in these regions on the heat budget can be comparable and even stronger than the contribution of the surface air-sea exchange (Barnett et al., 2005).

This article presents results from a study of the convergence of ocean advective heat and salinity fluxes in the region adjacent to the Greenland-Scotland Ridge (GSR). It is an ocean region of intense winter convection and water mass transformation (Brambilla, Talley & Robbins, 2008; Mauritzen, 1996a; Mauritzen, 1996b) driven by the air-sea exchange and ocean mixing (Isachsen, Koszalka & JH LaCasce, 2012). The Atlantic waters enter this region along the multiple branches of the North At-

lantic Current (Figure 4.1a). In the subpolar gyre, they progressively lose their heat due to the air-sea exchange and form the surface Subpolar Mode Water (SPMW) (McCartney & Talley, 1982). The SPMW is vertically nearly uniform and gradually change as it spreads horizontally (Brambilla, Talley & Robbins, 2008). A remnant of the SPMW called the Irminger water spreads (see Myers, Kulan & Ribergaard, 2007) at intermediate depths and plays a significant role in the heat budgets of the Irminger and Labrador Seas (Myers, Kulan & Ribergaard, 2007; Straneo, 2006; Zhu & Demirov, 2011).

North of the GSR, the surface Atlantic Water is intensively transformed and cooled as it is transported northward by the Norwegian Atlantic Current (NwAC) (Mauritzen, 1996a; Mauritzen, 1996b)). The processes of air-sea exchange, advection by mean currents, and eddy-induced diffusion are the main drivers of the transformation of Atlantic Water. Mesoscale eddies in this region play an essential role in the transformation of the Atlantic Water and the exchange of heat and freshwater between the NwAC and the central part of the Norwegian Sea. Isachsen, Koszalka & JH LaCasce (2012) found in particular that the horizontal eddy-induced heat transport in the NwAC is "of first-order importance to the total buoyancy budget of the region and, ultimately, to the exchanges across the Greenland-Scotland Ridge." In the western part of the ocean region adjacent to the GSR, the East Greenland Current (EGC) transports cold and fresh waters (see Figure 4.1a) and sea ice of Arctic origin along the coast of Greenland (B. Rudels, Fahrbach, et al., 2002). The EGC partly branches north of the GSR and forms the Jan Mayen Current and the East Iceland Current (Figure 4.1a). Part of the waters of the EGC enter the North Atlantic through the Denmark Strait and spread along the Eastern Greenland Coast. The horizontal heat

flux convergence (HFC) and salt flux convergence (SFC) determine the impact of the transport by the currents on the local budgets of heat and salt.

The observational estimates in our previous study (Lundrigan & Demirov, 2019) show that the HFC in the surface layer of the ocean region adjacent to the GSR is spatially non-uniform. Over the Denmark Strait (see Figure 7 in Lundrigan & Demirov, 2019), the surface-layer HFC has a magnitude several times that of this characteristic in the rest of the region. The available subsurface observations of the ocean are rather sparse in space and time and do not allow the study of the subsurface projection of the observed surface patterns of the HFC. Instead, an ocean reanalysis is used in this article to estimate the subsurface distribution of the HFC and SFC.

A combination of models and data were previously used by Barnett et al. (2005) to identify the characteristics and vertical extension of the surface warming and their geographical variations. These authors found in particular that the warming signal in the North Atlantic extends to depths of about 700 m. Another model study by Meehl et al. (2011) demonstrated that the warming of the water column is not vertically homogeneous. Here, we study the subsurface structure of the advective heat flux convergence (HFC) and salt flux convergence (SFC) in model simulations of the ocean region adjacent to the GSR in an attempt to identify the vertical projection of the observational estimates of the surface HFC found by (Lundrigan & Demirov, 2019).

The article is organized as follows: The data and methods of our analysis are presented in Section 4.3. Section 4.4 describes the vertical structure of the convergence of HFC and SFC in the ocean region adjacent to the GSR. Section 4.5 presents the results from EOF analysis of the HFC and SFC. Finally, the discussion in Section 4.6 focuses on the physical causes of the HFC and SFC found in SODA model reanalysis.

4.3 Data and Method of Analysis

In this study, we use the SODA ocean reanalysis, version 3 (Carton & Giese, 2008) in the ocean region adjacent to the GSR. The SODA reanalysis system is based on the GFDL MOM-5 ocean model coupled to the SIS1 (Sea Ice Simulator) sea-ice model (Griffies, 2012). The numerical grid is irregular, with an average resolution of about $1/4^o$. The ocean model grid size is about 28 km at the equator and down to less than 10 km at polar latitudes (Carton, Chepurin & Chen, 2018). SODA uses a data assimilation scheme of ocean observations for the correction of the model errors and biases. Model output includes monthly mean temperature, salinity, and velocity interpolated on a regular 0.5^o horizontal grid with 50 vertical levels for the period from 1965 to 2010. Our previous estimates based on SODA (Figure 8 in Lundrigan & Demirov (2019)) showed a very good agreement with the observed (Figure 7 in Lundrigan & Demirov (2019)) heat flux convergence in the surface layer. The goal of the present article is to understand the vertical structure of the convergence of heat and salt fluxes and the subsurface projection of the patterns observed in the observational and SODA surface characteristics of HFC and SFC by Lundrigan & Demirov (2019).

To elucidate the links between estimates of convergences of heat and salinity advective fluxes and the dynamics of the main currents, we subdivide the studied region into four subregions with zonal boundaries shown as black solid lines in Figure 4.1b. The first subregion is over the Eastern Greenland Current (EGC) to the north and over the Eastern Greenland and Irminger Current (EGIC) to the south of the Denmark Strait. The second subregion is over the Irminger Sea. The third includes the

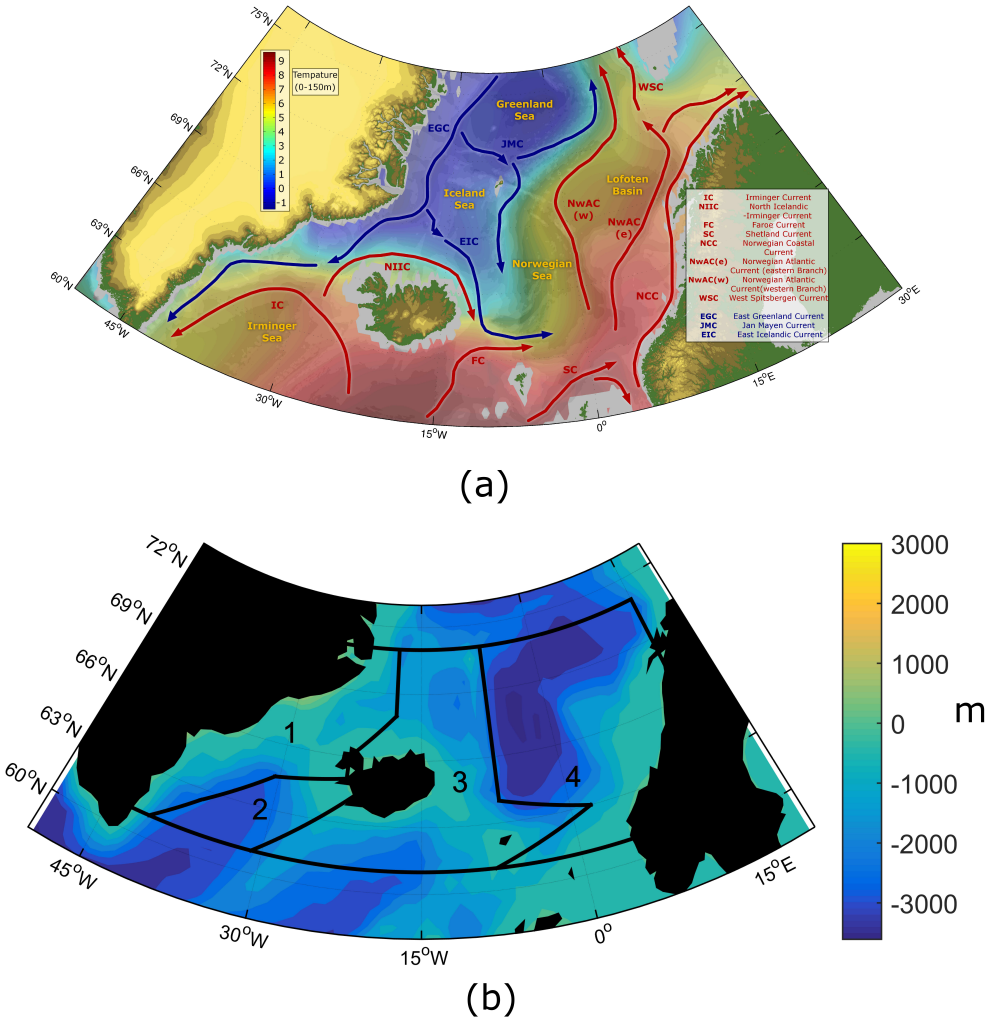

Figure 4.1: (a) Sea Surface Temperature in the Northeast Subpolar North Atlantic Ocean and Nordic Seas, bottom topography, and major currents (after AMAP, 1998). (b) The boundaries of the four subregions.

southern part of the Greenland Sea, the Iceland Sea, and the western part of the North Atlantic Drift Current (NADC). The fourth subregion is over the eastern part of the North Atlantic Drift Current and the Norwegian Atlantic Current (NwAC). The boundaries of the subregions are defined based on consideration of the topography of the studied ocean basin (Figure 4.1b). Notice that there are small differences between (Figure 4.1b) and the boundaries of the subregions used in our previous work (Lundrigan & Demirov, 2019). The latter were determined based on sea surface temperature (see Figure 3c in Lundrigan & Demirov, 2019).

The HFC and SFC is averaged over the boxes ,which have a width shown as black lines in Figure 4.1b and a meridional extension of 1.5^o. The zonally averaged advective heat flux convergence (HFC) in the four subregions for each 1.5^o meridional slice is calculated as:

$$HFC = -\frac{\rho_0 c_p}{L} \int_{\lambda_W}^{\lambda_E} \tilde{\mathbf{u}} \cdot \nabla T (R_e \cos\varphi) d\lambda \tag{4.1}$$

where $\tilde{\mathbf{u}}$ is the monthly mean vector of horizontal velocity, ∇ is the horizontal gradient operator, T is the monthly mean temperature, R_e is the Earth's radius, and λ_W and λ_E determine the longitudes of the western and eastern boundaries of each of the subregions (see Figure 4.1) correspondingly. The length of the path of integration is $L = \int_{\lambda_W}^{\lambda_E} R_e \cos\varphi d\lambda$. The HFC (see Equation 4.1) is a negative dot product of the vectors of horizontal velocity and temperature gradient. Therefore, the largest magnitudes of the HFC are observed in regions of high horizontal temperature gradients and where the current velocity has a significant component across the isotherms.

Similarly, the convergence of advective flux of salt (SFC) is defined as

$$SFC = -\frac{\rho_0 c_p}{L} \int_{\lambda_W}^{\lambda_E} \tilde{\mathbf{u}} \cdot \nabla S(R_e \cos\varphi) d\lambda$$

where S is the monthly mean salinity. The HFC (W/m^3) and SFC ($g/m^3/s$) represent the density of the gain/loss of heat and salt per unit volume in each of the four subregions.

4.4 Vertical Structure of the Convergence of Mean Heat and Salt Fluxes

The vertical sections of HFC and SFC estimates based on SODA reanalysis in the four subregions are shown in Figure 4.2 and Figure 4.3, respectively. The HFC and SFC are calculated as mean zonal convergence of the advective fluxes of heat and salt averaged for the period of time from 1965 to 2010. As such they determine the local long-term mean gain/loss of heat and salt due to the advection over the region adjacent to the GSR.

The HFC and SFC in Subregion 1 are positive in the area south of the Denmark Strait between latitudes 63^oN and 66^oN. The values of both characteristics have maximums in a narrow area just south of the Denmark Strait and at about 65 N. The HFC in this area has values higher than 200 W/m^3 in the upper 1500 m layer with a maximum at the surface of 450 W/m^3. In agreement with the observational estimates by Lundrigan & Demirov (2019) this value is higher than the surface HFC magnitudes in the other three subregions (Figures 4.2). As in the observational estimates of Lundrigan & Demirov (2019) the values of HFC are negative at the surface north of

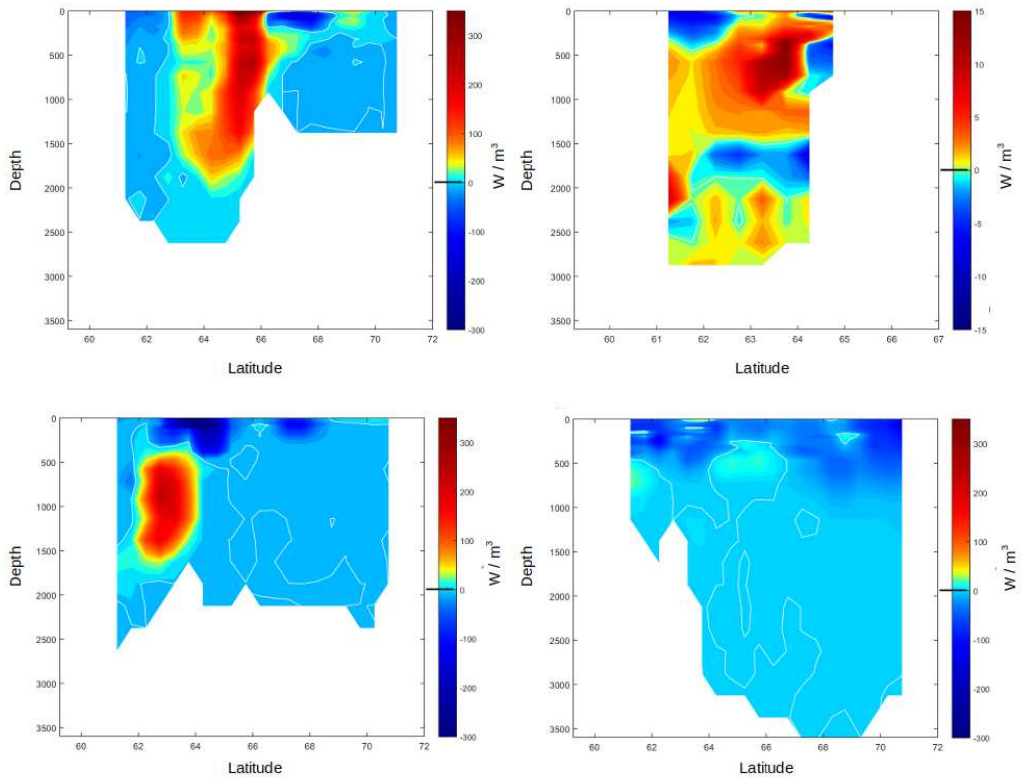

Figure 4.2: The HFC estimates based on SODA reanalysis in the four subregions. Note the different scale used in Subregion 2

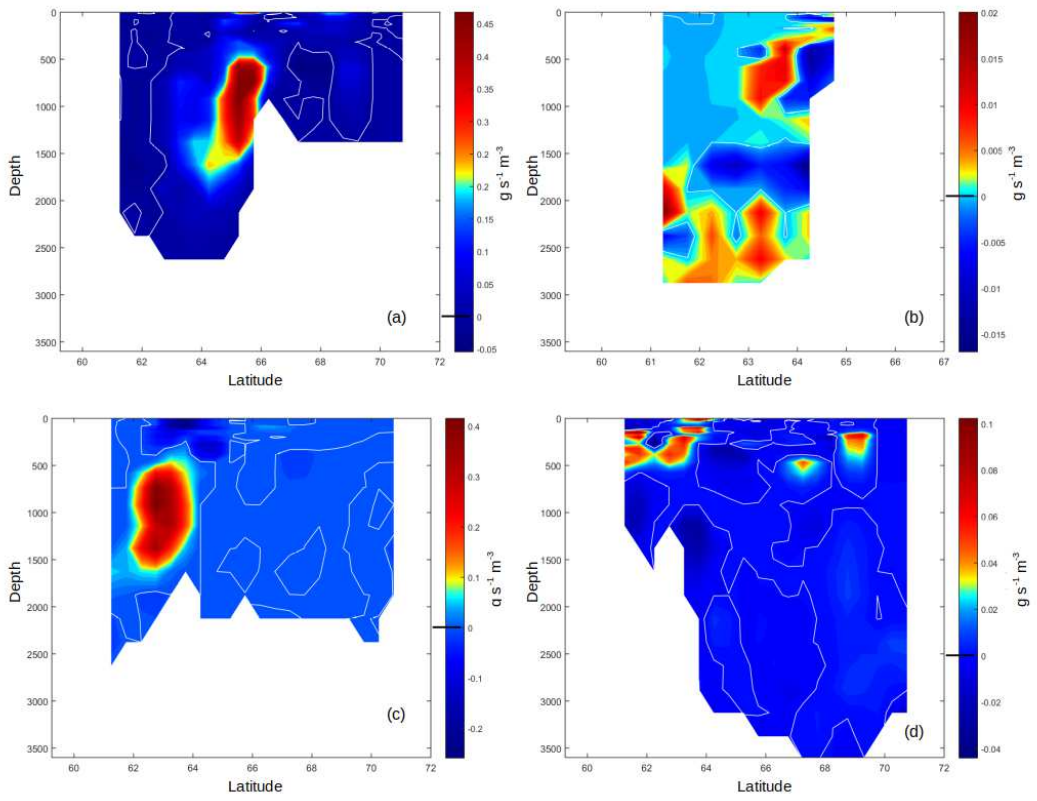

Figure 4.3: The SFC estimates based on SODA reanalysis in the four subregions.

the Denmark Strait. In Figure 4.2a this layer of negative HFC extends meridionally between latitudes of 66^oN and 69.5^oN and vertically down to depths of about 300 m.

The maximum of SODA based estimates of the SFC in Subregion 1 (Figure 4.3a) is observed in the layer between 500 m and 1500 m at latitude 65.5^oN. The SFC values in this layer exceed by an order of magnitude the SFC in Subregion 2 and are several times higher than the SFC in the Subregion 4. Unlike the HFC, however, the layer of high SFC do not extend above the 500 m depth where the values of SFC are relatively low.

In good agreement with the observational estimates (see Lundrigan & Demirov, 2019)), the values of HFC in the surface layer of the Subregion 2 (Figure 4.2b) are significantly smaller than the HFC estimates in the other three subregions. The HFC and SFC at all depths are also smaller than in the three other subregions. Three major patterns in HFC and SFC are observed in the vertical section over Subregion 2. The first one is a dipole in HFC and SFC in the surface 1500 m layer the northern part of the subregion in the vicinity of the Denmark Strait. While the dipole extends vertically down to about 1500 m, the magnitudes of HFC and SFC are relatively small below 1000 m. The second pattern is an intermediate layer of negative HFC and SFC at depths between 1500 and 2000 m (see Figures 4.2b 4.3b). Finally, negative HFC and SFC values are present in the surface 500 m layer of the southern part of the region which is over the central part of the subpolar gyre in the Irminger Sea.

The observational estimates of HFC in the surface layer of Subregion 3 by Lundrigan & Demirov (2019) are negative over the Iceland-Faroe Ridge. The SODA-based estimates of surface HFC and SFC are also predominantly negative in this region. The layer of negative HFC and SFC in this part of Subregion 3 extends from the

surface down to 300 m (Figures 4.2c 4.3c). The values HFC and SFC in the layer between 500 m and 1500 m over the Iceland-Faroe Ridge are relatively high with a HFC maximum of 200 W/m^3 and SFC maximum of 0.4 $g/m^3/s$ in the 500-1500 m.

The HFC and SFC have relatively small magnitudes in Subregion 4. The HFC in this subregion varies between -140 W/m^3 and 40 W/m^3 (Figure 4.2d). The values of SFC are between -0.04 $g/m^3/s$ and 0.1 $g/m^3/s$ (Figure 4.3d). The distribution of HFC and SFC in the surface 500 m layer of the southern part of Subregion 4 is "patchy" where areas of negative HFC and SFC are irregularly distributed within areas of positive HFC and SFC. In the layer below 500 and between latitudes 61^{o}N and 66^{o}N (Figures 4.2d, 4.3d) the values of HFC low positive and the SFC are low negative. In the northern part of the Subregion 4, the negative HFC in the surface 500 m has a large magnitude (about -140 W/m^3) while the SFC in this area is close to zero.

The GSR restricts the exchange of deep and intermediate waters between the North Atlantic and the Nordic Seas. The transport of surface and overflow waters is limited mostly to the flow through the shallow Denmark Strait, over the Iceland-Faroe Ridge, and Faroe-Shetland Channel. The limitations on the meridional transport imposed by the GSR and the co-presence of the cold and fresh waters of the Nordic Seas and warm and salty waters of the Atlantic Ocean intensify the meridional temperature gradients (see Figure 4.1a) across the GSR. The SODA based estimates of HFC and SFC indicate that strongest heat and salt advective fluxes occur over the southern parts of Denmark Strait and Iceland-Faroe Ridge. These are the areas where the Irminger Current branches south of the Denmark Strait (Figures 4.2a, 4.3a) and where the Central Iceland Basin Branch separates from the North Atlantic Current

south of the Iceland-Faroe Ridge (Figures 4.2a, 4.3a). The dynamics of these currents over the complex bottom topography south of the GSR generates strong ageostrophic components of current velocity across the isotherms. The distribution of current velocity and large meridional temperature gradients both contribute to the large values of the HFC (Equation 4.1) and SFC (Equation 4.3).

Another important pattern in the SODA based estimates of HFC and SFC is the presence of a surface layer of negative HFC north of the GSR in Subregions 1, 3, and 4. Lundrigan & Demirov (2019) explained this pattern with the impact which the Eastern Icelandic Current (EIC) (see Figure 4.1a) has on the surface layer in this part of the studied area. The EIC branches from the EGC at about $66-67^{o}$N in Subregion 1. It flows southeastward across the Subregion 3 and approaches the southern part of the Subregion 4. The HFC in the surface 300-500 m layer along the path of this current is negative representing the net heat loss due to the spreading and mixing of the polar water in the surface modified Atlantic Water. Another surface layer of negative HFC is observed in the northern part of the Subregion 4 (Figure 4.2d) where the Jan Mayen Current separates into two branches flowing in the Greenland and Iceland Sea respectively (Figure 4.1a)

4.5 Interannual variability of HFC and SFC

To study the dominant patterns of interannual variability of the convergence of heat and salt advective fluxes in the ocean region adjacent to the GSR, in this section, we present results from the Empirical Orthogonal Function analysis of the HFC and SFC for the period from 1965 to 2010. The seasonal cycle is removed from the data

	Subregion 1	Subregion 2	Subregion 3	Subregion 4
HFC	60%	52%	66%	43%
SFC	84%	63%	85%	60%

Table 4.1: The variance explained by the first EOFs of HFC and SFC for each of the subregions.

prior the EOF calculations. The dominant (first) EOFs calculated from the monthly mean fields of HFC and SFC for the four subregions are shown in Figures 4.4 and 4.5.

The variance explained by the first EOFs of HFC and SFC is correspondingly 60% and 84% in Subregion 1 and 66% and 85% in Subregion 3. In Subregion 2 the variance explained by the first EOFs is smaller, 52% for the EOF of HFC and 63% for the EOF of SFC. The lowest variance related to the first EOF was found in Subregion 4, 43% for the EOF of HFC and 60% for the EOF of SFC correspondingly.

The dominant EOFs are calculated separately for HFC and SFC. Therefore, they do not necessarily represent coherent variations in the two characteristics. To assess how strong the HFC and SFC dominant EOFs are related, we calculated the correlation coefficients of their principal components (see Table 4.2).

The correlation coefficients between the dominant modes of HFC and SFC are high and statistically significant only in the Subregion 1 (r=0.65, p-value = 10^{-6}) and Subregion 3 (r= 0.94, p-value= 10^{-23}). The correlations between the principal components of the HFC and SFC in the Subregion 2 and 4 are r= -0.3 (p-value= 0.83) and r= 0.09, (p-value= 0.56) respectively. The coherent nature of the dominant EOFs in Subregion 1 and 3 is further supported by their spatial patterns (Figures 4.4 and 4.5). The spatial structures of the dominant EOFs of HFC and SFC

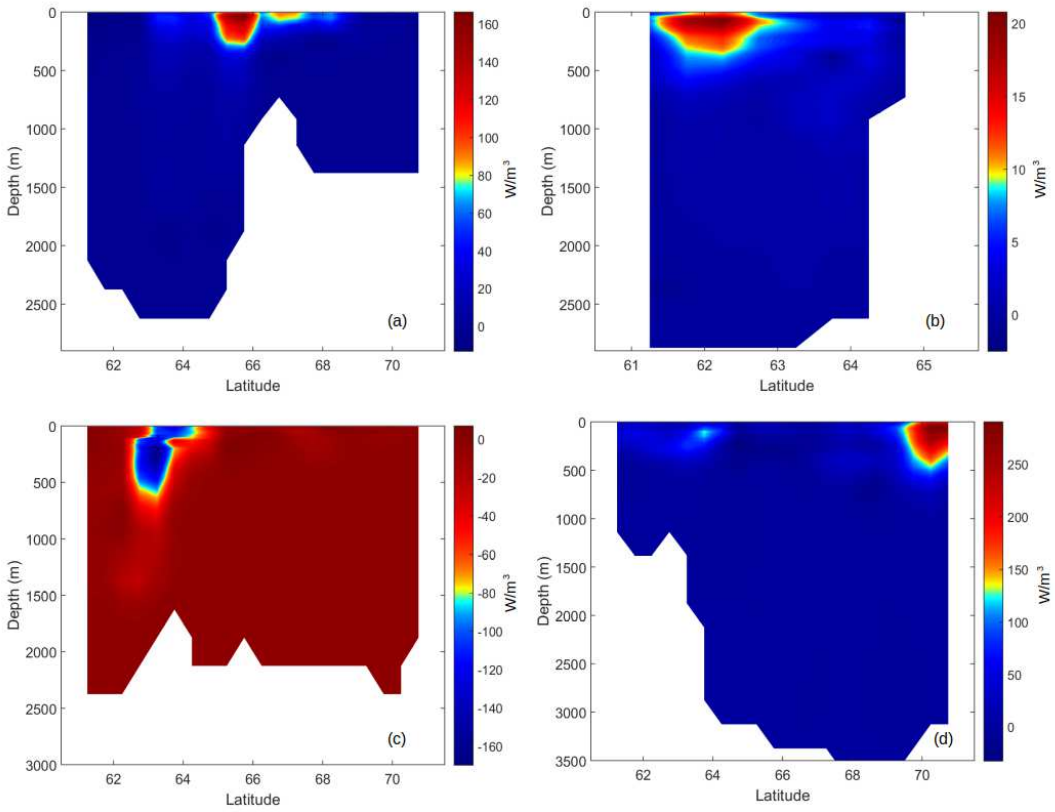

Figure 4.4: The dominant (first) EOFs calculated from the monthly mean fields of HFC for the four subregions.

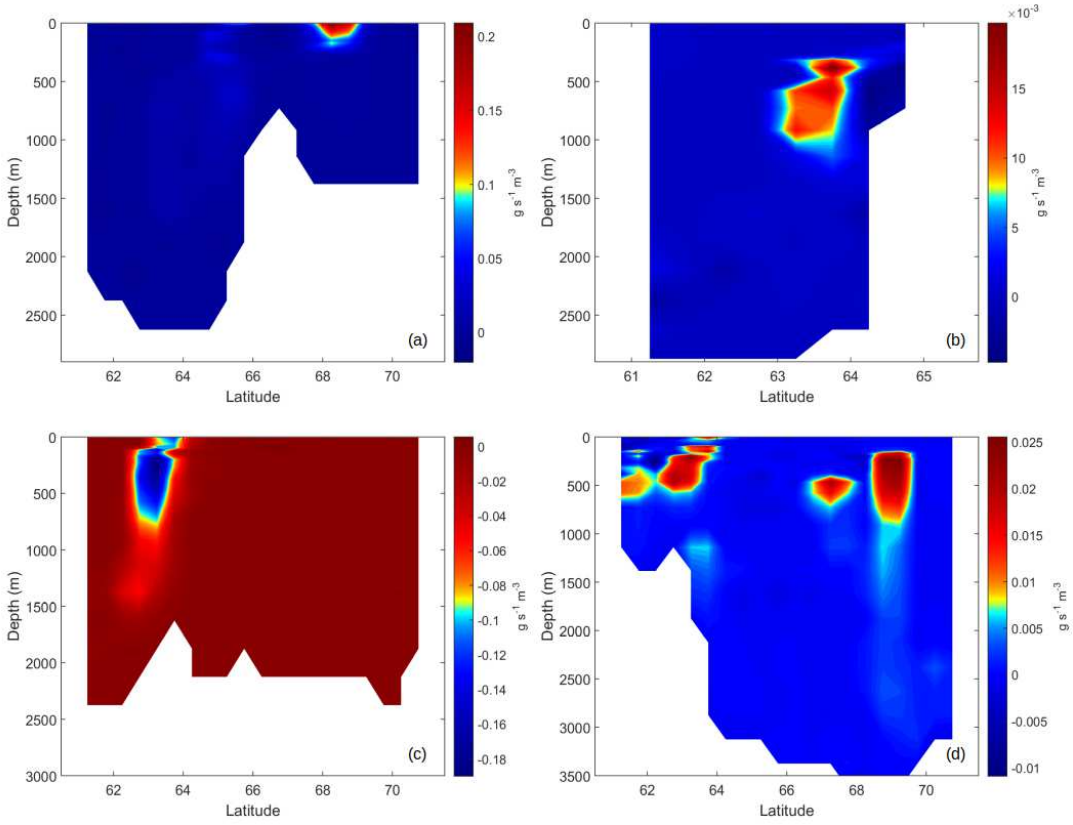

Figure 4.5: The dominant (first) EOFs calculated from the monthly mean fields of SFC for the four subregions.

in Subregion 1 and 3 (Figures 4.4a,c and 4.5a,c) constitute variations in the intensity in the main patterns of the mean HFC and SFC (Figures 4.2a,c and 4.3a,c). These are coherent in-phase oscillations throughout these subregions (i.e. the EOFs have the same sign in the subregion). The amplitude of the variations of HFC related to the dominant EOF in Subregions 1 and 3 are close and about 160 W/m^3. Similarly, the amplitude of SFC EOFs are close and about 0.2 $g/m^3/s$. We observe that there is a difference in the structure of the magnitudes of the dominant EOFs of HFC and SFC in Subregion 1. The SFC maximum in this subregion occurs not south of Denmark Strait but at about 67-68^{o}N (Figure 4.5a). The SFC variations in the surface layer of this subregion depend on the advection of salinity and transport of sea-ice. The EGC transports cold and fresh waters and sea-ice of Arctic origin along the east coast of Greenland. At 67-68^{o}N in the Subregion 1, the EGC branches into the Eastern Icelandic Current and EGC. The interannual variability and partitioning of the freshwater and sea-ice transport by these currents dominates the spatial structure of the first EOF of the SFC in this subregion. Relatively high values of the amplitude of the first EOF of SFC are observed also south of the Denmark Strait but they are less than half the size of the surface values the dominant EOF of SFC at 67-68^{o}N. As mentioned earlier there is a weak correlation between the principal components of the dominant EOFs of HFC and SFC in Subregions 2 and 4. The spatial structure of the EOFs of HFC and SFC in each of these two subregions is also different. The dominant EOFs of HFC in Subregion 2 and 4 constitute mostly surface-intensified variations Figures 4.4 b and d. The maximum of the amplitude of the HFC EOF in Subregion 2 is over the central part of the gyre in the Irminger Sea is 20 W/m^3 (Figure 4.4b). Notice that this value is about two times higher than the magnitude of

	Subregion 1	Subregion 2	Subregion 3	Subregion 4
HFC - Wind	$0.37(P < 0.01)$	$0.14(P = 0.35)$	$0.27(P < 0.075)$	$-0.04(P = 0.79)$
SFC - Wind	$0.55(P < 0.0002)$	$0.23(P = 0.12)$	$0.40(P < 0.007)$	$0.67(P < 4e-6)$
HFC - SFC	$0.65(P < 1e-6)$	$-0.03(P = 0.83)$	$0.94(P < 1e-23)$	$0.08(P = 0.58)$

Table 4.2: The correlation coefficients of the principal components of the dominant EOFs of the HFC and SFC

the mean HFC (Figure 4.2b). Similarly, the highest amplitude of the dominant EOF of HFC in the northern part of Subregion 4 is 250 W/m^3 (Figure 4.4d) is almost twice as the magnitude of mean HFC in this region(Figure 4.2d). These high amplitudes are observed in the areas of strong air-sea exchange in the central part of the subpolar gyre (Figure 4.1) in the Subregion 2 and in the Lofoten Basin in the northern part of Subregion 4. On the other hand, the EOFs of the SFC in the Subregions 2 and 4 (Figures 4.5bd) represent structures of coherent variations in the intensity of the patterns of mean SFC (Figures 4.3bd) in the surface 500 m.

Figure 4.6 shows the principal components of the EOFs of HFC (blue solid curves), of the EOFs of the SFC (red solid curves). The dashed curve shows the principal component of the dominant EOF of the wind curl over the ocean region adjacent to the GSR as a measure of wind forcing in the local region. The principal components of HFC in the Subregions 2 and 4 have weak and statistically insignificant correlations with the surface wind curl. In Subregion 2 it is r= 0.14 (p-value= 0.35) and in Subregion 4 r= -0.04 (p-value= 0.79). The principal components of SFC in these subregions have significantly higher correlations with the wind stress curl. In Subregion 2 r= 0.23 (p-value= 0.12) and in Subregion 4 r= 0.67 (p-values$< 4 \cdot 10^{-6}$).

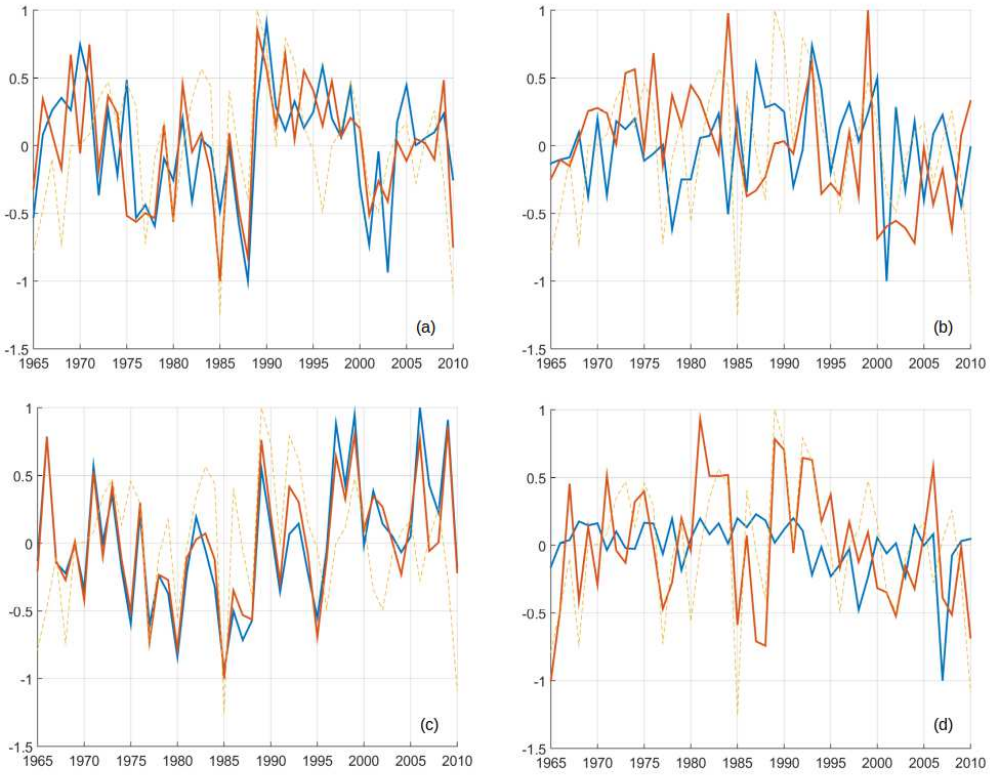

Figure 4.6: The principal components of the EOFs of HFC (blue solid curves), of the EOFs of the SFC (red solid curves). The dashed curve shows the principal component of the dominant EOF of the wind curl over the ocean region adjacent to the GSR.

The correlations of the wind stress with the principal components of the dominant EOFs of the HFC in Subregion 1 is r= 0.37 (p-value$<$ 0.01) and Subregion 3 r=0.27 (p-value $<$ 0.08). The corresponding correlation coefficients between the wind curl and principal components of SFC are r= 0.55 (p-value$<$ $2 \cdot 10^{-4}$) for Subregion 1 and r=0.40 (p-value$<$ $7 \cdot 10^{-3}$). Figures 4.6 a, c show that in general, the correspondence between the variations of the principal components of wind stress curl, HFC and SFC in these subregions are in a good agreement under strong wind curl. The long term variations in the surface wind forcing affects the Ekman pumping over the entire region and the intensity of wind-driven component of ocean circulation (see Section 2.7). One example is the interannual shift of the wind principal component from low negative in 1985 to high positive in 1990. The principal components of the HFC and SFC in subregions followed this strong variation in the surface wind forcing and both changed from low negative to high positive. We observe that the patterns of the EOFs of the HFC and SFC (Figures 4.4a,c 4.5a,c) impose variations of heat and salt advective fluxes convergence in Subregions 1 and 3 which have opposite phases. For example, during the interannual shift in the late 1980s, the HFC over the Denmark Strait increased by an amount equal to twice the amplitude of the EOF (Figures 4.4a) while the HFC over the Iceland-Faroe Ridge decreased by 1.75 times the amplitude the EOF (Figure 4.5a). Similarly, the SFC variations due to the dominant EOF modes have opposite signs in the two subregions.

4.6 Discussions

The GSR restricts the exchange of deep and intermediate waters between the North Atlantic and the Nordic Seas. The strong temperature gradient across the GSR and the impact which the ridge has on the main currents contribute to the convergence of heat and salt advective fluxes. The estimates of the HFC and SFC derived from SODA reanalysis suggest that the GSR has a strong impact in relatively narrow areas south near the Denmark Strait and Iceland-Faroe Ridge. These estimates suggest in particular that the large surface gain of heat due to the HFC south of the Denmark Strait observed in our previous study (Lundrigan & Demirov, 2019) is the surface part of patterns of high and positive HFC and SFC which extends in the water column down to depths of about 1500 m in these two areas. The values of HFC and SFC near the Denmark Strait and Iceland-Faroe Ridge exceed by an order of magnitude this characteristics in the Irminger Sea and more than twice the HFC and SFC in the Norwegian Sea.

Our analysis suggests that the variations in the dominant EOF constitutes physical modes of coherent oscillations of HFC and SFC near the Denmark Strait and Iceland-Faroe Ridge. The variability in the principal component of these modes correspond well to the local change in the intensity of the wind stress curl over the GSR in the late 1980s. Our previous study (S. Lundrigan & E. Demirov, 2012) found that this was the period of onset imbalance of lateral fluxes of heat and salt into the Nordic Seas which contributed to the decadal warming of this basin in the late 1980s and 1990s.

References

AMAP (1998). *AMAP assessment report: Arctic pollution issues*. Arctic Monitoring and Assessment Programme (AMAP), Oslo, Norway.

Barnett, T. et al. (2005). "Penetration of human-induced warming into the world's oceans". In: *Science* 309(5732), pp. 284–287.

Brambilla, E., L. Talley & P. Robbins (2008). "Subpolar Mode Water in the northeastern Atlantic: 2. Origin and transformation". In: *Journal of Geophysical Research: Oceans* 113(C4). DOI: https://doi.org/10.1029/2006JC004063.

Carton, J., G. Chepurin & L. Chen (2018). "SODA3: A new ocean climate reanalysis". In: *Journal of Climate* 31(17), pp. 6967–6983.

Carton, J. & B. Giese (2008). "A reanalysis of ocean climate using Simple Ocean Data Assimilation (SODA)". In: *Monthly Weather Review* 136(8), pp. 2999–3017.

Griffies, S.M. (2012). "Elements of the modular ocean model (MOM)". In: *GFDL Ocean Group Tech. Rep* 7, p. 620.

Isachsen, P.E., I Koszalka & JH LaCasce (2012). "Observed and modeled surface eddy heat fluxes in the eastern Nordic Seas". In: *Journal of Geophysical Research: Oceans* 117(C8). DOI: https://doi.org/10.1029/2012JC007935.

Kuhlbrodt, T. & J.M. Gregory (2012). "Ocean heat uptake and its consequences for the magnitude of sea level rise and climate change". In: *Geophysical Research Letters* 39(18).

Levitus, S. et al. (2000). "Warming of the world ocean". In: *Science* 287(5461), pp. 2225–2229.

Lundrigan, S. & E. Demirov (2012). "Long-Term Variability of Volume and Heat Transport in the Nordic Seas: A Model Study". In: *Atmosphere-Ocean* 50(2), pp. 156–168. DOI: https://doi.org/10.1080/07055900.2012.683769.

Lundrigan, S & E Demirov (2019). "Mean and Eddy-Driven Heat Advection in the Ocean Region Adjacent to the Greenland-Scotland Ridge Derived From Satellite Altimetry". In: *Journal of Geophysical Research: Oceans* 124(3), pp. 2239–2260.

Mauritzen, C. (1996a). "Production of dense overflow waters feeding the North Atlantic across the Greenland-Scotland Ridge. Part 1: Evidence for a revised circulation scheme". In: *Deep Sea Research Part I: Oceanographic Research Papers* 43(6), pp. 769–806. DOI: https://doi.org/10.1016/0967-0637(96)00037-4.

Mauritzen, C. (1996b). "Production of dense overflow waters feeding the North Atlantic across the Greenland-Scotland Ridge. Part 2: An inverse model". In: *Deep Sea Research Part I: Oceanographic Research Papers* 43(6), pp. 807–835. DOI: 10.1016/0967-0637(96)00038-6..

McCartney, M. & L. Talley (1982). "The subpolar mode water of the North Atlantic Ocean". In: *Journal of Physical Oceanography* 12(11), pp. 1169–1188. DOI: https://doi.org/10.1175/1520-0485(1982)012<1169:TSMWOT>2.0.CO;2.

Meehl, G. et al. (2011). "Model-based evidence of deep-ocean heat uptake during surface-temperature hiatus periods". In: *Nature Climate Change* 1(7), p. 360.

Myers, P., N. Kulan & M. Ribergaard (2007). "Irminger water variability in the West Greenland Current". In: *Geophysical Research Letters* 34(17). DOI: https://doi.org/10.1029/2007GL030419.

Roberts, C.D. et al. (2016). "On the drivers and predictability of seasonal-to-interannual variations in regional sea level". In: *Journal of Climate* 29(21), pp. 7565–7585.

Roberts, C. et al. (2017). "Surface flux and ocean heat transport convergence contributions to seasonal and interannual variations of ocean heat content". In: *Journal of Geophysical Research: Oceans* 122(1), pp. 726–744.

Rudels, B., E. Fahrbach, et al. (2002). "The East Greenland Current and its contribution to the Denmark Strait overflow". In: *ICES Journal of Marine Science* 59(6), pp. 1133–1154. DOI: https://doi.org/10.1006/jmsc.2002.1284.

Stocker, T. (2014). *Climate change 2013: the physical science basis: Working Group I contribution to the Fifth assessment report of the Intergovernmental Panel on Climate Change*. Cambridge University Press.

Straneo, F. (2006). "Heat and freshwater transport through the central Labrador Sea". In: *Journal of Physical Oceanography* 36(4), pp. 606–628. DOI: https://doi.org/10.1175/JPO2875.1.

Zhu, J & E Demirov (2011). "On the mechanism of interannual variability of the Irminger Water in the Labrador Sea". In: *Journal of Geophysical Research: Oceans* 116(C3). DOI: https://doi.org/10.1029/2009JC005677.

Chapter 5

Conclusions

5.1 Summary

The ocean transport through the GSR is essential for maintaining the present-day exchange of heat and freshwater between the Arctic Mediterranean and the North Atlantic Ocean. Understanding this transport is crucial for improving our understanding of the climate of the Arctic and Subarctic. The main objective of this thesis is to quantify the characteristics of advective heat transport in the ocean region adjacent to the GSR. The study consists of three Sub-projects.

Sub-project 1, presented in Chapter 2, focuses on a model study of interannual and decadal variability in the Nordic Seas. The advective heat transport though the GSR and its impact on the heat budget of the Nordic Seas are estimated based on fifty years of ensemble simulations forced with the reanalysis of the National Centers for Environmental Prediction (NCEP). The goal of the model data analysis is to understand the role of the advection of heat through the GSR in driving the interannual

variability of the Nordic Seas observed over the last fifty years.

Sub-project 2, presented in Chapter 3, provides observational estimates of surface mean and eddy-induced heat fluxes derived from satellite and in-situ data. The goal of this study is to identify the spatial patterns of the heat flux convergence (HFC) over the region adjacent to the GSR and the contributions of mean advection and eddy-induced transport to the HFC.

Sub-project 3, presented in Chapter 4, focuses on the vertical structure of convergence of the advective fluxes of heat and salt. The primary goal of this sub-project is to find the "fingerprints" in the surface patterns of the heat advection convergence found in Sub-project 2. The heat and salt fluxes in this sub-project are derived from the SODA (Simple Ocean Data Analysis) reanalysis.

5.2 Main conclusions

The analysis of ensemble model simulations in Sub-project 1 focuses on two events in the interannual and interdecadal variability of the Nordic Seas during the past fifty years. The first one is the Great Salinity Anomaly in the 1960s and early 1970s. The second one is the warming of the Arctic and Subarctic oceans in the late 1980s. The results from model simulations demonstrate that the increase in the transport of fresh and cold waters through Fram Strait in the 1960s was concurrent with a reduction in the meridional water exchange over the GSR. The resulting imbalance in salinity and heat fluxes through the strait and over the ridge also contributed to the freshening of the water masses of the Nordic Seas and intensified the Great Salinity Anomaly in the Nordic Seas. The model results also demonstrated that in the late 1980s, the

AW transport over the GSR was stronger than usual while the exchange through Fram Strait was close to normal. The related imbalance in the lateral heat fluxes through the strait and over the ridge warmed the Nordic Seas and caused an increase in the temperature of the AW inflow to the Arctic Ocean in the late 1980s (i.e., about a decade earlier than the warming of the source of the AW in the subpolar North Atlantic Ocean).

The results from the analysis of satellite and in-situ observations in Sub-project 2 demonstrated that heat advection by the mean flow in the surface layer of the ocean region adjacent to the GSR is zonally asymmetric with higher magnitude in the western part of the region. This asymmetry is associated with a large magnitude mean heat advection in an area adjacent to the Denmark Strait. The advection of heat is high and positive south of the strait and low and negative north of it. We suggest that this heat advection impacts the local budgets of heat and potential energy of the mean flow in the surface layer. The satellite altimeter observations are used to identify and study the characteristics of mesoscale eddies in the ocean region adjacent to the GSR. The radius, lifetime, and paths of propagation, are assessed. About 70% of the eddies are observed in the eastern part of the studied region. The eddy-induced heat transport by warm mesoscale eddies in the Norwegian Sea was found to be about two-and-a-half times larger than the mean advection by the Norwegian Atlantic Current.

The analysis of SODA data demonstrates that model reanalysis represents the large-scale patterns of surface heat convergence found in the observational estimates (HFC) correctly in the ocean region adjacent to the GSR found in Sub-project 2. The SODA based results show also that the high values of the HFC over the Denmark

Strait are part of a pattern of intensified mean HFC and convergence of advective fluxes of salinity (SFC) in the surface 1500 m ocean layer. A similar pattern of high positive SFC and HFC is observed at depths between 500 m and 1500 m over the Iceland-Faroe Ridge. The EOF analysis of the HFC and SFC shows that the variability of the centers of high HFC and SFC over the Denmark Strait and Iceland-Faroe Ridge is dominated by physical modes of coherent variations in the SFC and HFC in these regions. In particular, these modes caused an intensification of the heat and salt exchange through the GSR during the decadal shift in the transport of heat through the GSR in the late 1980s found in Sub-project 1. The method of this study is based on using surface observations and simulations from coarse resolution and eddy-permitting ocean models. By their nature, these data do not resolve the dynamics in the overflow regions in the GSR. The results focus mostly on the heat fluxes in the surface and intermediate ocean layers (Chapters 4,5) and the long-term variability of integral heat and salt transport through the GSR (Chapter 3). While the results are robust and consistent in both observations and ocean simulations, they do not provide any insight into the role of the deepwater overflow through the GSR on the meridional heat and salt transport.

5.3 Ideas for future research

The results presented in the thesis raise questions about the physical processes of the exchange through the GSR. The scales of these processes range in a broad interval, from the fine-scale, sub-mesoscale and mesoscale to the large-scale ocean circulation.

What are the physical processes that govern the observed patterns of HFC and

SFC? What is the relative importance of mean advection, mesoscale eddies, and submesoscale events on this transport?

How significant is the global impact of the patterns of high HFC and SFC over the Denmark Strait and Iceland-Faroe Ridge on the meridional transport of heat and freshwater in the Arctic and Subarctic?

How significant are the local impacts of observed patterns of HFC and SFC and their variability on the properties of water mass characteristics in the ocean region adjacent to the GSR?

The model simulations used in the thesis have an insufficient resolution to address these questions. The satellite observations used to estimate HFC provide information only for the surface layer of the ocean. Therefore, more observations and improved models are needed to address these questions. The most recent advances in ocean observations and modeling provide the foundation for addressing these research questions.

- The technological advance in the ocean observing system provides an unprecedented opportunity to obtain high-quality in-situ subsurface observations. The moorings and gliders deployed by international programs like OSNAP, VITALS, and OFI provide valuable information about the heat transport in the Arctic and Subarctic.

- Over the past two decades, there was an essential development in the methods of numerical modelling of ocean circulation. Present-day ocean models have enhanced capabilities in simulating the ocean dynamics over complex topography with a resolution of the order of kilometres. The present-day ocean models, in combination with observations, provide an opportunity to study the interaction of the large scale transport with local HFC and SFC over the GSR.

Bibliography

Abernathey, R. & J Marshall (2013). "Global surface eddy diffusivities derived from satellite altimetry". In: *Journal of Geophysical Research: Oceans* 118(2), pp. 901–916. DOI: https://doi.org/10.1002/jgrc.20066.

Aksenov, Y. et al. (2010). "The North Atlantic inflow to the Arctic Ocean: High-resolution model study". In: *Journal of Marine Systems* 79(1-2), pp. 1–22.

AMAP (1998). *AMAP assessment report: Arctic pollution issues*. Arctic Monitoring and Assessment Programme (AMAP), Oslo, Norway.

Antonov, J. et al. (2005). "World Ocean Atlas 2005, Volume 2:Salinity". In: *NOAA Atlas NESDIS 62*. Ed. by S. Levitus. U.S. Government Printing Office, Washington, D.C., 182p.

AVISO (2011). *AVISO (Archiving and Validation and Interpretation of Satellite Oceanographic data)*. Tech. rep. The altimeter products were produced by Ssalto/Duacs and distributed by Aviso, with support from Cnes.

AVISO (2013). *AVISO (Archiving and Validation and Interpretation of Satellite Oceanographic data)*. Tech. rep. GFO.

B.Bernard et al. (2006). "Impact of partial steps amd momentum advectoin schemes in a global ocean ciruclation model at eddy-permitting resolution." In: *Ocean Dynamics* 56, pp. 543–567.

Barnett, T. et al. (2005). "Penetration of human-induced warming into the world's oceans". In: *Science* 309(5732), pp. 284–287.

Beckmann, A & R Döscher (1997). "A method for improved representation of dense water spreading over topography in geopotential-coordinate models". In: *Journal of Physical Oceanography* 27(4), pp. 581–591.

Belkin, I. et al. (1998). "Great Salinity Anomalies". In: *Progress in Oceanography* 41, pp. 1–68.

Bersch, M. (1995). "On the circulation of the northeastern North Atlantic". In: *Deep Sea Research Part I: Oceanographic Research Papers* 42(9), pp. 1583–1607.

Blanke, B. & P. Delecluse (1993). "Variability of the tropical Atlantic ocean simulated by a general circulation model with two different mixed layer physics." In: *J. Phys. Oceanogr.* 23, pp. 1363–1388.

Blindheim, J. & S Osterhus (2005). "The Nordic Seas, main oceanographic features". In: *Geophysical Monograph-American Geophysical Union* 158, p. 11. DOI: https://doi.org/10.1029/158GM03.

Brambilla, E., L. Talley & P. Robbins (2008). "Subpolar Mode Water in the northeastern Atlantic: 2. Origin and transformation". In: *Journal of Geophysical Research: Oceans* 113(C4). DOI: https://doi.org/10.1029/2006JC004063.

Brath, M. et al. (2010). "Altimeter-based estimates of eddy variability and eddy transports in the subpolar North Atlantic". In: *Marine Geodesy* 33(S1), pp. 472–503.

Burchard, H. & J. Beckers (2004). "Non-uniform adaptive vertical grids in one-dimensional numerical ocean models". In: *Ocean Modelling* 6(1), pp. 51–81.

Carton, J., G. Chepurin & L. Chen (2018). "SODA3: A new ocean climate reanalysis". In: *Journal of Climate* 31(17), pp. 6967–6983.

Carton, J. & B. Giese (2008). "A reanalysis of ocean climate using Simple Ocean Data Assimilation (SODA)". In: *Monthly Weather Review* 136(8), pp. 2999–3017.

Chaigneau, A. et al. (2011). "Vertical structure of mesoscale eddies in the eastern South Pacific Ocean: A composite analysis from altimetry and Argo profiling floats". In: *Journal of Geophysical Research: Oceans* 116(C11). DOI: https://doi.org/10.1029/2011JC007134.

Chelton, D., R. DeSzoeke, et al. (1998). "Geographical variability of the first baroclinic Rossby radius of deformation". In: *Journal of Physical Oceanography* 28(3), pp. 433–460.

Chelton, D., M. Schlax & R. Samelson (2011). "Global observations of nonlinear mesoscale eddies". In: *Progress in Oceanography* 91(2), pp. 167–216. DOI: https://doi.org/10.1016/j.pocean.2011.01.002.

Chinn, B. & S. Gille (2007). "Estimating eddy heat flux from float data in the North Atlantic: The impact of temporal sampling interval". In: *Journal of Atmospheric and Oceanic Technology* 24(5), pp. 923–934. DOI: https://doi.org/10.1175/JTECH2057.1.

Coachman, L.K. & K. Aagaard (1974). "Physical oceanography of Arctic and subarctic seas". In: *Marine geology and oceanography of the Arctic seas*. Springer, pp. 1–72.

Conger, AM et al. (2009). "GFO and JASON Altimeter Engineering Assessment Report. Update: GFO-Acceptance to End of Mission on October 22, 2008, JASON-Acceptance to September 29, 2008". In:

Dickson, B., J. Meincke & P. Rhines (2008). "Arctic-Subarctic ocean fluxes: Defining the role of the Northern Seas in climate. A general introduction". In: *Arctic-Subarctic Ocean Fluxes - Defining the role of the northern seas in climate*. Ed. by R.R. Dickson, J. Meincke & P. Rhines. Springer, pp. 1–14.

Dickson, R.R. & J. Brown (1994). "The production of North Atlantic Deep Water: sources, rates, and pathways". In: *Journal of Geophysical Research: Oceans* 99(C6), pp. 12319–12341. DOI: https://doi.org/10.1029/94JC00530.

Dickson, R.R., J.J. Osborn, et al. (2000). "The Arctic response to the North Atlantic Oscillation". In: *J. Clim.* 15, pp. 2671–2696.

Dickson, R. et al. (1988). "The Great Salinity Anomaly in the northern North Atlantic". In: *Progress in Oceanography* 20(2), pp. 103–151.

Dong, C. et al. (2014). "Global heat and salt transports by eddy movement". In: *Nature communications* 5, p. 3294.

Drange, H. et al. (2005). "The Nordic seas: an overview". In: *GEOPHYSICAL MONOGRAPH-AMERICAN GEOPHYSICAL UNION* 158, p. 1.

Dussurget, R. et al. (2011). "Fine resolution altimetry data for a regional application in the Bay of Biscay". In: *Marine Geodesy* 34(3-4), pp. 447–476. DOI: https://doi.org/10.1080/01490419.2011.584835.

Eden, C. (2010). "Anisotropic rotational and isotropic residual isopycnal mesoscale eddy fluxes". In: *Journal of Physical Oceanography* 40(11), pp. 2511–2524. DOI: https://doi.org/10.1175/2010JPO4397.1.

Eldevik, T. et al. (2009). "Observed sources and variability of Nordic seas overflow". In: *Nature Geoscience* 2(6), p. 406.

Fan, X. et al. (2013). "Observations of Irminger Sea anticyclonic eddies". In: *Journal of Physical Oceanography* 43(4), pp. 805–823. DOI: https://doi.org/10.1175/JPO-D-11-0155.1.

Fichefet, T. & M.A. Maqueda (1999). "Modelling the influence of snow accumulation and snow-ice formation on the seasonal cycle of the Antarctic sea-ice cover". In: *Climate Dynamics* 15(4), pp. 251–268.

Gascard, J. & K. Mork (2008). "Climatic importance of large-scale and mesoscale circulation in the Lofoten Basin deduced from Lagrangian observations". In: *Arctic–Subarctic Ocean Fluxes*. Springer, pp. 131–143.

Gent, P.R. & J.C. McWilliams (1990). "Isopycnal mixing in ocean circulation models". In: *J. Phys. Oceanogr* 20, pp. 150–155.

Gill, A. (1982). *Atmosphere—ocean dynamics*. Elsevier.

Glessmer, M. et al. (2014). "Atlantic origin of observed and modelled freshwater anomalies in the Nordic Seas". In: *Nature Geoscience* 7(11), p. 801. DOI: https://doi.org/10.1038/ngeo2259.

Griffies, S.M. (2012). "Elements of the modular ocean model (MOM)". In: *GFDL Ocean Group Tech. Rep* 7, p. 620.

Häkkinen, S. & C. Geiger (2000). "Simulated low-frequency modes of circulation in the Arctic Ocean". In: *Journal of Geophysical Research: Oceans* 105(C3), pp. 6549–6564.

Hakkinen, S. & P.B. Rhines (2004). "Decline of subpolar North Atlantic circulation during the 1990s". In: *Science* 304(5670), pp. 555–559.

Hanawa, K. & L. Talley (2001). ".4 Mode waters". In: *International Geophysics*. Vol. 77. Elsevier, pp. 373–386. DOI: https://doi.org/10.1016/S0074-6142(01)80129-7.

Hansen, B. & S Østerhus (2000). "North atlantic–nordic seas exchanges". In: *Progress in oceanography* 45(2), pp. 109–208. DOI: https://doi.org/10.1016/S0079-6611(99)00052-X.

Hansen, B., S. Osterhus, et al. (2008). "The Inflow of Atlantic Water, Heat and Salt to the Nordic Seas". In: *Arctic-Subarctic Ocean Fluxes - Defining the role of the northern seas in climate*. Ed. by R.R. Dickson, J. Meincke & P. Rhines. Springer, pp. 15–43.

Hátún, H., C. Eriksen & P.B Rhines (2007). "Buoyant eddies entering the Labrador Sea observed with gliders and altimetry". In: *Journal of Physical Oceanography* 37(12), pp. 2838–2854. DOI: https://doi.org/10.1175/2007JPO3567.1.

Haugan, P.M. et al. (1991). "Modeled and observed mesoscale circulation and wave current refraction during the 1988 Norwegian continental shelf experiment". In: *Geophysical Research* 96, pp. 10487–10506.

Hibler III, W.D. (July 1979). "A Dynamic Thermodynamic Sea Ice Model". In: *Journal of Physical Oceanography* 9, pp. 815–846.

Hilmer, M. & T. Jung (2000). "Evidence for a recent change in the link between the North Atlantic Oscillation and Arctic sea ice export". In: *Geophysical Research Letters* 27(7), pp. 989–992.

Hurlburt, H. et al. (2008). "Steering of upper ocean currents and fronts by the topographically constrained abyssal circulation". In: *Dynamics of Atmospheres and*

Oceans 45(3-4), pp. 102–134. DOI: https://doi.org/10.1016/j.dynatmoce.2008.06.003.

Ikeda, M et al. (1989). "A process study of mesoscale meanders and eddies in the Norwegian Coastal Current". In: *Journal of Physical Oceanography* 19(1), pp. 20–35. DOI: https://doi.org/10.1175/1520-0485.

Ince, E. et al. (2019). "ICGEM–15 years of successful collection and distribution of global gravitational models, associated services, and future plans". In: *Earth System Science Data* 11(2), pp. 647–674.

Isachsen, P.E., I Koszalka & JH LaCasce (2012). "Observed and modeled surface eddy heat fluxes in the eastern Nordic Seas". In: *Journal of Geophysical Research: Oceans* 117(C8). DOI: https://doi.org/10.1029/2012JC007935.

Isachsen, P.E., J.H LaCasce, et al. (2003). "Wind-Driven Variability of the Large-Scale Recirculating Flow in the Nordic Seas and Arctic Ocean". In: *Phys. Oceanography* 33, pp. 2535–2550.

Jackett, DR & TJ McDougall (1995). "Stabilization of hydrographic data". In: *J. Atmos. Oceanic Technol* 12, pp. 381–389.

Johannessen, O.M., K. Lygre & T. Eldevik (2005). "Convective chimneys and plumes in the Northern Greenland Sea". In:

Johnson, G. & K. McTaggart (2010). "Equatorial Pacific 13 C water eddies in the eastern subtropical South Pacific Ocean". In: *Journal of Physical Oceanography* 40(1), pp. 226–236. DOI: https://doi.org/10.1175/2009JPO4287.1.

Karcher, M. et al. (2003). "Arctic warming: Evolution and spreading of the 1990s warm event in the Nordic seas and the Arctic Ocean". In: *Journal of Geophysical Research: Oceans* 108(C2).

Karimova, S. (2017). "Performance of gridded and along-track altimetry products in eddy manifestation in the western mediterranean". In: *2017 IEEE International Geoscience and Remote Sensing Symposium (IGARSS)*. IEEE, pp. 2991–2998.

Khatiwala, S., P. Schlosser & M. Visbeck (Feb. 2002). "Rates and Mechanisms of Water Mass Transformation in the Labrador Sea as Inferred from Tracer Observations". In: *Journal of Physical Oceanography* 32, pp. 666–686.

Kuhlbrodt, T. & J.M. Gregory (2012). "Ocean heat uptake and its consequences for the magnitude of sea level rise and climate change". In: *Geophysical Research Letters* 39(18).

Latarius, K. & D. Quadfasel (2010). "Seasonal to inter-annual variability of temperature and salinity in the Greenland Sea Gyre: heat and freshwater budgets". In: *Tellus A: Dynamic Meteorology and Oceanography* 62(4), pp. 497–515.

Levitus, S. et al. (2000). "Warming of the world ocean". In: *Science* 287(5461), pp. 2225–2229.

Lilly, J.M. (2002). "Observations of the Labrador Sea eddy field". PhD thesis. University of Washington.

Lilly, J.M. et al. (2003). "Observations of the Labrador Sea eddy field". In: *Progress in Oceanography* 59(1), pp. 75–176. DOI: https://doi.org/10.1016/j.pocean.2003.08.013.

Lohmann, K., H. Drange & M. Bentsen (2008). "Response of the North Atlantic subpolar gyre to persistent North Atlantic oscillation like forcing." In: *Clim Dyn* 32, pp. 273–285.

Lundrigan, S. (2010). "A Model Study of Interannual and Decadal Variability of the Arctic and Sub-Arctic Oceans". MSc. Newfoundland: Memorial University of Newfoundland.

Lundrigan, S. & E. Demirov (2012). "Long-Term Variability of Volume and Heat Transport in the Nordic Seas: A Model Study". In: *Atmosphere-Ocean* 50(2), pp. 156–168. DOI: https://doi.org/10.1080/07055900.2012.683769.

Lundrigan, S & E Demirov (2019). "Mean and Eddy-Driven Heat Advection in the Ocean Region Adjacent to the Greenland-Scotland Ridge Derived From Satellite Altimetry". In: *Journal of Geophysical Research: Oceans* 124(3), pp. 2239–2260.

Madec, G. (2008). *NEMO ocean engine: version 3.1.* Laboratoire d'Oceanographie et du Climat: Experimentation et Approches Numeriques.

Marsh, R. et al. (2008). "Mechanisms for recent warming of the North Atlantic: Insights gained with an eddy-permitting model". In: *Journal of Geophysical Research,* 113. doi:10.1029/2007JC004096.

Marshall, J. & G. Shutts (1981). "A note on rotational and divergent eddy fluxes". In: *Journal of Physical Oceanography* 11(12), pp. 1677–1680. DOI: https://doi.org/10.1175/1520-0485.

Mauritzen, C. (1996a). "Production of dense overflow waters feeding the North Atlantic across the Greenland-Scotland Ridge. Part 1: Evidence for a revised circulation scheme". In: *Deep Sea Research Part I: Oceanographic Research Papers* 43(6), pp. 769–806. DOI: https://doi.org/10.1016/0967-0637(96)00037-4.

Mauritzen, C. (1996b). "Production of dense overflow waters feeding the North Atlantic across the Greenland-Scotland Ridge. Part 2: An inverse model". In: *Deep*

Sea Research Part I: Oceanographic Research Papers 43(6), pp. 807–835. DOI: 10.1016/0967-0637(96)00038-6..

McCartney, M. & L. Talley (1982). "The subpolar mode water of the North Atlantic Ocean". In: *Journal of Physical Oceanography* 12(11), pp. 1169–1188. DOI: https://doi.org/10.1175/1520-0485(1982)012<1169:TSMWOT>2.0.CO;2.

Meehl, G. et al. (2011). "Model-based evidence of deep-ocean heat uptake during surface-temperature hiatus periods". In: *Nature Climate Change* 1(7), p. 360.

Meincke, J, B Rudels & HJ Friedrich (1997). "The Arctic Ocean–Nordic Seas thermohaline system". In: *ICES Journal of Marine Science* 54(3), pp. 283–299.

Merryfield, W.J., G. Holloway & A. E. Gargett (June 1999). "A Global Ocean Model with Double-Diffusive Mixing". In: *Journal of Physical Oceanography* 29, pp. 1124–1142.

Mohn, H. (1887). *Den Norske Nordhavsekspedition 1876-1878. Temperatur og Stromingar*. Version Bd II. Christiania, Norway: Nordhavets Dybder.

Mork, K. & Ø. Skagseth (2010). "A quantitative description of the Norwegian Atlantic Current by combining altimetry and hydrography". In: *Ocean Science* 6(4), pp. 901–911. DOI: https://doi.org/10.5194/os-6-901-2010.

Mork, M. (1981). "Circulation phenomena and frontal dynamics of the Norwegian Coastal Current". In: *Philosophical Transactions of the Royal Society of London A: Mathematical, Physical and Engineering Sciences* 302(1472), pp. 635–647. DOI: 10.1098/rsta.1981.0188.

Muench, R.D. et al. (1992). "Winter oceanographic conditions in the Fram Strait Yermak Plateau region". In: *Journal of Geophysical Research* 97, pp. 3469–3483.

Myers, P., N. Kulan & M. Ribergaard (2007). "Irminger water variability in the West Greenland Current". In: *Geophysical Research Letters* 34(17). DOI: https://doi.org/10.1029/2007GL030419.

Mysak, L., D. Manak & R. Marsden (1990). "Sea-ice anomalies observed in the Greenland and Labrador Seas during 1901-1984 and their relation to an interdecadal Arctic climate cycle". In: *Climate Dynamics* 5(2), pp. 111–133.

Mysak, L. & S. Power (1992). "Sea-ice anomalies in the western Arctic and Greenland-Iceland Sea and their relation to an interdecadal climate cycle." In: *Climatological Bulletin* 26(3), pp. 147–176.

NEMO (Nucleus for European Modelling of the Ocean) (Nov. 2011). *Meshmask grid*. http://www.nemo-ocean.eu/About-NEMO/Gallery/Meshmask-grid.

NOAA & NODC (2007). *Operational oceanography group: Global ARGO data*. Tech. rep. date of access: July 2012. National Oceanic Atmospheric Administration.

Nurser, AJG & S Bacon (2014). "The rossby radius in the Arctic Ocean". In: *Ocean Science* 10(6), pp. 967–975.

Orvik, K. & P. Niiler (2002). "Major pathways of Atlantic waters in the North Atlantic and Nordic Seas towards Arctic." In: *Geophys. Res. Lett.* 29(19), doi:10, 1029/2002GL01502.

Osborn, T. & C. Cox (1972). "Oceanic fine structure". In: *Geophysical & Astrophysical Fluid Dynamics* 3(1), pp. 321–345. DOI: https://doi.org/10.1080/03091927208236085.

Østerhus, S. & T. Gammelsrød (1999). "The abyss of the Nordic Seas is warming". In: *Journal of Climate* 12(11), pp. 3297–3304.

Pawlowicz, R. et al. (1995). "Thermal evolution of the Greenland Sea Gyre in 1988–1989". In: *Journal of Geophysical Research: Oceans* 100(C3), pp. 4727–4750.

Pickart, R., D. Torres & P. Fratantoni (2005). "The east Greenland spill jet". In: *Journal of Physical Oceanography* 35(6), pp. 1037–1053. DOI: https://doi.org/10.1175/JPO2734.1.

Polyakov, I., G. Alekseev, et al. (2004). "Variability of the Intermediate Atlantic Water of the Arctic Ocean over the Last 100 years." In: *Journal of Climate* 17(23). doi:10.1175/JCLI-3224.1, pp. 4485–4497.

Polyakov, I., A. Beszczynska, et al. (2005). "One more step toward a warmer Arctic". In: *G. Res. Lett.* 32(L17605). doi:10.1029/2005GL023740.

Quadfasel, D. et al. (1991). "Warming in the Arctic". In: *Nature*.

Reynolds, R. et al. (2007). "Daily high-resolution-blended analyses for sea surface temperature". In: *Journal of Climate* 20(22), pp. 5473–5496. DOI: https://doi.org/10.1175/2007JCLI1824.1.

Rhein, M. (1996). "Convection in the Greenland Sea, 1982–1993". In: *Journal of Geophysical Research: Oceans* 101(C8), pp. 18183–18192.

Rhines, P., S. Häkkinen & S. Josey (2008). "Is Oceanic Heat Transport Significant in the Climate System". In: *Arctic-Subarctic Ocean Fluxes - Defining the role of the northern seas in climate*. Ed. by R.R. Dickson, J. Meincke & P. Rhines. Springer, pp. 87–110.

Roberts, C.D. et al. (2016). "On the drivers and predictability of seasonal-to-interannual variations in regional sea level". In: *Journal of Climate* 29(21), pp. 7565–7585.

Roberts, C. et al. (2017). "Surface flux and ocean heat transport convergence contributions to seasonal and interannual variations of ocean heat content". In: *Journal of Geophysical Research: Oceans* 122(1), pp. 726–744.

Rossby, T., M.D. Prater & H. Søiland (2009). "Pathways of inflow and dispersion of warm waters in the Nordic seas." In: *Geo. Phys. Res.* 114. doi:10.1029/2008JC005073.

Rudels, B., E. Fahrbach, et al. (2002). "The East Greenland Current and its contribution to the Denmark Strait overflow". In: *ICES Journal of Marine Science* 59(6), pp. 1133–1154. DOI: https://doi.org/10.1006/jmsc.2002.1284.

Rudels, B., H. Friedrich & D. Quadfasel (1999). "The Arctic circumpolar boundary current". In: *Deep Sea Research Part II: Topical Studies in Oceanography* 46(6-7), pp. 1023–1062. DOI: https://doi.org/10.1016/S0967-0645(99)00015-6.

Rudels, B., D. Quadfasel, et al. (1989). "Greenland Sea convection in the winter of 1987–1988". In: *Journal of Geophysical Research: Oceans* 94(C3), pp. 3223–3227.

Schauer, U. et al. (2008). "Variation of Measured Heat Flow Through the Fram Strait Between 1997 and 2006." In: *Arctic-Subarctic Ocean Fluxes - Defining the role of the northern seas in climate*. Ed. by R. R. Dickson, J. Meincke & P. Rhines. Springer, pp. 65–85.

Schlichtholz, P. (2011). "Influence of oceanic heat variability on sea ice anomalies in the Nordic Seas". In: *Geophys. Res. Lett.* 38, doi:10.1029/2010GL045894.

Serreze, M. et al. (2006). "The large-scale freshwater cycle of the Arctic". In: *Journal of Geophysical Research: Oceans* 111(C11). DOI: https://doi.org/10.1029/2005JC003424.

Skagseth, O et al. (2008). "Arctic-Subarctic Ocean Fluxes - Defining the role of the northern seas in climate". In: Springer. Chap. Volume and Heat Transports to the Arctic Ocean.

Stammer, D. & C. Dieterich (1999). "Space-borne measurements of the time-dependent geostrophic ocean flow field". In: *Journal of Atmospheric and Oceanic Technology* 16(9), pp. 1198–1207. DOI: https://doi.org/10.1175/1520-0426(1999)016<1198:SBMOTT>2.0.CO;2.

Stocker, T. (2014). *Climate change 2013: the physical science basis: Working Group I contribution to the Fifth assessment report of the Intergovernmental Panel on Climate Change*. Cambridge University Press.

Straneo, F. (2006). "Heat and freshwater transport through the central Labrador Sea". In: *Journal of Physical Oceanography* 36(4), pp. 606–628. DOI: https://doi.org/10.1175/JPO2875.1.

Straneo, F. et al. (2009). "Did changes in the Subpolar North Atlantic trigger the recent mass loss from the Greenland Ice Sheet?" In: *US Clivar Variations Newsletter* 7, pp. 1–4.

T.Fichefet & M.A.Morales Maqueda (1997). "Sensitivity of a global sea ice model to the treatment of ice thermodynamics and dynamics." In: *J. Geophys. Res.* 102, pp. 12609–12646.

Tereshchenko, V. (1997). "Seasonal and year-to-year variation in temperature and salnity of the main currents in Kola section in the Barents SeaHistorical data on water temperature in the 0-200m layer in the Kola section in the Barents Sea (1". In: *PINRO*. PINRO Press, 71p.

Thompson, K.R. et al. (2006). "A simple method for reducing seasonal bias and drift in eddy resolving ocean models". In: *Ocean Model*, pp. 122–138.

Timmermann, R. et al. (2005). "On the representation of high latitude processes in the ORCA-LIM global coupled sea ice–ocean model". In: *Ocean Modelling* 8(1-2), pp. 175–201.

Tran, N et al. (2002). "Assessment of the cycle-to-cycle noise level of the Geosat Follow-On, TOPEX, and Poseidon altimeters". In: *Journal of Atmospheric and Oceanic Technology* 19(12), pp. 2095–2107. DOI: https://doi.org/10.1175/1520-0426(2002)019<2095:AOTCTC>2.0.CO;2.

Våge, K. et al. (2011). "The Irminger gyre: circulation, convection, and interannual variability". In: *Deep Sea Research Part I: Oceanographic Research Papers* 58(5), pp. 590–614. DOI: https://doi.org/10.1016/j.dsr.2011.03.001.

Vallis, G.K. & L. Lam (1996). "From Laminar Flow to Turbulence". In: *An introduction to nonlinear physics*, pp. 308–357.

Veron, AJ et al. (1999). "Stable lead isotopic ratios trace thermohaline circulation in the subarctic North Atlantic". In: *Deep Sea Research Part II: Topical Studies in Oceanography* 46(5), pp. 919–935. DOI: https://doi.org/10.1016/S0967-0645(99)00009-0.

Voet, G. et al. (2010). "The mid-depth circulation of the Nordic seas derived from profiling float observations". In: *Tellus*(62A). doi:10.1111/j.1600-0870.2010.00444.x, pp. 516–529.

Wunsch, C. (1999). "Where do ocean eddy heat fluxes matter?" In: *Journal of Geophysical Research: Oceans* 104(C6), pp. 13235–13249. DOI: https://doi.org/10.1029/1999JC900062.

Yashayaev, I. (2007). "Hydrographic changes in the Labrador Sea, 1960-2005". In: *Prog. Oceanogr.* 73(3-4), pp. 242–276.

Yashayaev, I. & D. Seidov (2015). "The role of the Atlantic Water in multidecadal ocean variability in the Nordic and Barents Seas". In: *Progress in Oceanography* 132, pp. 68–127. DOI: https://doi.org/10.1016/j.pocean.2014.11.009.

Zhang, J., D A. Rothrock & M. Steele (1998). "Warming of the Arctic Ocean by a strengthened Atlantic inflow: Model results". In: *Geophysical Research Letters* 25(10), pp. 1745–1748.

Zhang, J., M. Steele, et al. (2004). "Increasing exchanges at Greenland-Scotland Ridge and their links with the North Atlantic Oscillation and Arctic sea ice". In: *Geophysical research letters* 31(9).

Zhu, J & E Demirov (2011). "On the mechanism of interannual variability of the Irminger Water in the Labrador Sea". In: *Journal of Geophysical Research: Oceans* 116(C3). DOI: https://doi.org/10.1029/2009JC005677.

Appendix A

Ocean Model and Experimental Design

The model setup used in Chapter 2 was the same model runs used in my Master's thesis (S. Lundrigan, 2010). This appendix is Chapter 3 from my Master's thesis to give details on the specifics of the model and its setup and forcing that was used.

The model used in this study is the NEMO-OPA model (Madec, 2008) coupled to the multi-layered ice model NEMO-LIM (T.Fichefet & M.A.Morales Maqueda, 1997). Both the ocean model (NEMO-OPA) and sea-ice model (NEMO-LIM) are configured on a global tripolar grid at 2^o horizontal resolution with 31 vertical levels, 20 of which are in the top 500 m, (see Figure A). This coarse resolution tri-polar grid has two north poles, one over northern Canada and the other over Siberia in order to avoid singularities of the model grid over the ocean (see Figure A). The configuration of this grid leads to a horizontal resolution of about 90 km within the study region.

Other models are often chosen to be used, such as the NAOSIM hierarchy, which

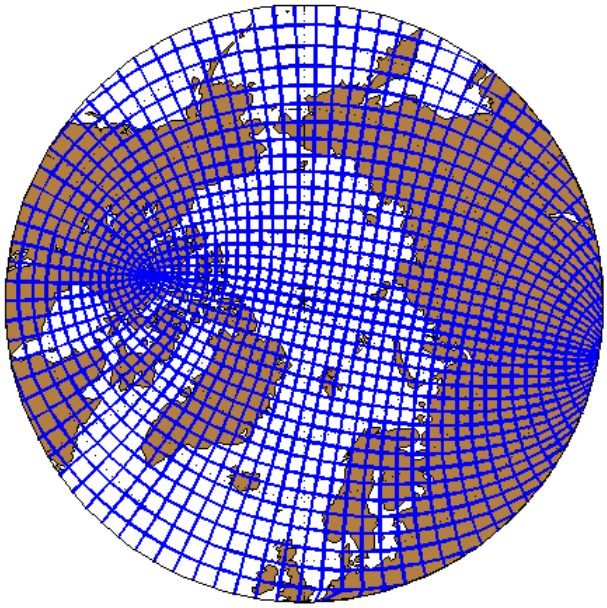

Figure A.1: The tripolar model grid shown for the study region.

are a group of ocean/sea ice models that are used to study the North Atlantic and Arctic Ocean and the HadCM3 model, which is a coupled ocean and atmosphere model. The NEMO-OPA model is used in this study because it met the requirements for the needed resolution and speed and its ability to be set up easily on our computing platform.

A.1 The Model Equations

The governing equations of the model are geophysical fluid dynamics equations on a curvilinear coordinate system. The model assumes the ocean is incompressible, *i.e.*

$$\nabla \cdot \mathbf{U} = 0 \tag{A.1}$$

The Reynold's number is defined as the ratio of advective terms to diffusive terms and simplifies to:

$$Re = \frac{UL}{\nu} \approx \frac{(0.1m/s)(10^5\ m)}{10^{-6}\ m^2/s} = 10^{10} \tag{A.2}$$

The Reynold's number is very large due to the large length scales (L $\sim$ 100 km) of the ocean. This means that oceanic flows are always turbulent. Therefore the friction in the model must include turbulent stress and eddies.

The Navier-Stokes equation for an incompressible turbulent fluid in a rotating coordinate system is:

$$\rho \frac{D\mathbf{U}}{Dt} = -\nabla P + \rho \mathbf{g} + \nabla \nu \nabla \mathbf{U} - 2\mathbf{\Omega} \times \mathbf{U} \tag{A.3}$$

where $\frac{D}{Dt}$ is the material derivative , ∇ is the gradient, t is the time, z is the vertical coordinate, P the pressure, Ω is the Earth's angular velocity vector, g is the

gravitational acceleration, ν is the turbulent viscosity, and ρ is the *in situ* density given by the equation of state

$$\rho = \rho(T, S, P) \tag{A.4}$$

The material derivative in Equation A.3 is defined according to:

$$\frac{D\mathbf{U}}{Dt} = \frac{\partial \mathbf{U}}{\partial t} + \mathbf{U} \cdot \nabla \mathbf{U} \tag{A.5}$$

which after using some vector algebra identities becomes

$$\frac{D\mathbf{U}}{Dt} = \frac{\partial \mathbf{U}}{\partial t} + \frac{\nabla \mathbf{U}^2}{2} + (\nabla \times \mathbf{U}) \times \mathbf{U} \tag{A.6}$$

The small-scale physics for momentum is parametrized by using a turbulent model in the vertical and Laplacian operator in the horizontal. We will use the notation $D_h^u = \nabla \nu \nabla \mathbf{U}$ for the mixing.

The Boussinesq approximation, usually used in ocean models, assumes that the density is equal to the average density,ρ_o, in all equations except the vertical momentum equation, therefore Equation A.3 becomes:

$$\frac{\partial \mathbf{U}_h}{\partial t} + \left[\frac{\nabla \mathbf{U}^2}{2} + (\nabla \times \mathbf{U}) \times \mathbf{U} \right]_h = -\frac{1}{\rho_o} \nabla_h P + \mathbf{D}_h^{\mathbf{U}} - 2\mathbf{\Omega} \times \mathbf{U}_h \tag{A.7}$$

where the h subscript denotes that it is the local horizontal vector.

In the vertical we assume that all the terms except the pressure gradient and gravity are negligible. Then we obtain

$$\frac{\partial p}{\partial z} = -\rho g \tag{A.8}$$

which is known as the hydrostatic approximation.

The equations for the conservation of temperature and salinity close the system

$$\frac{\partial T}{\partial t} = -\nabla \cdot (T\mathbf{U}) + D^T \tag{A.9}$$

$$\frac{\partial S}{\partial t} = -\nabla \cdot (S\mathbf{U}) + D^S \tag{A.10}$$

where D^T and D^S are the parametrizations of small-scale physics for temperature and salinity.

The model uses a 2^{nd} order centered advection scheme. In this formulation the value at the velocity points is the mean of the two neighbouring T-point values and is of second order accuracy. The vorticity term in Equation A.7 is calculated using an enstrophy conserving scheme. With this scheme there is a global conservation of enstrophy, ($[(\zeta + f)/e_{ef}]^2$), for a horizontally non-divergent flow (Madec, 2008).

The kinematic boundary conditions are defined at the surface and at solid earth - ocean boundaries. At the bottom mass must be conserved and therefore

$$w = -\mathbf{U}_h \cdot \nabla(H), z = H \tag{A.11}$$

when H is the depth of the ocean at a given location.

At the surface boundary mass conservation gives

$$w = \frac{\partial \eta}{\partial t} + \mathbf{U}_h|_{z=\eta} \cdot \nabla_h(\eta) + P - E, z = 0 \tag{A.12}$$

where $P - E$ is the mass flux of freshwater into the surface. Using Equations A.11, A.12 and the continuity equations we find the free surface equation

$$\frac{\partial \eta}{\partial t} = \nabla \cdot \left[(H + \eta)\bar{\mathbf{U}} + P - E\right] \tag{A.13}$$

which is used to calculate the height of the ocean free surface.

The wind stress is calculated from the bulk formulas

$$\tau = \rho C_D U_{10}^2 \tag{A.14}$$

where τ is the wind stress, ρ is the density of the air, C_D is the drag coefficient of the surface and U_{10} is the wind speed at 10 m above the surface. Over the ocean there is a lower coefficient of friction than over regions with highly ridged sea ice. The dynamic boundary condition at the surface is (Madec, 2008):

$$\begin{aligned} \tau_x &= \nu \frac{\partial u}{\partial z}, z = 0 \\ \tau_y &= \nu \frac{\partial v}{\partial z}, z = 0 \end{aligned} \tag{A.15}$$

No slip boundary condition is defined at the bottom boundary is defined:

$$u = v = 0 \tag{A.16}$$

The temperature and salinity surface flux boundary conditions are given by

$$\begin{aligned} \frac{\partial T}{\partial t}|_{z=0} &= \frac{Q_{ns}}{\rho_o C_p e3t} \\ \frac{\partial S}{\partial t}|_{z=0} &= \frac{EMP\ S|_{z=0}}{e3t} \end{aligned} \tag{A.17}$$

respectively (Madec, 2008). Where Q_{ns} is the heat flux absorbed at the surface and includes the sensible, latent and long wave radiative fluxes. EMP is the total surface freshwater budget, evaporation - precipitation - river runoff + change is sea ice thickness. The heat capacity is C_p and $e3t$ is the depth of the first model layer. The short wave radiative flux penetrates below the surface and is absorbed in the water column.

A.2 Model Grid

The model is configured on a standard staggered Arakawa C grid. The scalar grid points are denoted by t, vector grid points are denoted by u and v and the vorticity

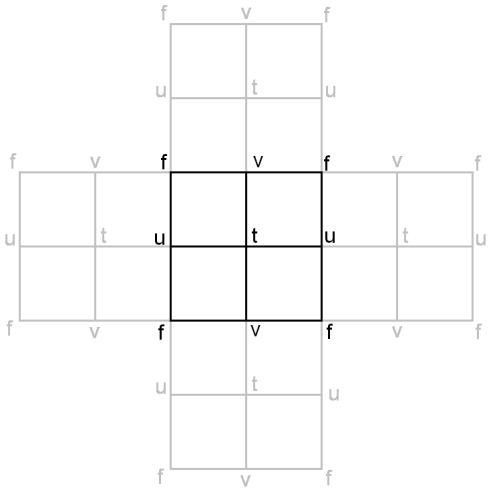

Figure A.2: Arakawa C-grid.

grid points are denoted by f. The different grid point are shifted by a half step as shown in Figure A.2.

The scale factors define the local metrics of the curvilinear tri-polar grid. They are defined as the distance between the grid points. In the both the north-south direction and the east-west directions they are given by:

$$\begin{aligned} e_1 &= (a+z)\left[\left(\frac{\partial\lambda}{\partial i}\cos\phi\right)^2+\left(\frac{\partial\phi}{\partial i}\right)^2\right]^{1/2} \\ e_2 &= (a+z)\left[\left(\frac{\partial\lambda}{\partial j}\cos\phi\right)^2+\left(\frac{\partial\phi}{\partial j}\right)^2\right]^{1/2} \\ e_3 &= \left(\frac{\partial z}{\partial k}\right) \end{aligned} \tag{A.18}$$

where a is the radius of the earth, z is the altitude above a reference sea level, λ is the longitude and ϕ is the latitude. Within the thin-shell approximation $(a+z)$ can be replaced by a. (Madec, 2008)

Partial steps are used along the bottom topography. Without using the partial steps the bottom topography is divided up into discrete steps that have the size of the model vertical levels. These larger steps can misrepresent a shallow sloped bottom or large localized depth gradients and this can lead to large localized vertical velocities which leads to numerical dispersion effects. Therefore, partial steps are used to better represent the topography (Madec, 2008) (B.Bernard et al., 2006).

The model's salinity and temperature profiles were initialized using monthly averaged Levitus salinity and temperature (Antonov et al., 2005). In order to reduce model drift and bias on the climatological time scale a spectral nudging scheme is applied (Thompson et al., 2006). The nudging is applied to the surface layers above 45^oN for salinity only so as to not affect the interannual variability in the intermediate waters in which we are concerned.

A.3 Forcing and Ensemble model runs

The model forcing is computed from bulk parametrization of the surface turbulent heat, momentum and water fluxes. These turbulent fluxes are computed with model SST, near surface atmospheric temperature, wind speed, humidity and precipitation using the bulk formulae. They relate the wind stress (τ), sensible heat (SH) and

latent heat (LH) to the measured quantities of the atmosphere.

$$\begin{aligned} \tau &= \rho_{atm} C_d (u_{atm} - u_s) \\ SH &= \rho_{atm} C_h (T_{atm} - T_s) \\ LH &= \rho_{atm} C_e u (q_{atm} - q_s) \end{aligned} \tag{A.19}$$

Where ρ_{atm} is the surface air density, $u_{atm}, T_{atm}, q_{atm}$ are the wind speed, temperature and specific humidity respectively at 10 m. $u_{atm}, T_{atm}, q_{atm}$ at 10 m can be calculated from wind, temperature and humidity at any height and stratification using profile relationships. The 's' subscript means the value at the surface. In these formulas u_s is assumed to be zero and q_s is the saturation humidity at T_s multiplied by 0.98 because of the reduced saturation of the specific humidity due to being over salt water. The coefficients C_d, C_h, C_e are determined empirically. The total cloud cover is used to calculate the surface radiative balance.

Ocean models are not a perfect representation of the actual physics that occurs in the ocean. They are many parametrizations in the models and therefore there is error associated with the model itself. The coarseness of this model allows for an ensemble of runs to be possible. Using different initial conditions for each ensemble member the model's error in the results can be studied. In this thesis all results presented are the raw mean of the ensemble members and the error bars given are the 95% confidence level in the ensemble unless otherwise stated.

The atmospheric parameters used in this study are from NCEP/NCAR reanalysis. Two data sets of these parameters are used in this study: they are monthly mean data and 6-hourly NCEP/NCAR data for the period 1948-2005. This is first spun-up

for 30years using climatological atmospheric conditions as the forcing. The model is then run for 50 years, from 1948-2005, using the 6 hourly NCEP/NCAR forcing. A 'snap-shot' is saved every year during this run. Six of these 'snap-shots' were then chosen to be the initial conditions for each of the ensemble members, the first one after another 37 years of spin-up. The initial conditions are chosen so as to have a spread of intensities and sign of the North Atlantic Oscillation (NAO) index. The chosen years were 1985, 1989, 1992, 1994, 1996 and 1997. Each of these 6 initial conditions were used to the ensemble from 1948-2005 saving the output monthly for analysis. The output from 1965-2005 is used for analysis in this study.

References

Antonov, J. et al. (2005). "World Ocean Atlas 2005, Volume 2:Salinity". In: *NOAA Atlas NESDIS 62*. Ed. by S. Levitus. U.S. Government Printing Office, Washington, D.C., 182p.

B.Bernard et al. (2006). "Impact of partial steps amd momentum advectoin schemes in a global ocean ciruclation model at eddy-permitting resolution." In: *Ocean Dynamics* 56, pp. 543–567.

Lundrigan, S. (2010). "A Model Study of Interannual and Decadal Variability of the Arctic and Sub-Arctic Oceans". MSc. Newfoundland: Memorial University of Newfoundland.

Madec, G. (2008). *NEMO ocean engine: version 3.1*. Laboratoire d'Oceanographie et du Climat: Experimentation et Approches Numeriques.

T.Fichefet & M.A.Morales Maqueda (1997). "Sensitivity of a global sea ice model to the treatment of ice thermodynamics and dynamics." In: *J. Geophys. Res.* 102, pp. 12609–12646.

Thompson, K.R. et al. (2006). "A simple method for reducing seasonal bias and drift in eddy resolving ocean models". In: *Ocean Model*, pp. 122–138.

Appendix B

Determination of Surface Geostrophic Eddy Velocity

In this study, EN and GFO along-track altimeter observations are used to estimate eddy surface geostrophic velocity. The calculation of geostrophic velocity from along-track data is based on the method suggested by Stammer and Dieterich (1999). This method was previously successfully applied in a study by Brath et al. (2010) on eddy kinetic energy (EKE), mean circulation, and eddy-driven heat transport in the subpolar ocean.

The sea-level anomaly $\eta' = \eta - \overline{\eta}$ is defined as the difference between sea level η and the record mean $\overline{\eta}$ over the period of study from 2003 to 2008. The values of $\overline{\eta}$ may differ from the long-term mean $\widehat{\eta}$ (the geoid) used in the calculation of the sea-level anomalies. The latter is typically calculated over another period than the period used in our study and may differ from $\overline{\eta}$ because of the presence of interannual variability. To account for this difference, we correct the long-term effects in the

following way. First, the time average of sea-level anomalies is calculated on a 1×0.5 grid. The grid size was chosen to ensure that there are enough sea-level anomaly points in all grid boxes. Then, the time mean sea-level anomaly is interpolated and added to the long-time mean $\widehat{\eta}$.

The anomaly of surface geostrophic velocities (Brath et al., 2010) is calculated on a virtual track between two satellite tracks. The points 1, 2, and 3 are the closest observation points on the two tracks. The η_4' is found through interpolation between the closest data points. Then, the eddy velocity along-track components are defined by

$$\begin{aligned} \widetilde{u'} &= \frac{-g}{f}\frac{\eta_2' - \eta_1'}{D_{12}} \\ \widetilde{v'} &= \frac{g}{f}\frac{\eta_3' - \eta_4'}{D_{34}} \end{aligned} \tag{B.1}$$

where η_1', η_2', η_3', and η_4' (see Figure B.1) are the sea-surface height anomalies on separate satellite tracks and $D_{12} > 0$ and $D_{34} > 0$ are the distances between the observations on the two satellite tracks. To ensure that the satellite tracks are close together, data points further apart than 40 km are not used. On average the points from the two tracks are approximately 12 km. The velocities $\tilde{u'}$ and $\tilde{v'}$ are then rotated by θ to get the final x and y components of velocity $\vec{U}$.

The advective heat flux at the along-track points is calculated in a similar way:

$$\mathbf{u}' \cdot \nabla T' = \widetilde{u'}\frac{T_3' - T_4'}{D_{34}} + \widetilde{v'}\frac{T_2' - T_1'}{D_{12}} \tag{B.2}$$

The values of $T_1', T_2', T_3', and T_4'$ are interpolated in space and time from the satellite gridded SST data onto the points 1, 2, 3, and 4 along the two satellite tracks in Figure B.1. These along-track values of the advective heat flux convergence are then

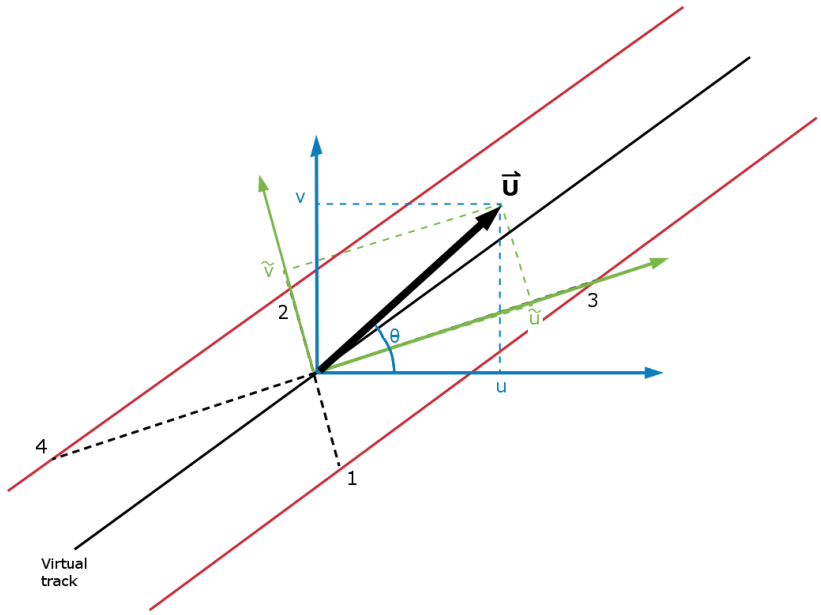

Figure B.1: A schematic diagram of the geometry of geostrophic velocity computation using along-track sea-level anomalies. The black line is the virtual track for which the velocities are calculated. The two red lines are the paths of the two satellite along-track observations. Numbers $1-4$ define the positions of the sea-level anomaly observations that are used to compute the green velocity components. $\vec{U}$ is the final velocity on the Cartesian coordinate system after a rotation by θ.

averaged in time over a regular grid where the mean eddy heat convergence $\overline{\mathbf{u}'\nabla T'}$ is calculated.

Appendix C

Eddy Detection from Surface Altimetry

In this study, we use wavelet transformations of sea-level anomaly data as an objective method for eddy detection. The window size of the wavelet transform is inversely proportional to the frequency of an event. Therefore, the window size is larger for low-frequency events than for high-frequency events. The wavelet transform is a natural choice when the high-frequency events are expected to be rescaled versions of a signal that has a similar structure across different scales, which is the case for eddies. The wavelet method used in this study follows the work of Lilly et al. (2003).

The wavelet transform of a time series $x(t)$ with a wavelet $g(t)$, shown in Figure C.1, is defined as

$$W^{(n)}[x](\tau, a) = \int_{-\infty}^{\infty} \frac{1}{a^n} g^* \left(\frac{t-\tau}{a} \right) dt \tag{C.1}$$

The wavelet transform of $x(t)$ with $g(t)$ is the convolution of $x(t)$ with rescaled

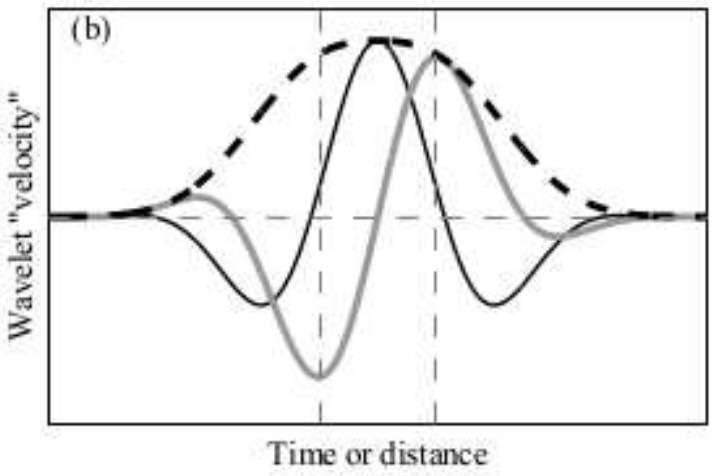

Figure C.1: Slepian Wavelet example. The thin black (thick gray) line is the real (imaginary) part of the wavelet, the thick dashed line is the envelope function h. (Lilly et al., 2003)

and time-reversed versions of the wavelet. The wavelet transform

$$W^{(n)}[x](\tau, a) = x * g_a^{(n)}(\tau) \tag{C.2}$$

is just the convolution of $x(t)$ with $g(t)$ itself.

The wavelet $g(t)$ has the form

$$g_{\tau,a}(x) = \frac{1}{a} h\left(\frac{t-\tau}{a}\right) e^{(2\pi i k(x-\tau))} + \frac{\epsilon}{a} \tag{C.3}$$

where $h(t)$ is a slowly varying envelope and k is the wavenumber of the wavelet at scale a. The envelope function h(t) is a real valued and even window. In order for the wavelet analysis to yield phase information the wavelet needs to be complex, therefore the real valued envelope function is multiplied by the $e^{(2\pi i k(x-\tau))}$ term. If the window were chosen to be the simple Gaussian window, as is often done, it would make a Morlet wavelet. However this wavelet has long tails and makes the localization of

time less precise. Therefore in this analysis, as per Lilly et al. (2003), the discrete prolate spheroidal sequences (DPSS) are used, Figure C.1. The shape of the DPSS matches better the shape of the eddies we expect to observe.

Before the wavelet analysis was done the seasonal signal was removed. The regular seasonal cycle we defined as

$$A + B \times cos(Ct + D) \tag{C.4}$$

The first step to find the seasonal signal is to fit the data to Equation C.4. The seasonal cycle is then removed to find the outliers in the timeseries. The low frequency signal was then found using low pass filtering on the timeseries with no outliers and no seasonal signal. The next step (and all subsequent steps) involves removing the low frequency signal and the outliers identified in the last step from the original data. The seasonal cycle is found again by fitting this data to equation 3. The outliers and the low frequency signal are found again and removed for the next step in the iteration. This is done until there are no more outliers and the seasonal cycle and low frequency signal are no different than in the previous step.

The wavelet transform has a greater strength when the time series of anomalies matches well with the wavelet of a particular scale. The largest value of the wavelet transform modulus within some neighbourhood is an 'isolated anomaly' as per Lilly et al. (2003). The isolated anomaly point (τ_*, a_*) is therefore defined as

$$|W(\tau_*, a_*)| \geq |W(\tau, a)| \qquad \begin{cases} |\tau_* - \tau| \leq b_\tau a_* \\ |a_* - a| \leq b_a a_* \end{cases} \tag{C.5}$$

where b_τ and b_a are the dimensions of the neighborhood.

The phase of our complex wavelet transform at point (τ_*, a_*) indicates whether the isolated event at that point is even or odd. The phase angle is defined as

$$\phi_* = \arctan\left(\frac{W_s(\tau_*, a_*)}{W_c(\tau_*, a_*)}\right) \tag{C.6}$$

$$\phi_* = \begin{cases} = 0 & \text{even, with a positive SSH anomaly} \\ = \pm\pi & \text{even, with a negative SSH anomaly} \\ = \pm\frac{\pi}{2} & \text{odd} \end{cases} \tag{C.7}$$

The dimensions of the apparent radius of the event signal are defined using the phase angle in such a way that the radius can be calculated for both monopole events ($\phi_* = 0$ or $\phi_* = \pm\pi$) and dipole events ($\phi_* = \pm\pi/2$). The radius of the dipole signal is considered for each pole separately:

$$R_* = a_* \left(\sin^2(\phi_*) + 1\right) \tag{C.8}$$

The dynamical strength of an eddy-like event is characterized by the maximum of the vertical vorticity within the core. A non-dimensional measure of this (or an estimate of the Rossby number) is given by

$$Z_* = \left(\cos^2(\phi_*) + 1\right) \frac{V_*}{fR_*} \tag{C.9}$$

where V_* is estimated assuming the event has a velocity profile expected from a solid-body core geostrophic eddy:

$$V_* = -2b\frac{g\delta_*}{fR_*} \tag{C.10}$$

where b is based upon the profile of the eddy (it is 0.3 for a typical monopole) and δ_* is the SSH excursion at the location of interest.

References

Lilly, J.M. et al. (2003). "Observations of the Labrador Sea eddy field". In: *Progress in Oceanography* 59(1), pp. 75–176. DOI: https://doi.org/10.1016/j.pocean.2003.08.013.

Appendix D

Method of Eddy Path detection

The paths travelled by eddies that are identified using the wavelet analysis are found by iteratively looking for eddy events that are similar and near-by in space and time.

From a list of all eddy events taking the first one, Eddy A, all other eddy events are searched to find eddy events that are similar. Similar is defined here as the two eddy events being within 150 km, be observed within 35 days of each other and have amplitudes and radii that are within 0.25 and 2.5 times their previous size. If there is an eddy event, say Eddy B, which meets this criteria then it is added to the 'eddy path' of Eddy A, which we will call Eddy Path α. If there are multiple eddy events that meet the criteria then the closest in space event is chosen as the next eddy in the path. Both Eddy A and Eddy B are removed from the list of available events before the next step. To find the next eddy event in Eddy Path *alpha* the location, date and size of Eddy B is used to search in the list again to find similar eddy events. This iterative approach is used until no eddy events left in the list are similar to the last eddy in the Eddy Path α. Then you have the complete Eddy Path α which starts at

Eddy A. Next you start the search again with the list of eddy events that has all the eddies from Eddy Path α removed.